UNIVERSITY OF CALIFORNIA SAN DIEGO

Exploring nanoscale chemical distributions for energy applications using atom probe tomography

A dissertation submitted in partial satisfaction of the requirements for the degree Doctor of Philosophy

in

Nanoengineering

by

Pritesh Parikh

Committee in charge:

Professor Ying Shirley Meng, Chair
Professor Eric Fullerton
Professor Olivia Graeve
Professor Ping Liu
Professor Paul Yu

2019

The Dissertation of Pritesh Parikh is approved, and it is acceptable in quality and form for publication on microfilm and electronically:

_____

_____

_____

_____

_____
Chair

University of California San Diego

2019

DEDICATION

This thesis is dedicated to my family.

My mother, *Nrupa* for being my lifeline through these years; my father, *Anish* for encouraging me to dream big and follow my passion;

my sister, *Hesha* for being my partner-in-crime and my brother-in-law *Zubin* for his unending support.

EPIGRAPH

“I learned very early the difference between knowing the name of something and knowing something”

Richard P. Feynman

TABLE OF CONTENTS

LIST OF ABBREVIATIONS

APT	Atom Probe Tomography
TEM	Transmission Electron Microscopy
FET	Field Effect Transistor
PMOS	P-type Metal Oxide Semiconductor
NMOS	N-type Metal Oxide Semiconductor
CIGS	Cadmium Indium Gallium Selenide
MBE	Molecular Beam Epitaxy
FA	Formamidinium
UV	Ultra-violet
RH	Relative Humidity
2D	Two dimensional
BMS	Battery Management Systems
EELS	Electron energy loss spectroscopy
SEM	Scanning Electron Microscopy
XRD	X-ray Diffraction
SIMS	Secondary Ion Mass Spectrometry
ppm	Parts per million
DC	Direct-current
FIB	Focused ion beam
amu	Atomic mass units
IVAS	Integrated Visualization and Analysis Software

IR	Infra-red
STEM	Scanning Transmission Electron Microscopy
EDS	Energy dispersive X-ray spectroscopy
3D	Three dimensional
SRAM	Static Random-Access Memory
CAD	Computer Aided Design
GIS	Gas Injection System
ARM	Axial Rotational Manipulator
LEAP	Local Electrode Atom Probe
HAADF	High Angle Annular Dark Field
VNAND	Vertical NAND gate
PSC	Perovksite solar cell
HTL	Hole Transport Layer
BF-TEM	Bright Field Transmission Electron Microscopy
EF-TEM	Energy Filtered Transmission Electron Microscopy
FTO	Fluorine-doped tin oxide
FTIR	Fourier Transform Infra-red Spectroscopy
HRTEM	High resolution Transmission electron microscopy
SAED	Selective Area Electron Diffraction
XAS	X-ray Absorption Spectroscopy
ALD	Atomic layer deposition
NMP	N-methyl 2-pyrrolidone

SEI	Solid electrolyte interphase
CMC	Carboxy methyl cellulose
PAA	Polyacrylic acid
EC	Ethylene carbonate
DEC	Diethylene carbonate
FEC	Fluoroethylene carbonate
DMC	Dimethyl carbonate

LIST OF SYMBOLS

¢	Cents
W	Watt
kg	kilogram
Co	Cobalt
Mn	Manganese
Ni	Nickel
Al	Aluminum
Li	Lithium
Z	Atomic number
Da	Dalton
Na	Sodium
S	Sulfur
Se	Selenium
A	Ampere
Si	Silicon
Pt	Platinum
K	Kelvin
pJ	picoJoule
μ	Micrometer
κ	Kappa
n	Nano

F	Fluorine
O	Oxygen

LIST OF FIGURES

LIST OF TABLES

ACKNOWLEDGEMENTS

A PhD is a life changing experience and a good mentor can change the course of your future. Through this journey, I have been fortunate to be mentored by Prof. Shirley Meng who made me a stronger, more confident individual and an independent researcher. I am truly grateful for her belief in my abilities and her training to allow me to achieve limits, that even I thought were not possible. I would like to thank her for her guidance, her rigorous testing of my skills and the financial support provided by her. I would also like to thank my committee members, Prof. Paul Yu, Prof. Eric Fullerton, Prof. Olivia Graeve and Prof. Ping Liu for their unique perspectives and suggestions that have strengthened this thesis.

I would also like to thank Dr. Arun Devaraj, who taught me everything I know about atom probe tomography and without whom this research would not have been possible. It has been truly rewarding to learn both science and life experiences from him. His positive demeanor, passion for science and his way of working with people are all qualities I wish to imbibe in myself one day. I would also like to thank Priya Thekkumparambath Mana for all her delicious cooking and tips on working with Arun, during my time at Pacific Northwest National Laboratory.

I am especially grateful to my family. Without their love and support, this journey would not have been possible. I would like to thank my mom, Nrupa Parikh, who believed and supported me in my scientific career right from the start and her soothing words during difficult times. My dad, Anish Parikh, has been the moral and financial support for my entire family and his strength and tenacity has been

an inspiration to me. Both my parents' struggles and values they uphold, have made me into the person I am today. My sister, Hesha Irani, has been my happy place during rough times and her positive and practical attitude has helped me stay focused and motivated. I thank her for that. My brother-in-law, Zubin Irani has been an ardent supporter of higher education since the start and I would like to thank him for his support. I would also like to thank my maternal grandmother, Kokilaben Parikh and my maternal grandfather, Vasant Parikh, and my paternal grandmother, Bhanuben Parikh for their support and well wishes. I am deeply grateful to my extended family in San Diego that have made me feel at home in US. Shilpa Mody, Nimish Mody, Samiya and Sparsh Mody have all been my strength and an integral part of my support system.

Very rarely do you also get the chance to work with student mentors that can provide expert guidance but also ignite a true passion for science in you and I am grateful to have worked with Dr. Abhik Banerjee on silicon anodes and with Dr. Shen Wang on perovskite solar cells for this.

Without a team of experts, it would have been challenging to achieve the progress that I did in my PhD and there are several people, I would like to thank for that. Dr. Michael DiBattista, Corey Senowitz, Don Lyons, Dr. Isabelle Martin, Dr. Ty Prosa, Dr. Daniel Perea, Dr. Zoe Zhou and Dr. Kent Snyder have all been instrumental in teaching me different aspects of research, communication and networking skills.

LESC has a group of brilliant minds working on such challenging problems, and everyone in the group has always created a very welcoming atmosphere to work at. I would especially like to thank Dr. Danna Qian, Dr. Haodong Liu, Dr. Mike Verde, Dr. Judith Alvarado, Dr. Chuze Ma, Unjong Lee, Tom Wynn, Hyusueng Chung, Han Nyugen for their support, guidance and assistance with techniques and experiments. I would also like to thank all of LESC members, past present for their unique technical skills that I could learn from and making LESC a great place to work at.

I would also like to thank my silicon anode group, Osman Trieu, Dr. Dijo Damien, Macwin Savio D'Souza and Josh Gong without whom we could not have achieved the current progress on anode materials in LESC.

Lastly, a support system can make a great difference for your mental and emotional health and I am grateful to my group of friends here in San Diego and my dance groups across the 4 years as part of the Association of Indian Graduate Students. I would like to thank Neeraja Vegesna, Nandkishore Prakash and Vaibhav Hatkar for their support and everlasting friendship. I would also like to thank Vignesh Srinivasan, Sunandha Srikanth, Kanika Khanna and Dr. Siddhartha Nath for their support during trying times.

Finally, I would like to thank my funding sources, Qualcomm (through the Qualcomm Mentor Fellow Award), PNNL (through the Alternative Sponsor Fellow) and Ford (through the University Research Program).

Chapter 4, in full, is a reprint of the material Parikh, P., Senowitz, C., Lyons, D., Martin, I., Prosa, T. J., DiBattista, M., Devaraj, A. & Meng, Y. S. Three-Dimensional Nanoscale Mapping of State-of-the-Art Field-Effect Transistors (FinFETs). *Microscopy and Microanalysis* **23,** 916–925 (2017). The dissertation author was the primary investigator and author of this paper. APT measurements and sample preparation were performed by the author. Isabelle helped with the APT measurements for NMOS. Corey and Don worked on the STEM-EDS sample preparation and results. Corey and Don also helped with the interpretation of the APT data.

Chapter 5, in full, is currently being prepared for submission for publication, Parikh, P., Chung, H., Vo, E., Banerjee, A., Devaraj, A. & Meng, Y.S. Compositional quantification of high nickel content NCA and NMC battery oxides using Atom Probe Tomography. The dissertation author was the primary investigator and author of this paper. Haelie (Hyesueng Chung) was responsible for the electrochemistry for NCA cathodes. Ethan helped with the APT data acquisition.

Chapter 6, in full, is currently being prepared for submission for publication, Parikh, P., Zhang, Y., Damien, D., Trieu, O., Fang, C., Banerjee, A., Perea, D., Devaraj, A. & Meng, Y.S. Direct observation of Li during first cycle lithiation of silicon anodes. The dissertation author was the primary investigator and author of this paper.

Chapter 7, in full, is a reprint of the material Wang, S., Sina, M., Parikh, P., Uekert, T., Shahbazian, B., Devaraj, A. & Meng, Y. S. Role of 4- *tert* -Butylpyridine as a Hole Transport Layer Morphological Controller in Perovskite Solar Cells. *Nano Letters* **16,** 5594–5600 (2016). The dissertation author was the co-author of this paper. APT measurements and sample preparation were performed by the dissertation author.

VITA

2008-2013 Bachelor of Engineering, BITS Pilani Hyderabad Campus, India

2008-2013 Master of Science, BITS Pilani Hyderabad Campus, India

2013-2014 Research Assistant, IIT Bombay, India

2014-2019 Research Assistant, University of California San Diego

2014-2019 Doctor of Philosophy, University of California San Diego

PUBLICATIONS

Parikh, P., Sina, M., Banerjee, A., Wang, X., D'Souza, M. S., Doux, J.-M., Wu, E. A., Trieu, O. Y., Gong, Y., Zhou, Q., Snyder, K. & Meng, Y. S. Role of Polyacrylic Acid (PAA) Binder on the Solid Electrolyte Interphase in Silicon Anodes. *Chem. Mater.* **31,** 2535–2544 (2019).

Wang, S., Huang, Z., Wang, X., Li, Y., Günther, M., Valenzuela, S., **Parikh, P.**, Cabreros, A., Xiong, W. & Meng, Y. S. Unveiling the Role of tBP–LiTFSI Complexes in Perovskite Solar Cells. *Journal of the American Chemical Society* **140,** 16720–16730 (2018).

Parikh, P., Senowitz, C., Lyons, D., Martin, I., Prosa, T. J., DiBattista, M., Devaraj, A. & Meng, Y. S. Three-Dimensional Nanoscale Mapping of State-of-the-Art Field-Effect Transistors (FinFETs). *Microscopy and Microanalysis* **23,** 916–925 (2017).

Devaraj, A., Perea, D. E., Liu, J., Gordon, L. M., Prosa, T. J., **Parikh, P.**, Diercks, D. R., Meher, S., Kolli, R. P., Meng, Y. S. & Thevuthasan, S. Three-dimensional nanoscale characterization of materials by atom probe tomography. *International Materials Reviews* **63,** 68–101 (2018).

Trease, N. M., Seymour, I. D., Radin, M. D., Liu, H., Liu, H., Hy, S., Chernova, N., **Parikh, P.**, Devaraj, A., Wiaderek, K. M., Chupas, P. J., Chapman, K. W., Whittingham, M. S., Meng, Y. S., Van der Van, A. & Grey, C. P. Identifying the Distribution of Al3+ in LiNi0.8Co0.15Al0.05O2. *Chem. Mater.* **28,** 8170–8180 (2016).

Wang, S., Sina, M., **Parikh, P.**, Uekert, T., Shahbazian, B., Devaraj, A. & Meng, Y. S. Role of 4- *tert* -Butylpyridine as a Hole Transport Layer Morphological Controller in Perovskite Solar Cells. *Nano Letters* **16,** 5594–5600 (2016).

FIELDS OF STUDY

Major Field: Engineering

Studies in Nanoengineering
Professor Ying Shirley Meng

ABSTRACT OF THE DISSERTATION

Exploring nanoscale chemical distributions for energy applications using atom probe tomography

by

Pritesh Parikh

Doctor of Philosophy in Nanoengineering

University of California San Diego, 2019

Professor Ying Shirley Meng, Chair

Life on earth exists due to a delicate balance with nature, one that has been skewed in our favor since the industrial revolution. The growing population demands energy for homes, offices, portable devices and transportation. However,

our reliance on natural gas/coal and petroleum to fulfill these requirements have led to an unprecedented increase in atmospheric CO_2 levels that threaten our own existence. A paradigm shift in how we generate, store and monitor energy is needed, with green energy and sustainability paving a way forward. The advent of photovoltaics and Li-ion battery have given us the necessary tools to bring about this change, but continued research relies on a deeper understanding of the mechanisms involved and materials developed for each technology. As the materials chemistry, size of particles and nature of the interfaces become more complex, the need for nanoscale analysis has never been more aptly described. 3D tomographic measurements can provide a clear picture of the materials composition and interface properties, with atom probe tomography (APT) allowing a nanoscale chemical and spatial analysis. Herein, we use APT to enhance our understanding of the device mechanisms and core material properties for photovoltaics, Li-ion batteries and state-of-the-art semiconductor fins. Our understanding can help to build better structure-property relations by tying in nanoscale analysis with bulk properties that will ultimately lead to better design and development of energy devices across a broad range of technologies.

Chapter 1 : Introduction and Thesis Outline

Since the industrial revolution, advances in science and technology have helped to slowly overcome challenges related to health, diseases, food shortage, hunger, sanitation and clean drinking water as well as infrastructure and education. These advances have improved our standard of living thus increasing the average lifespan. However, to satisfy the demands of the growing population, our reliance on plastic, microplastic products and fossil fuel-based energy have led to a multitude of environmental effects. These range from mass extinction of marine and terrestrial species due to plastic waste that ends up in the ocean, global warming from greenhouse gas emissions (primarily from CO_2 released by burning coal and natural gas) and increase in respiratory diseases due to pollutants released in the atmosphere from vehicular transport and industrial plants.

In order to provide a safe, sustainable environment to future generations, one of the major challenges continues to be availability and development of carbon-free or zero emissions energy. Overcoming this challenge will not only enable a sustainable future but it also creates a ripple effect that aids other challenges we currently face. It can provide clean energy for growth of lab scale plants to feed a larger population, provide energy for clean drinking water through de-salination plants and lead to independent sustainable communities. In this respect green energy, through the use of perennial renewable energy sources and energy storage devices (which can be recycled) can help to alleviate the stresses

we put on this planet. This can possibly curb atmospheric greenhouse gas levels and reverse current global warming trends.

Within the green energy space, there are three important aspects that are needed for a comprehensive approach; [a] Energy generation solutions [b] Energy storage solution and [c] Automation solutions to interface between generation and storage. Over the past few decades, continuous R&D efforts have enabled growth in each of these aspects. For instance, development of tandem solar cells, high gravimetric energy density (300-400 Wh/kg) for Li-ion batteries, development of perovskite solar cells and the recent success of electric cars are just some recent examples of this growth. Driven by the recent cost benefits (in ¢/kWh) over conventional coal/gas-based utility scale plants, the path towards green energy seems to be an inevitable one. However, the future will require continuous research, development and more importantly better and faster integration of all 3 aspects.

Over the past few decades, nanoscience and nanotechnology have helped to solve challenges that previously would not have been possible. For instance, nanoscience has enabled the development of high energy and power density cathodes[1,2] and anodes[3,4] for Li-ion batteries by understanding the surface degradation mechanism and mitigating it using nanoscale protective surface coatings[5]. Moreover, the understanding of the size dependent electrochemical performance and lithiation of alloy anodes[6] would not have been possible without advances in nanoscale imaging. The development of nanometer sized transistors

(finFETs) that can pack enough computing powers for battery management system essential for electric cars, as well as monitoring systems for utility scale solar plants would not have occurred without the advances in nanotechnology. But the most important advancement has been towards materials science and specifically instrumentation. This has led to a profound understanding of how materials respond under electrochemical, mechanical and chemical stresses which can be used to develop better devices and technology.

Hence my thesis work at UC, San Diego has explored the close connection between nanoscience and energy (batteries, solar cells and nanoelectronic devices), through the use of atom probe tomography (APT). APT can enable 3-D visualization of the chemical composition of various elements at the nanoscale. Such an analysis has helped us to better understand [1] limitations of the stoichiometry obtained from APT for different material systems and [2] applications of APT for current material challenges. Through the course of the work carried out in this thesis we have now started to create structure-property relations by combining atomistic investigation at the nanoscale with device property at the macro-scale to better understand energy devices.

Chapter 1 as mentioned above gives a brief introduction as to how energy is an important global challenge and how nanoscience can help solve some key issues. **Chapter 2** introduces the 3 aspects of energy (generation, storage and automation) in greater detail with a specific focus on working mechanism, materials and devices used specifically for each case. **Chapter 3** introduces the details of

the technique used, atom probe tomography with description for sample preparation, working mechanism, and reconstruction details. **Chapter 4** discusses APT and TEM analysis of finFET for 14 nm commercial devices for both PMOS and NMOS devices. A comparison between the thickness measurement of the different fin and dielectric layers between the 2 different techniques is provided to ensure better reliability in APT results. **Chapter 5** discusses the fundamental investigation of the laser energy parameter on the cathode pristine particles for NCA. A comparison with NMC811 is also carried out. **Chapter 6** relates to the applications of APT towards silicon anodes in order to study lithiation mechanisms involved. **Chapter 7** discusses applications of APT towards perovskite solar cells and understanding degradation mechanism that originate in the hole transport layer. **Chapter 8** summarizes the overall work and provides ideas and avenues for future research.

Chapter 2 : Different aspects of Green Energy

Green energy encompasses a very diverse set of technologies that require concerted efforts from experts in different fields. The current issues are multifaceted, ranging from individual device performance, materials challenges and device integration to global and local policy[7]. However, research efforts are continuously needed to improve on and develop breakthrough technologies. To achieve this, a fundamental understanding of the underlying working mechanism, both at the materials and device level is necessary. Moreover, understanding of the current state-of-the-art for different device types and methodologies developed is also essential. Each technology will have significant advantages and disadvantages over the other, which can help to pick the right one for the required application. Such an exhaustive picture can then help to identify challenges for each technology and application and enable efforts that can be taken to overcome them.

2.1 Energy generation through renewables

Renewable energy sources can help power the world by leaving a minimal carbon footprint during the generation process, unlike burning coal and natural gas. While different sources exist such as wind, geothermal, tidal, hydroelectric and biomass, solar energy is the only one, that as a single source, can meet the word energy needs and continue to do even with any increased projections for future needs[8] (Figure 2.1). Moreover, it provides a perennial source with the ability to be integrated both on the utility scale and at the residential level. Current solar

technology provides ~25% conversion efficiency[9], leaving out 75% of the energy untapped. With a theoretical limit of 30% for single junction devices[10], which is very close to currently obtained efficiencies, the attention is geared more towards reducing the cost, such that solar energy can compete with traditional coal/gas-based plants. Novel low-cost technologies are hence required to enable a complete replacement of fossil fuels.

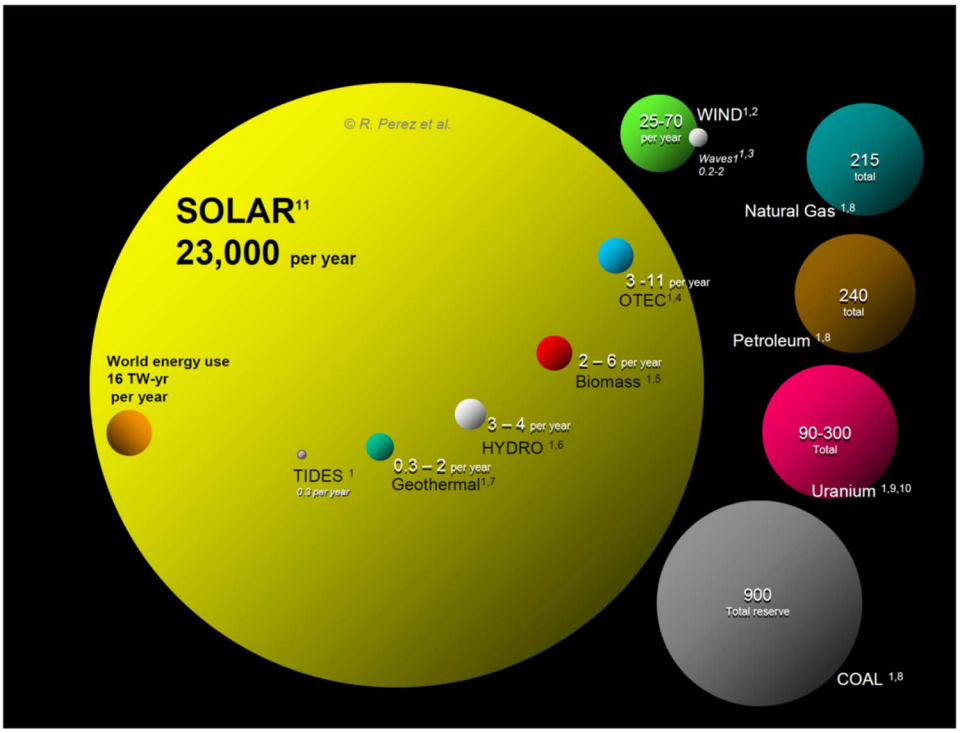

Figure 2.1: Energy reserves for renewable sources as compared to conventional sources and nuclear fuel[8].

Solar thermal systems and photovoltaic systems both convert sunlight into useable energy. Solar thermal works by using concentrated mirrors that convert the heat from sunlight into energy by heating a fluid that can in turn then run a turbine/generator. Due to the presence of a fluid reservoir, energy storage and

energy generation both happen together[11]. On the other end, photovoltaics convert photons from the visible spectrum of light into electron-hole pairs using doped semiconductor films, that are fabricated to form a p-n junction. In this case, energy storage occurs separately. Although solar thermal has an efficiency of ~ 70%, it requires larger land area use and higher costs compared to photovoltaics. Also, turbines parts can lead to wear and tear, that require continuous maintenance. On the other-hand photovoltaic plants are easier to build. Hence my work in this aspect has focused on photovoltaics.

2.1.1 Photovoltaic devices

Photovoltaic devices have traditionally used silicon as the active material for photon to electron conversion. As shown in Figure 2.2, when photon energy in excess of the bandgap of the material hits the p-n junction, electron hole pairs are formed. The electrons are swept across the depletion region into the n doped region where they travel through the current collector to the external circuit. Similarly, the holes move across the p doped region as the majority carried and complete the external circuit through contacts to provide a current[12].

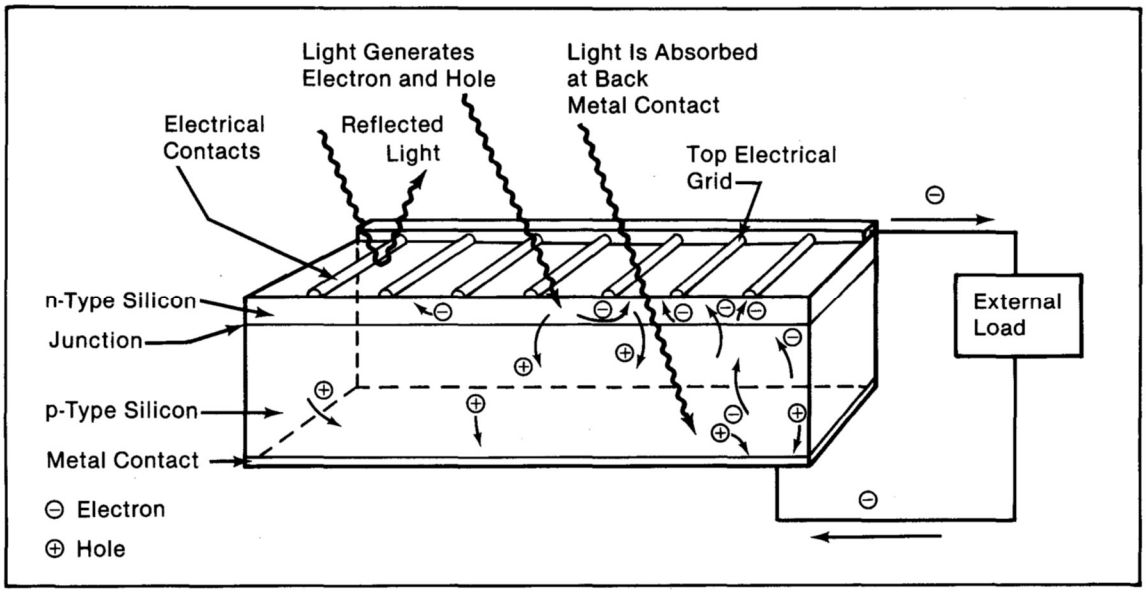

Figure 2.2: Basic working mechanism of a solar cell based on a p-n junction with pathways for recombination shown[13].

With over 3 decades of research, silicon-based photovoltaics have reached >25% power conversion efficiency in single junction devices. This was achieved with improvements in the current collector geometry through interdigitated electrodes and increase in silicon optical path lengths through surface texturing[14]. Recently though limited by the high costs involved with preparing high quality single crystalline wafers for silicon solar panels coupled with the high demand of pane;s, which could no longer be supplied by feedstock from the semiconductor industry[15], thin film solar panels (amorphous Si (a-Si), CIGS – Cadmium indium gallium selenide and CdTe- cadmium telluride) have come into prominence. They provide lower costs coming from simple roll to roll processing on flexible plastic/foil sheets. Moreover, both CIGS and CdTe have high absorption coefficients and bandgap ~1.45 eV, which is closer to the ideal of ~1.5 eV, as compared to silicon

at ~1.1 eV. However, the materials availability especially for In for large scale operations have created roadblocks for further commercialization. Cd is also toxic in itself but not CdTe, creating recyclability issues, especially in developing countries if any Cd is leaked into the environment[15].

Moreover, investments in high epitaxy techniques such as MBE (molecular beam epitaxy) to grow multijunction devices that can be tailored to absorb the solar spectrum in a wider electromagnetic spectrum window can provide over ~40% power conversion efficiency but are expensive for residential and commercial use. Hence new materials are required that can allow low cost and high power conversion efficiencies.

The power conversion efficiency of a solar cell η is given by the open circuit voltage V_{oc}, the short circuit current Isc, the fill factor FF and the input power P_{in} from the solar spectrum as:

$$\eta = \frac{V_{oc} I_{sc} FF}{P_{in}}$$

Where the fill factor is given by the ratio of the maximum power obtained to the ideal power obtained as a product of V_{oc} and I_{sc}.

2.2.2 Perovskite Solar Cell

Perovskites made of a hybrid organic-inorganic material, have over the past decade created a feverish interest in photovoltaics, with attractive optoelectronic properties. Developed from dye sensitized solar cells (which used a thin layer of dye as the absorber) by Miyasaka group[16], perovskites provide advantages of low

cost, low-temperature solution processing, high defect tolerance, direct bandgap, long carrier diffusion lengths, ambipolar transport and high absorption coefficients in the visible region[17–19]. Within a span of 10 years, the power conversion efficiencies of perovskite solar cells have reached over 20%[20–23] at the laboratory scale and over 15% for large scale modules[24].

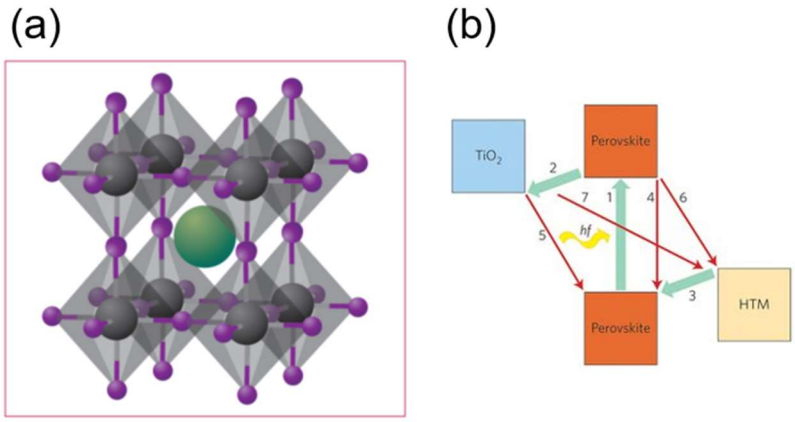

Figure 2.3: (a) Perovskite structure of the type ABX_3 where A is the organic cation (in green) usually methyl ammonium or formamidinium, B is the inorganic cation (in gray) usually Pb or Sn or a combination of it and X is the halide ion (in purple) typically I or Br or a combination[18]. (b) shows the working mechanism of a perovskite solar cell, with possible recombination pathways in red[17].

The structure consists of a cubic (tetragonal at room temperature) lattice ABX_3 as shown in Figure 2.3 (a). The organic cation (A) is situated at the body center, the inorganic cation B is at the vertices and the halide ion X is located halfway between each of the edges. Unlike a p-n junction solar cell, the mechanism here consists of a p-i-n (or alternatively n-i-p , based on device architecture) junction type where the intrinsic perovskite layer converts photons of appropriate energy (above its bandgap) into electron hole pairs (Figure 2.3 (b)). These are then transported to the selective charge collectors and subsequently to the contacts to

complete the circuit[25,26]. The movement of electrons and holes as it occurs in a working device, is shown in Figure 2.4 (b).

Traditionally, methyl ammonium lead iodide ($CH_3NH_3PbI_3$) has been the choice of active material. TiO_2 (titanium dioxide) is used as the electron transport layer with a mesoporous scaffold used for transport and a compact layer to reduce recombination effects. The entire device stack with the materials is shown in Figure 2.4 (a). FTO (fluorine doped tin oxide) is the current collector for the electron side. For the holes, an organic layer consisting of SpiroOMeTAD, with LiTFSI (Lithium bis(trifluoromethanesulfonyl)imide) and tBP (tert-butyl pyridine) as additives forms the hole transport layer. This is followed by Au (gold) contacts as the current collector layer on the hole side[17].

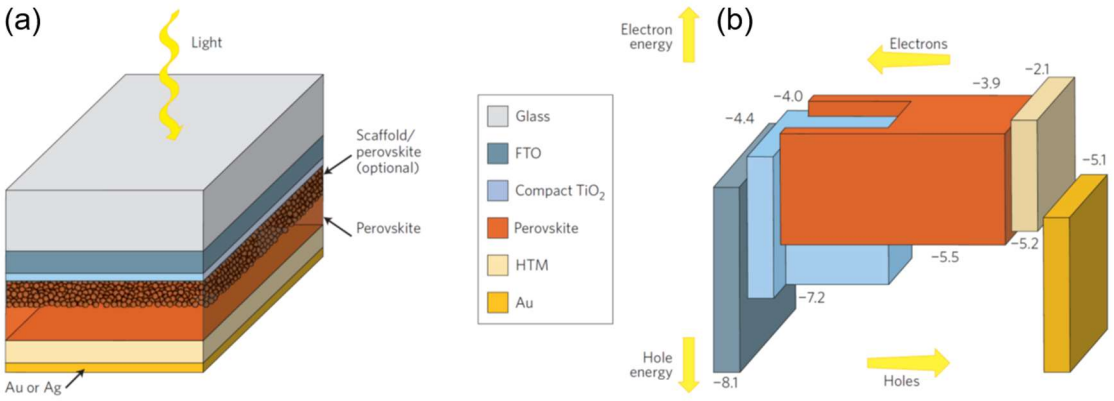

Figure 2.4: (a) Typical device architecture for a perovskite solar cell. The mesoporous scaffold can be TiO_2 or Al_2O_3 and it can be an optional layer also based on the architecture used. (b) The band alignment for each layer in the device stack showing the movement of electrons and holes from the absorber (perovskite) to the charge collector layers and then the contacts[17].

Since its introduction in 2008, several different materials for the electrodes[27–30], different device architectures and more variants and combinations

of the organic cation and halide ion for the perovskite absorber have been developed[18,19,31–33]. This development can be attributed in part to address stability issues in perovskite solar cells, both at the material and device level that are preventing commercialization. Environmental stimulants such as moisture, temperature, UV light and oxygen have also been seen to affect the perovskite material directly[34]. This high sensitivity is largely due to [1] the low formation energy of the perovskite compared to the reactants; lead iodide and methyl ammonium iodide[35] and [2] susceptibility of the organic cation to react with moisture through a sublimation process, leaving behind PbI_2[34]. In this respect, cationic substitution with Cs, FA (formamidinium), Rb and other larger species have been explored both for 2-D and 3-D perovskites, to create more thermally resilient and less moisture sensitive films. Moreover, mixed halide perovskite with Br-I as well as Br based perovskites can provide tuning of the bandgap and optical absorption[36]. These numerous modifications however also either lead to lower power conversion efficiencies or are themselves unstable and prone to degradation. This is especially true for organic species.

Of prime importance then is degradation of perovskites in moisture that can lead to rapid conversion back to PbI_2 within 24 hours. While thermal, oxygen and UV light degradation can be mitigated by appropriate cooling systems, sealing of devices and photon down conversion mechanisms respectively, moisture control over typical lifetimes of 20-30 years is more difficult. While the role of moisture during device fabrication is more debatable with reports showing that relative

humidity (RH) levels even up to 50% can lead to dissolution of the perovskite and better recrystallization and mass transport,[37–39] the effect of moisture in device degradation is unilateral in that perovskites degrade rapidly in presence of moisture[40,41]. The reaction mechanisms (as shown in Figure 2.5) and the formation of reversible monohydrate phases has also been reported[42,43].

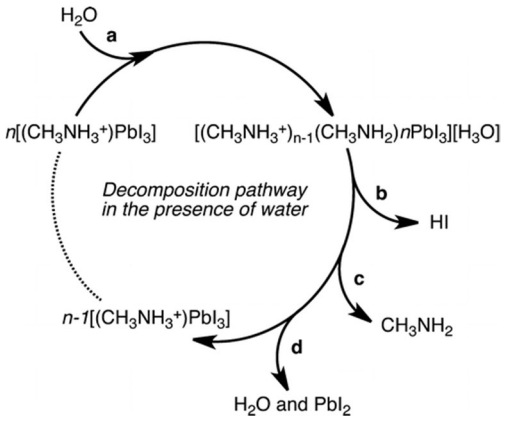

Figure 2.5: Schematic showing the degradation pathway for methyl ammonium lead iodide in presence of moisture[42].

In a complete device stack though, protection to moisture can be achieved either by more efficient sealing technologies or alternatively better material engineering that can act as a moisture barrier[44]. In order to achieve the latter, understanding the pathways for degradation in a complete device stack are necessary to ensure longer device lifetimes. As such rapid decay in power conversion efficiencies have been observed for device stacks where the perovskite material itself is not directly exposed to moisture due the hole transport layer and Au contacts above it[40,45]. A clear picture of the degradation here coming from a device perspective was hence missing, which was elucidated through our work and a few other groups at the same time[41,46,47].

2.2 Energy storage using Li-ion battery

The intermittency of energy generation through photovoltaics, due to the day and night cycles, as well as the need for stored energy for various other applications (portable tools, vehicular transport and electronic devices) have led to the rapid development of energy storage technologies.

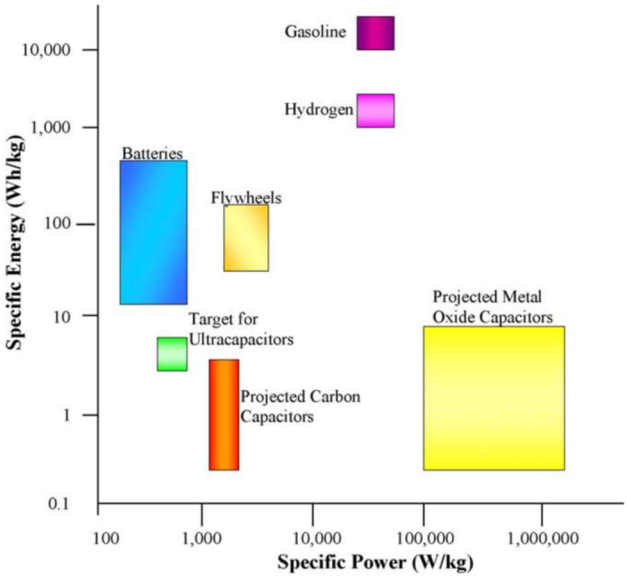

Figure 2.6: Comparison of energy storage technologies that satisfy different specific energy and power requirements[48].

While storage options are wide and varied (pumped hydroelectric, lead acid, flow batteries, Li-ion, compressed air, compressed hydrogen gas) based on the energy and power requirement[48], the current market for electrochemical storage based on Li-ion batteries has taken the forefront. Figure 2.6 shows the large range of energies that different battery technologies can satisfy, with only hydrogen and gasoline storage providing higher energy. Supercapacitors can provide high power

that are usually not required for a long duration and can be switched over to batteries for more sustained energy applications. In this respect, Li-ion batteries provides advantages of high energy density (compared to other primary and secondary battery chemistries), resilience to deeper discharge (compared to lead acid batteries) and safer, quiet running than compressed air and compressed hydrogen gas[49,50]. Led by improvements in cell chemistry and design, the penetration of Li-ion batteries is now ubiquitous globally.

2.2.1 Working mechanism of Li-ion batteries

The underlying source for electrochemical energy storage consists of the conversion of chemical energy stored in bonds (chemical potential) into useable energy in a reversible manner. Li-ion batteries are based on the concepts of a redox reaction, where oxidation occurs at one electrode and reduction at the other that are separated by an electrolyte medium. As shown in Figure 2.7, a typical Li-ion battery consists of both cathode and anode, the cathode made up of a Li containing transition metal oxide and the anode consists of graphite or a graphite-silicon (5-10%) blend. These electrodes are separated by a porous separator that prevents any direct contact between the electrodes and a liquid electrolyte that allows ionic conduction of Li-ion but prevents any electronic conduction.

During discharge, Li contained in the cathode is oxidized from Li to Li^+, due to the difference in the chemical potential between the anode and cathode. This Li^+ then travel to the anode inside the battery but the electrons are prevented to do so due to the poor electronic conductivity of the electrolyte. At the anode side, Li^+

is now reduced to Li taking an electron through the external circuit. Hence electronic transport (current flow) occurs in the external circuit driving the load and ion transport occurs inside the battery. During charge, the Li is oxidized at the anode and reduced at the cathode, due to an external driving force[51].

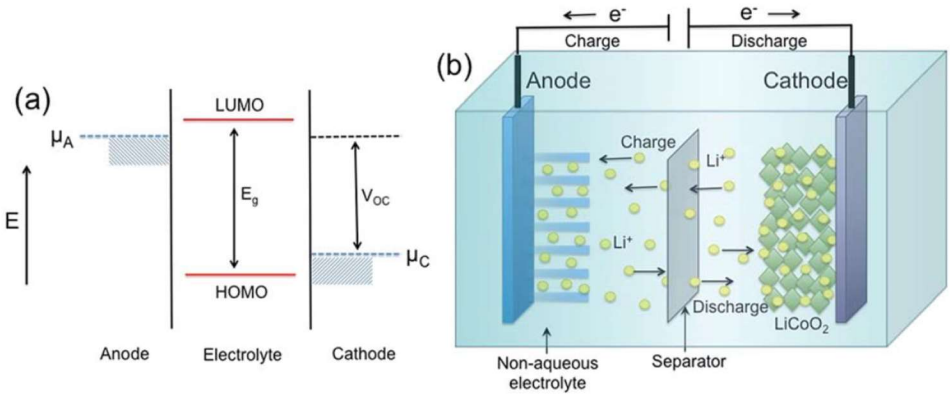

Figure 2.7: (a) Schematic showing the anode and cathode chemical potentials responsible for the driving force for ionic movement and (b) working mechanism of a Li-ion battery under charge/discharge conditions[51].

Since the redox reactions are driven by the chemical potentials, they are thermodynamically controlled. The theoretical specific capacity can also be determined based on the number of electrons transported and the molecular weight based on Faraday's law as

$$Q = \frac{nF}{3600M_w}$$

Where, *Q* is the theoretical specific capacity in mAh/g, *n* is the number of electrons transferred. *F* is the Faraday constant given by 96,500 C/mol and M_w is the molecular weight of the electrode.

While theoretically the obtained potentials and the specific capacity can help estimate the maximum energy that can be obtained, practically the materials stability under lithiation and de-lithiation is an important factor to be considered. The practical capacities obtained are hence a function of the amount of Li that can be extracted reversibly without material degradation. Moreover, side reactions between the electrode and electrolyte under applied potentials can be detrimental to the battery performance and capacity retention. Hence understanding material stability and interaction under different conditions is necessary for future battery development.

2.2.2 Cathode materials

Since the introduction of $LiCoO_2$ (LCO) by Goodenough[52] and commercialization of Li-ion batteries by Sony in 1990, the cathode has seen transition across different material chemistries. Driven by the high cost (due to Co), low thermal stability, low practical specific capacity of LCO (~135 mAh/g[53]) and capacity fade during deep discharge (>50% Li, 4.2 V), $LiNiO_2$ (with the same crystal structure as LCO) was introduced as the alternative. This was due to its high specific capacity (~175-200 mAh/g[54]), attributed to Ni, and low cost. However, the low thermal stability (due to ease of Ni^{3+} reduction compared to Co^{3+}) and high ratio of Li/Ni intermixing which interfered with Li pathways rendered this compound unstable and Co and Mn were introduced, Co for structural stability and rate capability and Mn for low cost and safety[3,53]. This gave rise to the field of layered

oxides- $LiNi_xMn_yCo_zO_2$ (NMC) that are currently being used for both portable electronic and electric transport applications.

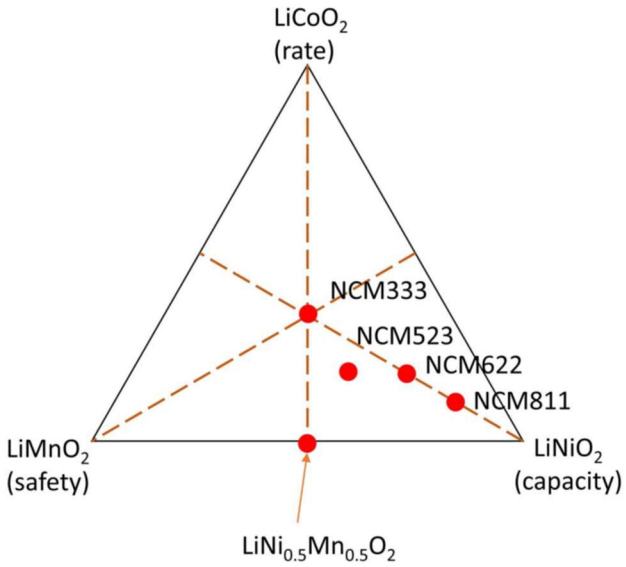

Figure 2.8: Schematic showing the different NMC compositions currently used and under development.

The 2D layered (R3m) structure allows for a planar channel for Li ion transport. Unlike other materials such as $LiNi_{0.5}Mn_{1.5}O_4$ (LNMO) with 3-D transport channels and $LiFePO_4$ (LFP) and $Li_4Ti_5O_{12}$ (LTO), NMC offers stable operating voltages until 4.3V, high specific capacity, low cost and environmental stability and an ability to tune the composition for higher capacities (Figure 2.8); a combination of which is not possible with other compounds.

Replacing Mn with Al can improve the thermal stability, capacity retention as well as the specific capacity at high Ni content, which is not currently achievable using the NMC. NCA ($LiNi_{0.8}Co_{0.15}Al_{0.05}O_2$) has hence gained prominence as the cathode material of choice (Figure 2.9). Moreover, patent issues[55] in US related to NMC have also hindered their growth to some extent.

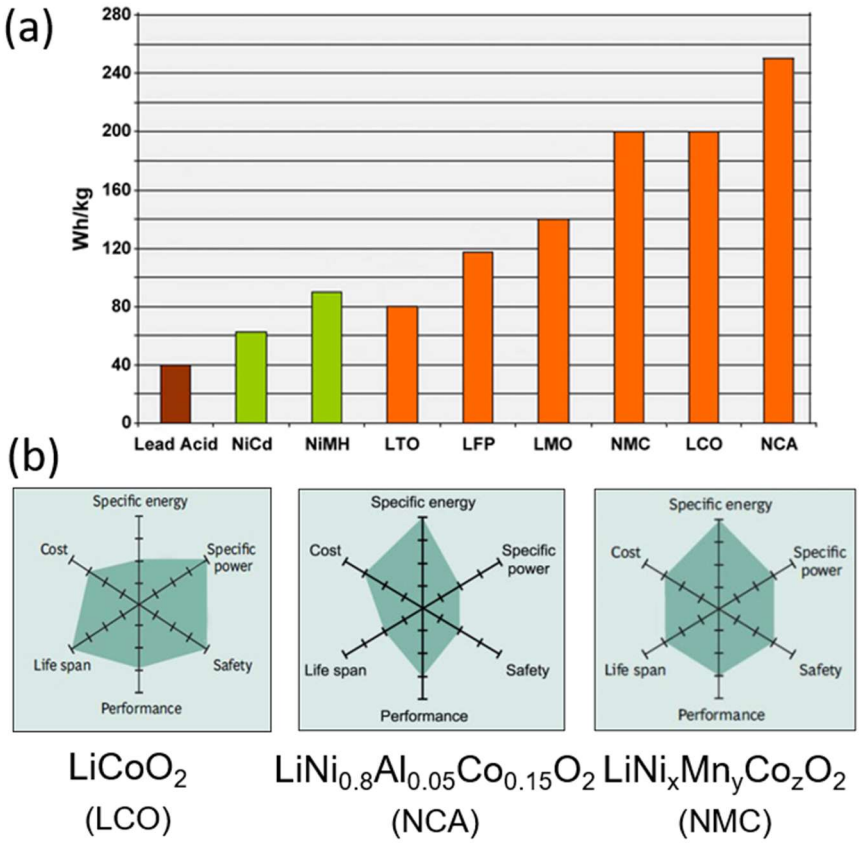

Figure 2.9: (a) Comparison of the energy density for different cathode materials compared to traditional lead acid and NiMH technologies. (b) Spider chart showing different metrics for comparison between LCO, NCA and NMC[56] .

While the role of Ni and Co has been extensively studied for NCA, with a change in the Ni oxidation state from the surface to the bulk leading to NiO rock salt formation, the role of Al is not clearly understood[57–59]. However, its effect on electrochemistry is clear, with both Al coated[60] and graded NCA cathodes[61] leading to improved capacity retention compared to traditional NMC cathodes. To this effect, the low concentration (5%) and low Z (atomic number) of Al has prevented its nanoscale study using other techniques, such as scanning electron microscopy (SEM), Focused ion beam (FIB) and transmission electron microscopy

(TEM). Understanding and observing the exact stoichiometry, is hence necessary to elucidate how Al affects the structural stability and participates in the longevity of NCA cathodes.

2.2.3 Anode materials

Amongst the anode materials, graphite has conventionally been the material of choice due to its low cost, low operating potential with Li and high abundance. The intercalation of Li into the 2D graphite planes provide low volume expansion (<5%), that allows reversible Li transport, thus providing high capacity retention. However, the specific capacity of ~ 372 mAh/g which was sufficient for portable devices can no longer fulfill applications towards grid storage and electric vehicles. The intrinsic specific capacity of the anode needs to be higher to allow higher volumetric energy densities in a battery pack.

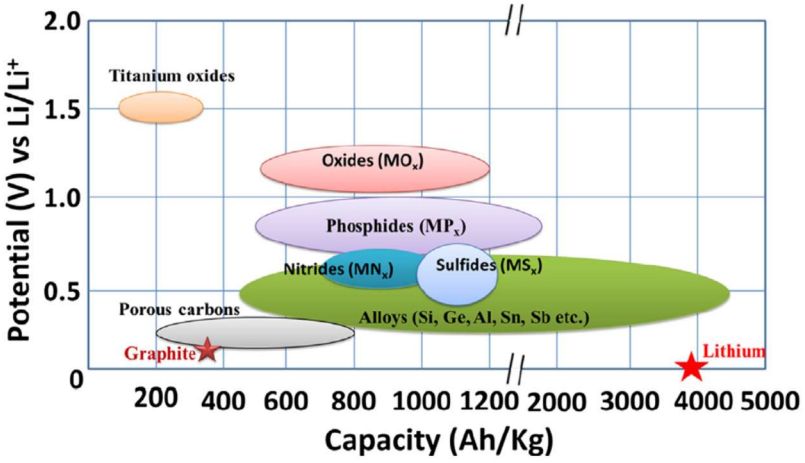

Figure 2.10: Comparison of the specific capacity and potential for different anode materials[6].

Alloy anodes, which allow more than one Li atom to alloy with it (compared to intercalation of one Li ion per 6 C atoms) allow for higher specific capacity. As shown in Figure 2.10, silicon can provide advantages that are similar to graphite with cost, operating potential and availability but like other alloy anodes, it suffers from larger volume expansion during lithiation (~300%)[4,62,63]. This severely impedes its capacity retention (Figure 2.11). To mitigate the effect of volume expansion on the electrode level, multiple different strategies have been employed from binder engineering[64–68] (with tailored functional groups for enhanced mechanical, adhesive and self-healing properties), to carbon coatings[69–72] and morphological shape and size control[62,73–75] for the silicon particles. However, translating these improvements, which are mostly seen in half-cell configuration against Li metal, over towards full cells have been a challenge still.

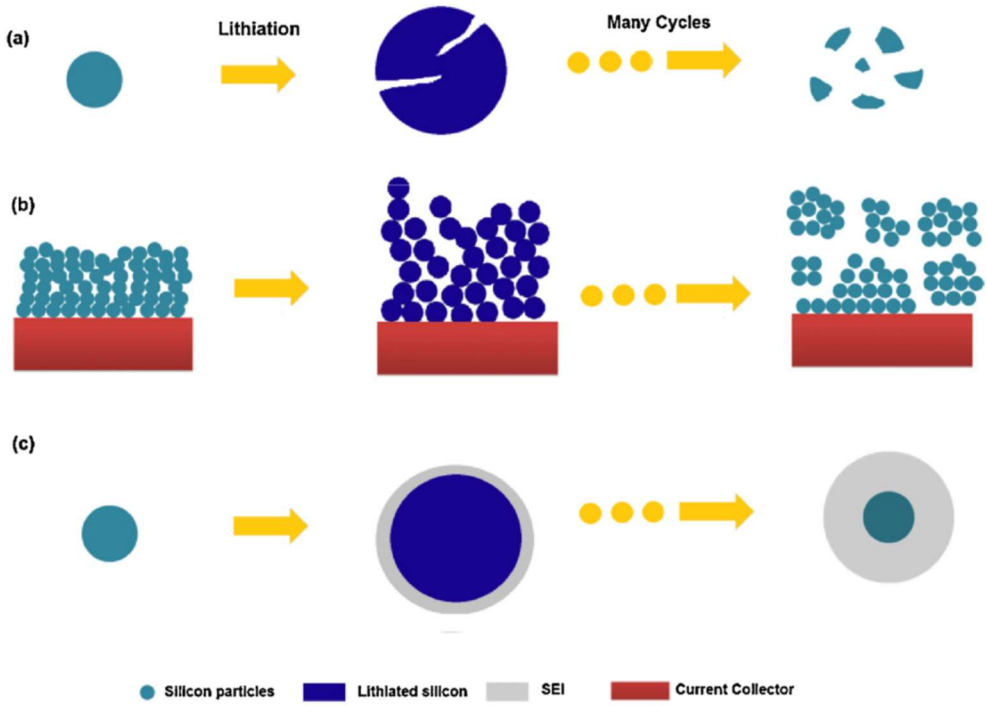

Figure 2.11: Failure mechanisms on silicon anodes due to its volume expansion, that lead to [a] pulverization of individual particles, [b] loss of electrical contract from the current collector and [c] consumption of electrolyte to form thicker SEI layer[76].

This is primarily due to the continued consumption of Li in the first cycle and on subsequent cycles due to the associated volume expansion. To better understand the fundamentals of the lithiation mechanism, in-situ TEM has been used to observe a reaction front between silicon and lithiated silicon[77–80]. It has been also been proposed that a high concentration of Li is needed at this interface to break the crystalline silicon interface[81]. But a direct observation of the lithium distribution is still missing, which can complete this understanding.

Moreover, direct Li distribution can allow a better understanding of how this stress propagates across the interface and what are the most critical parameters

that affect the volume expansion. This can provide clues for modifying the material structure further for enhanced capacity retention.

2.3 Monitoring, management and automation using semiconductors

Since the introduction of the field effect transistor, the semiconductor industry has seen the fastest growth in nanotechnology. Keeping up with Moore's Law[82], the average transistor size has decreased every 18 months with the current technology node at 10 nm for the channel length. A fundamental shift in the development occurred with the introduction of the finFET structure[83] where a 3-D fin was developed as the channel, instead of the planar structure, that allowed a better modulation of the channel current through the wrap around gate dielectric and gate contact. While these improvements have happened independent of the energy space, their role started to overlap with development of larger battery packs (for grid and electric vehicles) that require efficient management and monitoring systems. Battery management systems (BMS) were hence developed and deployed to identify the state of charge and health of individual cells and make real-time modifications to the charging protocols, to ensure high mileage with minimal materials degradation. This real-time monitoring and feedback control through efficient still requires advancements in understanding the limitation in current semiconductor technology.

With the introduction of finFETs, the ability to observe the dopant profiles and the 3-D stack of the fin-gate dielectrics and gate contacts at each technology node is necessary to allow further improvements. Moreover, defects that occur

only under certain testing parameters (soft defects) need advanced characterization techniques to correctly identify their source at the nanoscale. For instance, both TEM and APT correlative studies have been carried out on planar FETs[84] and on individual dielectric layers[85,86] to see the distribution of elements in each layer. However, for a controlled study, targeting of the fins and observation of both PMOS and NMOS devices at the current technology node is needed.

Chapter 3 : Advanced Nanoscale Characterization

Current advances in the green energy sector require nanoscale characterization, with high spatial resolution and high chemical sensitivity. For instance, finFET channels lengths are between 10-15 nm and 3D in nature[83,87]. Li-ion battery cathodes such as NCA consists of Al in small stoichiometric amounts (~1-2%), and NMC cathodes are increasing being modified with surface coatings that are a few nanometers thick[3]. Moreover, NCA cathodes with graded composition have also been developed[61]. Photovoltaics on the other end consists of multiple interfaces whose interactions are necessary to understand for better device lifetime.

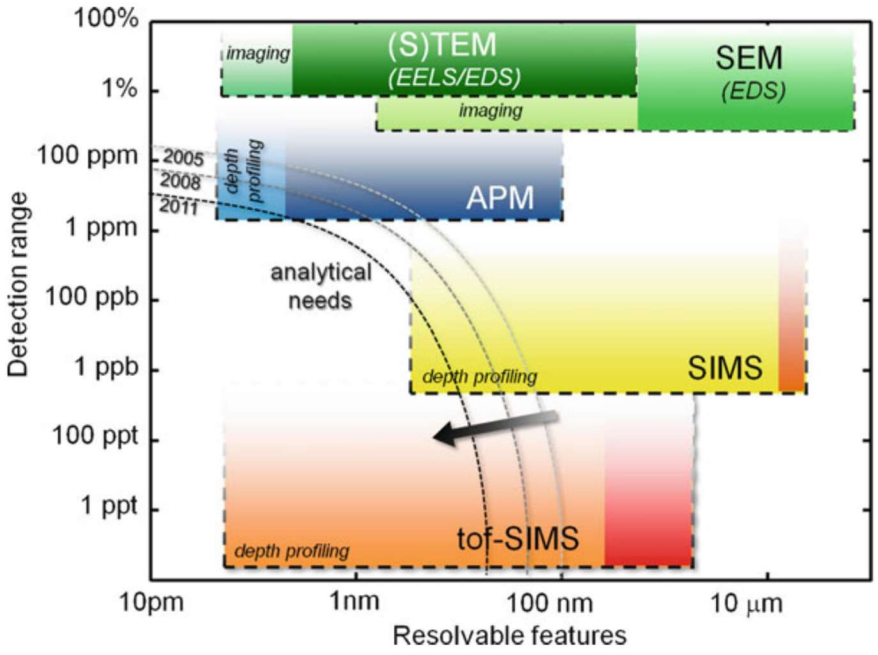

Figure 3.1: Comparison of the spatial and chemical resolution of various nanoscale based techniques with atom probe microscopy (APM)/atom probe tomography (APT)[88].

A host of different techniques exist that can provide either spatial or chemical information with nanometer resolution. Transmission electron microscopy (TEM) gives atomic resolution in 2D averaged over 100 nm or less. Using electron energy loss spectroscopy (EELS) and energy dispersive x-ray spectroscopy (EDX) gives chemical information in 2D with a sensitivity of ~1%. In the realm of nanoscale analysis, scanning electron microscopy (SEM), X-ray diffraction (XRD), Raman and IR spectroscopy all fall into macroscopic analysis techniques. Secondary ion mass spectrometry (SIMS) provides chemical information as a function of depth, with parts per million (ppm) sensitivity, but loses x-y spatial resolution.

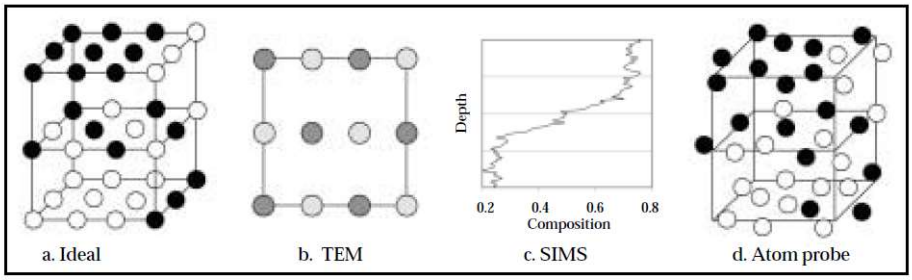

Figure 3.2: Comparison of the information obtained from APT versus what can be seen with TEM and SIMS[89].

Amongst the suit of different spectroscopy/spectrometry and microscopic techniques, APT lies in the regime between SIMS and TEM for combined spatial resolution and chemical sensitivity (Figure 3.1). APT can provide ~1-10 ppm chemical sensitivity, ~1 nm spatial resolution (better for metallic systems) and equal detection efficiency (>50%) for all elements, including H and Li. APT is

however, unique due its ability to observe buried interfaces, graded compositions at the nanoscale and true 3D information[90] as shown in Figure 3.2.

3.1 Working mechanism

APT derives its name from probing atoms (or small clusters of atoms) by tomographic 2D projections that are converted to a 3-D map. The basic working mechanism is shown in Figure 3.3. It consists of a needle shaped specimen, with an apex radius <100 nm that undergoes field evaporation of ions under the application of a base DC voltage and a pulsed laser (for oxides, semiconductors and ceramics) or a pulsed voltage (for metallic materials). The specimen is cryogenically cooled (~30-40K), to minimize atomic vibration, and the combination of a nanoscale tip radius and a local electrode allows for electric field lines to be perpendicular to the tip surface. The laser/pulsed voltage causes field ionization and ultimately the ions are emitted from the tip surface.

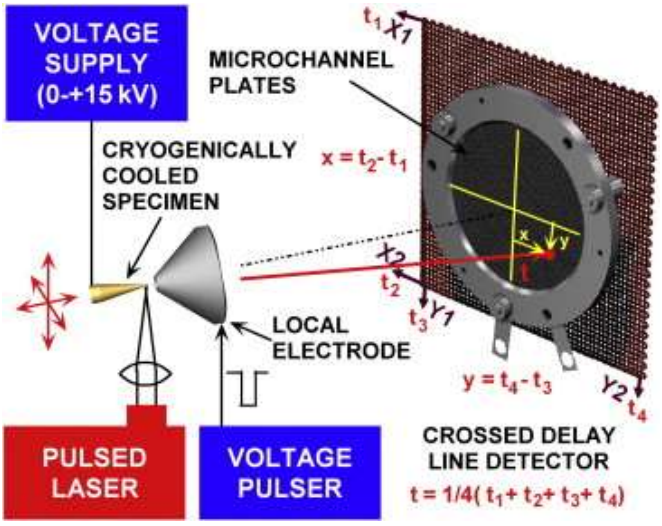

Figure 3.3: Schematic showing the mechanism for APT[91].

These ions are then accelerated in the electric field from the local electrode and reach a cross delay line detector (with a microchannel plate) to uniquely identify the x and y position of the emitted ion. The pulse rate is also controlled to allow less than 1 ion to evaporate per pulse and enable a z height determination. Simultaneously a time of flight measurement, from the time the ion was emitted till it hits the detector screen is also recorded to provide chemical species identification, through a mass/charge ratio.

3.2 Sample preparation

In order to ensure that the ions can be emitted from the specimen surface, they need to be prepared specifically into a needle shape with nanoscale apex radius. Hence specimen preparation, which is usually done using other techniques is a very important aspect of APT. Specimens are usually prepared using 3 different methods [a] electropolishing, [b] using a shadow mask and [c] using focused ion beam (FIB/Dualbeam)[88,92,93]. Electropolishing is more reserved for metallic samples. In brief, a bulk sample is cut into smaller rectangular pieces which act as one of the electrodes for the electropolish. A counter electrode and an electrolyte are then used to thin the sample at the electrolyte meniscus on application of a potential. The setup used is shown in Figure 3.4 (a)[92]. The sample is thinned till a neck region is formed and the thinning continued to allow the neck to break and form a tip. This method is more conventional, works best for metallic samples that can act as an electrode for the electropolish and does not allow any site-specific preparation.

The shadow mask consists of a mask pattern that is imprinted onto the sample using Ar sputtering[94], allowing for large scale preparation of specimens (Figure 3.4 (c)). This is however followed by a second sharpening step to achieve the final tip shape, which requires an ion beam instrument that can process one tip at a time. Hence this also loses any site specificity.

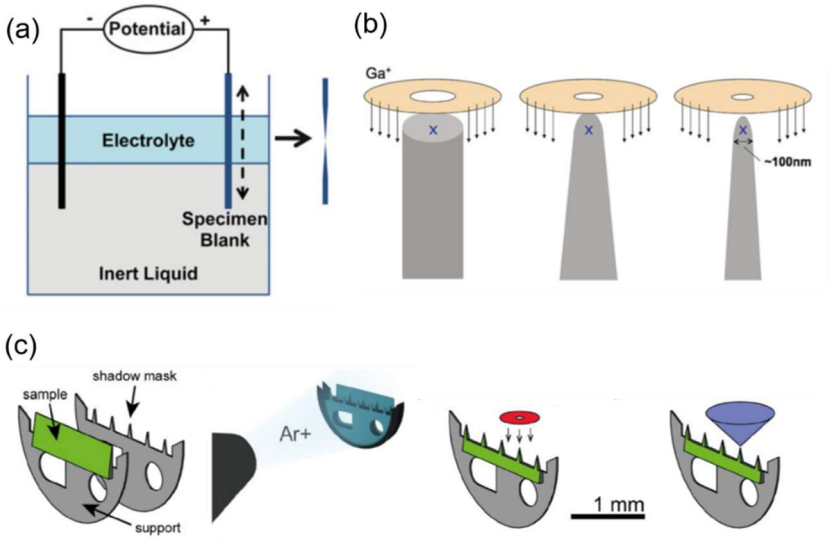

Figure 3.4: Schematic showing the specimen preparation techniques most commonly used for APT with (a) electropolishing[92], (b) FIB based liftout and tip sharpening[88] and (c) shadow mask based sample preparation[94].

Current technology though requires the preparation of specimens at specific locations, is possible using the FIB/Dualbeam instruments[88,92]. This technique though developed recently, is now most extensively used for sample preparation of oxides, ceramics, zeolites, halides and even metallic samples. A sample wedge section (milled at 22° instead of 52°) is lifted out from the bulk using micromanipulators inside the FIB, similar to TEM liftouts, and the sample wedges are attached onto individual Si microtip arrays[92]. The wedge section allows better

contact with the silicon microtip base in conjunction with Pt deposition patterns at the base, which from a stronger contact point than a physical Van-der-waal based contact (if the wedge shape was not used). Based on the length of the wedge lifted out, 5-6 samples can be prepared at a time. The individual specimens attached onto the microtip array are then milled (annular milling) to prepare the final tip shape (Figure 3.4 (b)). Each tip is then analyzed in the APT.

3.3 Running samples in the atom probe

As prepared samples are then loaded into a buffer chamber through a load lock until they are ready to be run in the system (analysis chamber). The samples are loaded into the analysis chamber using a transfer arm. The analysis chamber is set at a specific base temperature usually between 30-60 K based on the type of sample to be analyzed. The laser energy, pulse rate and detection rate are all set through the LEAP Control Center software. Any evaporation at a constant DC voltage, usually occurs at different temperatures for different elemental species present in the specimen (Figure 3.5 right panel) and any additional laser energy input can cause preferential evaporation of elements and interfere in data analysis and interpretation.

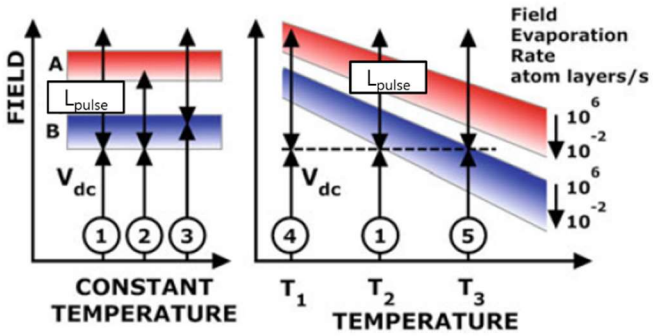

Figure 3.5: Schematic showing the need for the laser pulse and a constant temperature to prevent preferential evapaoration[93].

However, at a constant temperature, as shown in Figure 3.5 left panel, the field required for evaporation differs, which can be controlled by application of one base DC voltage and using the laser input energy to provide the differential such that this condition (extra input energy) is met for all elements thus allowing better reliability in the data. Hence the base temperature is not varied during the data acquisition.

Following this, the correct microtip identification and specimen alignment on the laser beam and with respect to the local electrode, is carried out next using the 2 optical microscopes in the analysis chamber (Figure 3.6 (a)). Once this is done, the runs are started and during runtime, at the onset of evaporation, the specimen tip location with respect to the laser is now more closely identified using a scanning feature on the software (Figure 3.6 (b)). Following this, the evaporation map on the detector screen is now aligned to make sure that the specimen ions uniformly impinge the screen and the ion information is not lost, as shown in Figure 3.6 (c). Once the alignments are finished and the required detection rate is reached, the

specimen data acquisition is put into laser tracking mode where an automated algorithm is used to allow efficient data collection.

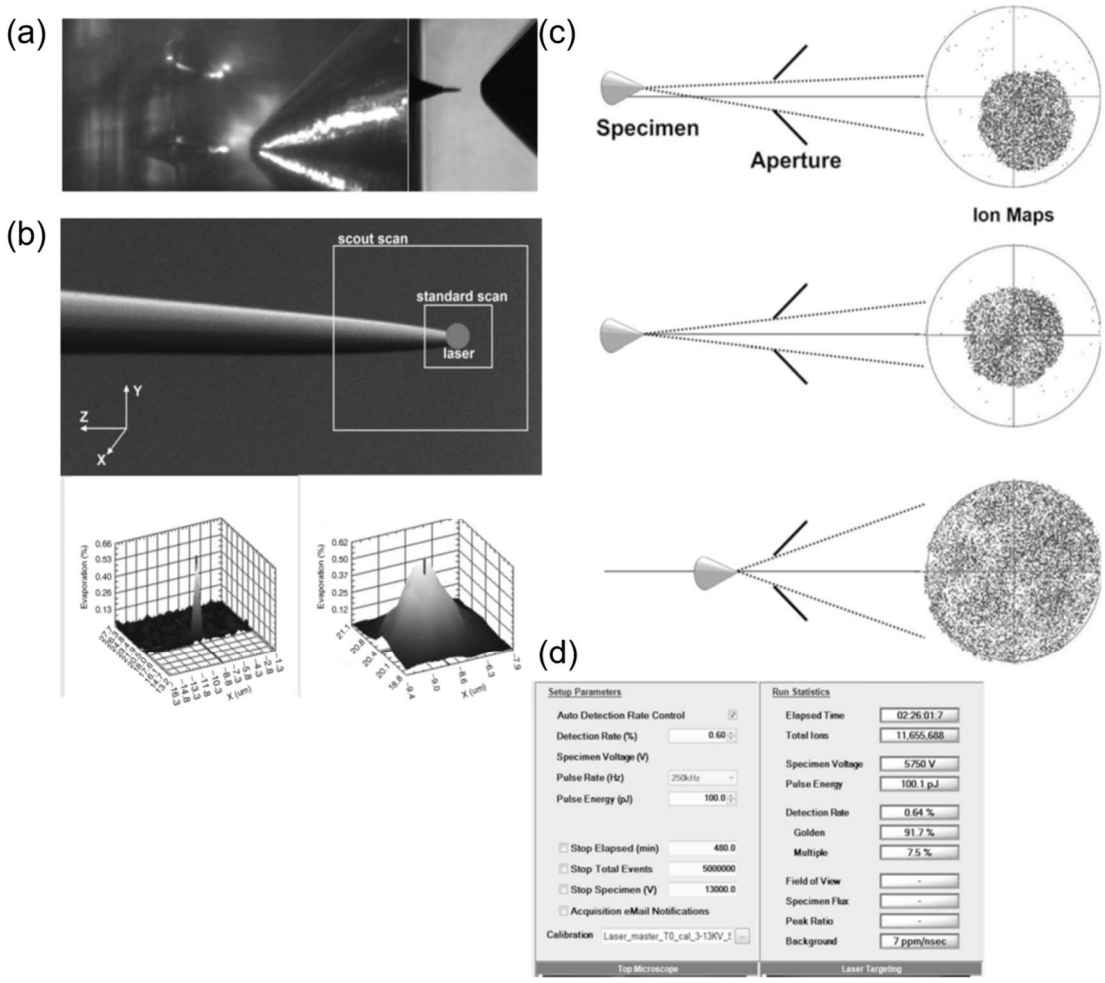

Figure 3.6: Different steps involved in the alignment of the specimen tip before and at the onset of an APT run. (a) Alignment of the correct tip with respect to the local electrode using the optical microscopes, (b) alignment of the laser on the specimen tip during run time and (c) ensuring that the detector map is uniformly illuminated with sample hits for to allow maximum data to be collected. (d) shows the LEAP Control Center software with the different parameters to be set.[93]

3.4 Instrumentation and parameter tradeoffs

Based on the pulse rate, the detection window is set up and ions that hit the screen within this window are only analyzed during the reconstruction process. A

time of flight is hence measured from the start of the detection window (which is offset from the pulse sequence, which determines the point when the ions are emitted from the surface), until the emitted ions hits the detector screen. A schematic for the time of flight measurement is shown in Figure 3.7.

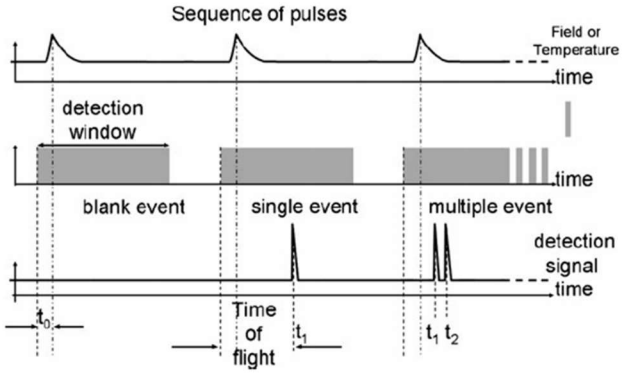

$$\frac{1}{2}mv^2 = neV \quad \text{and} \quad v = \frac{d}{t} \rightarrow \frac{m}{n} = \frac{2eV}{L^2}t^2$$

$$t_{\text{cor}} = F_V(V_{DC}) \cdot F_B(X,Y) \cdot (t_{\text{raw}} - t_0),$$

Figure 3.7: Schematic showing the calculation for the time of flight on the instrument side and the relevant equations used to get mass to charge ratio and the corrections applied during the reconstruction[88]. m denotes the mass, n is the charge, e is charge on a single electron, V is the applied voltage, L is the distance the specimen tip and the detector and t, t_{raw} both denote the time of flight. F_V and F_B are both corrections discussed later.

Correction algorithms are used to account for this offset and other trajectory offsets coming from ions emitted from the hemispherical specimen hitting a flat 2-D detector. Based on the time of flight of the ions, a mass to charge ratio is obtained for each ion, which is a unique signature of the element/ complex species present. APT can provide a very high (4000 amu) resolution in the mass to charge ratio, allowing identification of different isotopes for accurate assignment of complex ions.

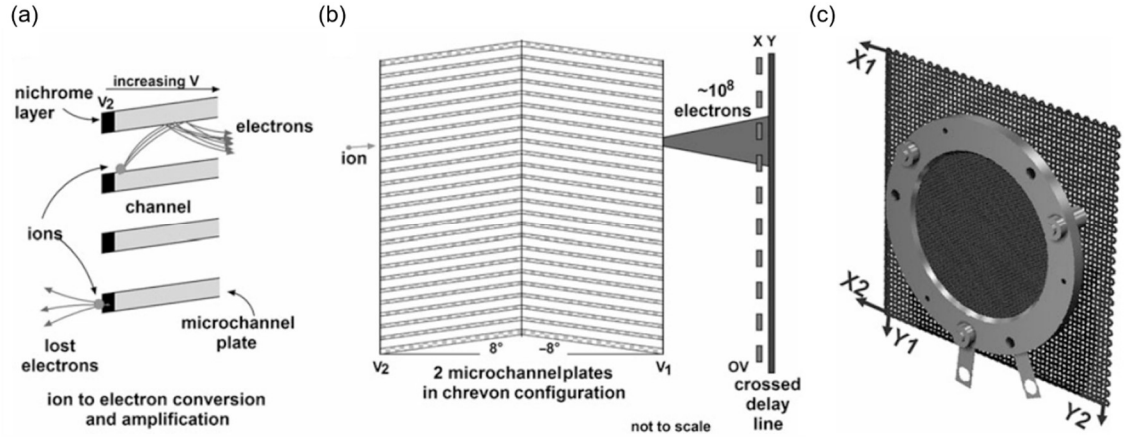

Figure 3.8: Schematic of the microchannel plate (a) and (b) and the cross delay line detector (c)

Ions impinging on the detector screen first hit 2 microchannel plates in a chevron configuration, that allows a cascade of electrons events to be produced from each ion hit, similar to a photomultiplier tube. This allows for an amplification of each ion and no loss in information from individual evaporation events (as seen in Figure 3.8 (a, b)). The electrons then hit a cross delay line detector that takes a unique amount of time for the signals to complete the circuit, based on the X and Y position of the electrons hitting the detector. This is used for x and y position identification in the specimen, through a magnification factor (Figure 3.8 (c)).

As with any instrument tradeoffs are involved in APT also. The chart in Figure 3.9 shows all the tradeoffs involved[92]. A higher pulse rate can give faster acquisition but prevents complete mass to charge spectrum to be available for analysis until higher base voltages are reached. This can lead to loss of critical information on the species present. On the other hand, a lower pulse rate can lead to very slow acquisition times. Laser energy is an important tradeoff too, with a

lower value allowing better spatial resolution but possible preferential evaporation and a higher energy giving better yield but at the cost of loss in accurate compositions or higher than usual Li evaporation rates (specifically for battery cathodes).

Acquisition parameter	Variable	General trend	Metrics	Comments	Primary tradeoff
Pulse rate ↑	f (Hz)	+ +	Background	Higher is better	Almost none except for practical considerations for TOF of all potential ion species
		−	m/n range	Exceptions: high-mass ions with long TOF or extremely poor thermal diffusivity materials in laser mode	
		−	Wrap around		
		−	Base temperature offset effects (laser)		
Base temperature ↑	T (K)	+ +	Analysis yield	Lower leads to better spatial resolution, Higher leads to better yield	Data quality vs. analysis yield
		− −	MRP		
		− −	Background		
		−	Heat flow (laser)		
		−	Surface diffusion		
Detection rate ↑	DR (ions/ pulse)	+ +	Background	Higher is better	Data quality vs. analysis yield
		−	Analysis yield	Exception: poor yielding materials and materials prone to multi-hit behavior	
		−	MRP		
		−	Multi-hit performance		
Pulse fraction ↑ (voltage mode)	PF (%)	+ +	Compositional accuracy	Higher is better	Data quality vs. analysis yield
		+	Background	Exception: Extreme PF may limit MRP and pulse amplitude is hardware limited	
		−	Potential for PF decay		
		−	High cycle fatigue		
Laser pulse energy ↑ (laser mode)	LPE (nJ or pJ)	+ + +	Analysis yield	Higher leads to better yield	Data quality vs. analysis yield
		+ +	Background	Lower leads to better spatial resolution	
		+	MRP		
		+	Effective pulse fraction		
		−	Complex ion generation		
		− −	Surface migration		

Figure 3.9: Tradeoff involved with different parameters in APT[92].

3.5 Reconstruction

The reconstruction process is carried out after sample acquisition on a separate proprietary software known as IVAS (Integrated Visualization and Analysis Software). The reconstruction follows through 6 steps and is based on a .rhit file generated during the acquisition. The first step in the reconstruction is the voltage history plot which provides a description of the base DC voltage as a function of the ion sequence number. The base DC voltage shows an exponential increase that plateaus out at higher ion numbers. This increase is due to the

broadening of the tip radius as ions are emitted from the surface, which now require more energy to be emitted. But as the tip radius increases, the number of ions emitted also increases from the same surface, leading to a slower increase in the voltage. In this step, the voltage range to be used for the reconstruction is set. The initial voltage region with intermittent features (indicative of the alignment processes followed during runtime), are removed from the reconstructed data, as shown by the shaded region in Figure 3.10 (a), which is then used for voltage reconstruction.

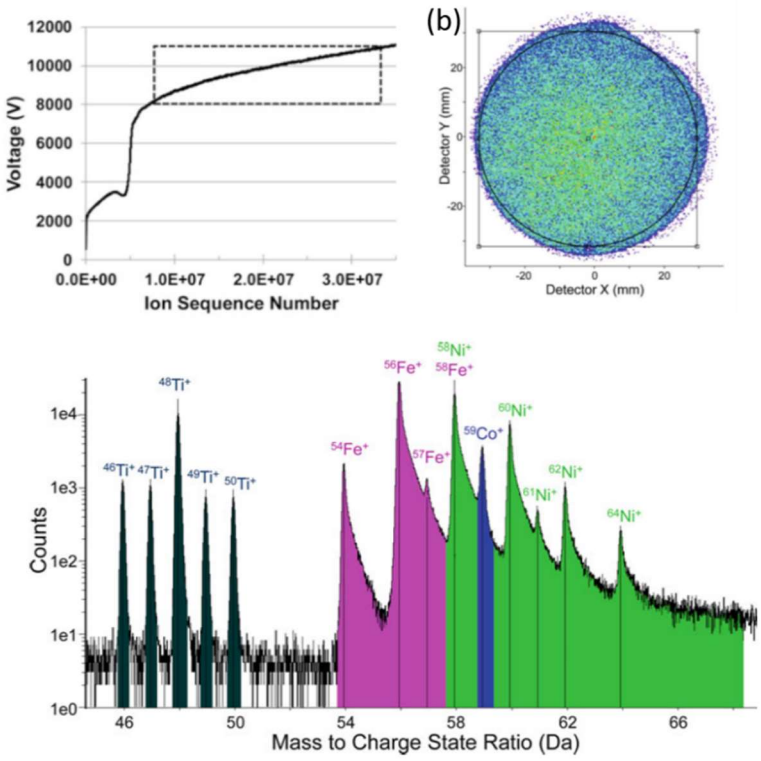

Figure 3.10: (a) Voltage history as a function of the ion sequence to identify features that are to be removed from the analysis. As shown here, the shaded region will be selected for further reconstruction. (b) Image showing the selected area of the detector map that will be used for reconstruction and (c) the mass spectrum analysis for identification of different chemical species.

Following this, the second step consists of selecting the area of the detector map that will be used for the reconstruction. The outer area of the map with sparse ion hits is eliminated too. The third and fourth steps are corrections applied to the time of flight, following which the time of flight is converted to a mass to charge ratio, based on the equation shown in Figure 3.7.

After the corrections, the last two steps are the most important for the reconstruction, the first one, is the mass ranging (Figure 3.10 (c)), which is an identification of the correct element/complex ion evaporated at a particular mass to charge ratio. For instance, a mass to charge ratio of 7 can be uniquely identified to Li^{+}. As such care must be taken to ensure [1] All species are uniquely identified, this in itself is a challenging process due to peak overlaps such as Ti^{3+} and O^{+}. However, the presence or absence of the isotopic peaks (usually present for samples not prepared from a particular isotope), and the correct ratio of the isotopic peaks can both help to circumvent this issue to a large extent. [2] The ions evaporating with one mass to charge ratio also have a peak distribution, that rises sharply and has a logarithmic decay, hence the ranging is done manually for each species from the onset of the peak to the decay of the peak into the background signals, as shown in Figure 3.10 (c). [3] Spurious single events from the background should also be analyzed with care to ensure that they are not mistakenly identified as a peak. Hence the mass ranging is a very important step in the reconstruction and needs to be carried out with utmost time. The ranging

once done, is saved and stored but can also be updated later once the reconstruction has finished.

Finally, the tip shape reconstruction is carried out. This step determines the accurate z height for each emitted ion. The reconstruction is carried out assuming a hemispherical tip shape for each specimen that descends into a cone of a fixed shank angle. Hence the tip shape reconstruction algorithms are divided based on voltage, shank angle or tip image. In the voltage-based algorithm, the voltage and the evaporation field F_e at the tip apex are used to calculate the radius R through a constant factor k_f. Each increment in voltage leads to the evolution of the radius and hence the tip, through the equation:

$$R = \frac{V}{k_f F_e}$$

In the shank angle-based reconstruction, an initial radius R_0, the shank angle α and the depth coordinate z obtained from the ion sequence number is used to calculate the evolution of the tip radius R.

$$R = R_O + \frac{\sin\alpha}{1-\sin\alpha} z$$

While both these algorithms work well with tips that conform to the assumptions of a hemispherical tip shape, more likely than often, the final tip shape does not fit this assumption. Figure 3.11 shows a tip image that is used for to create

tracers that follow the actual evolution of the tip which can then be used for the reconstruction process. The images are obtained from SEM or FIB.

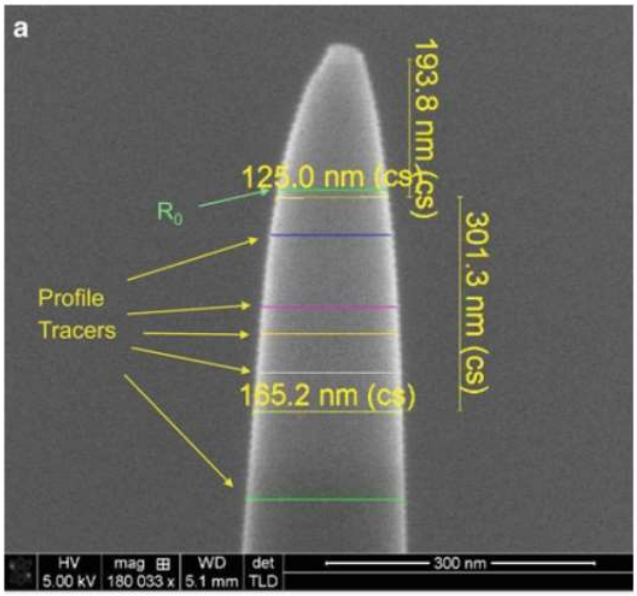

Figure 3.11: Tip profile process for the final step in the reconstruction[92].

After going through the reconstruction process, the system then generates a .pos file which can then be used for 3D visualization. Different color schemes, 3D rotations and different projections are all then used to analyze the obtained data, using the IVAS software.

3.6 Applications

While atom probe tomography is an intensive technique where the specimen is destroyed for analysis, the ability to obtain nanoscale information and at the atomic level for metallic systems has led to a host of different applications. Studying hydrogen embrittlement in steel[95], where the hydrogen distribution into grain boundaries or the bulk can make a different in the steel yield strength, studying the chemical make-up of geological materials where ppm level impurities

and nanoclusters provide clues towards formation of rocks on earth[96], semiconductor profile and dopant analysis[97] and more recently inorganic analysis of biological systems[98,99] are all are areas where atom probe tomography can be applied. The applications of APT towards energy devices, has however been limited.

Towards photovoltaics, multi-crystalline silicon panels have been explored for composition gradients on grain boundaries,[100] but more importantly heterojunction cells based on different III-V semiconductors have been more extensively explored to identify the thicknesses of each layers and homogeneity in the chemical distribution of each layer[101–103]. More recently though, multiple studies have also explored the segregation of Na and S or Se on grain boundaries in the active layer of CIGS solar cells[104–106]. These are identified to be as a result of diffusion from the soda lime substrates and lead to increased power conversion efficiencies due to passivation of vacancies at the grain boundaries. The applications of APT hence towards more novel perovskite and organic photovoltaic technology has still not been explored.

For battery materials, the field of APT is relatively new with just a handful of articles that first started with LCO[107]. Here APT was used as a complimentary technique with TEM to show the depletion in Li in the cycled samples and segregation of Li towards internal grain boundaries in LCO. Moreover, based on this initial interest, Mn based cathodes ($LiMn_2O_4$) and Ni, Co based cathodes were briefly explored before and after cycling[108–111]. $LiFePO_4$[112] and SiO[113] were also

reported once with no follow up work to investigate the materials further. However, around the same time, the effect of laser energy on the accurate stoichiometric compositions was investigated for simpler oxides[114]. This study showed the change in the atomic compositions with changing laser energy. This brought into question the quantitative accuracy of the analysis carried out for battery materials, even though the qualitative trends were verified due to correlative studies. Also, more importantly what the best analysis conditions were for each cathode oxide was necessary to explore.

Hence the field of APT was still wide open to first start to understand the material to instrument laser energy interactions before moving on to application such as nanoscale coatings, graded compositions and structural degradation from the surface to the bulk could be explored. Hence studying the fundamentals of APT towards energy materials and how the technique can be applied towards understanding next generation technology is the focus of this thesis.

Chapter 4 : Three-Dimensional Nanoscale Mapping of State-of-the-Art Field-Effect Transistors (FinFETs)

4.1 Introduction

In this era of digitalization, the ubiquitous nature of electronic devices such as phones, laptops, and smart home appliances has led to a social and economic revolution. At the core of each device is a transistor, a simple electronic switch that performs logic operations and stores data in memory blocks through intricate connections with other transistors[115]. The first transistor was invented in 1947 by Bardeen, Brattain, and Shockley at Bell Labs[116]. Since its invention, there have been numerous changes over the years with the field-effect transistor (FET) taking the forefront[117,118]. The development of complementary metal-oxide semiconductor (CMOS) technology (consisting of PMOS and NMOS; P for p-type and N for n-type, indicating the type of dopants used for the source-drain contacts) with individual FETs as either PMOS or NMOS is the current basis for chipsets used in digital integrated circuits (ICs)[119].

The FET has seen a relatively steady scaling of size following Moore's Law[82]. In effect, as the FET size scaled, parasitic capacitance between the contacts and gate became a major issue which led to new designs and materials to be used[120]. A paradigm shift occurred in 2000 with the introduction of the three-dimensional (3D) finFET technology by Dr. Chenming Hu[83]. The 3D structure with the fin protruding out and the gate wrapped around three sides allowed better control of the channel current during on/off state and also overcame the problem

of drain-induced barrier lowering, which was responsible for large off-state leakage currents due to the small channel size.

The fin brought in the era of nonplanar devices[120,121]. With the current production technology node at 14 nm (based on fin width), identifying and understanding individual finFETs is a burgeoning field. Defects in finFETs are currently identified using electrical, optical, or thermal techniques such as soft defect localization using a scanning optical microscope[122,123], infrared (IR)-based techniques, due to Si being transparent to IR wavelengths[123,124] and scanning spread resistance microscopy[125,126]. Although these techniques can tell the pass or fail state of each transistor and a localized region where the FETs are good or bad, the relationship between device failure and structural or concentration anomalies is still missing. At best these techniques can provide a spatial resolution of ~50 nm[122–126].

Soft defects occurring due to dielectric breakdown, process variations, and resistive interconnects are more often attributed to structural defects at the atomic level. Specifically, line-edge roughness and fin thickness variations can affect the threshold voltage and sub threshold slope[127,128], both important electrical parameters for low power devices. Variations in the oxide layer thickness can give rise to larger tunneling currents[129], while discrete impurity atoms in the channel can significantly affect the current density in the channel[130]. Thus, a systematic study of such variability in individual devices is necessary as the device dimensions decrease so that the performance of an IC is not comprised. Both the

scanning transmission electron microscopy (STEM) and atom probe tomography (APT) can aid to further this understanding. Although the STEM can provide an atomic scale spatial resolution <1Å [131] and an energy-dispersive X-ray spectroscopy (EDS) system incorporated in the STEM can provide chemical mapping, the ability to observe low atomic number (Z) elements is still lacking. Further the STEM can only provide 2D information on 3D finFETs.

Since the introduction of laser-assisted APT, the semiconductor industry has quickly ensured early adoption of this technique. APT can provide both spatial and compositional information by combining time-of-flight mass spectrometry with a point projection microscope. Samples prepared in the form of a needle are field evaporated under the application of a high-DC voltage and a UV laser to give 3D-nanoscale composition with a spatial resolution of ~0.2 nm at best at best for metals and up to 1–2 nm for complex oxides and nitrides[132], in x, y and z dimensions[87,88,92,133].

Initial studies on semiconducting devices and structures dealt with arsenic (As) Cottrell spheres in Si[134]. Further studies on Si–germanium (Ge) epitaxial layers[90] were followed by reports on planar high-κ dielectrics analyzed using both secondary-ion mass spectrometry and APT to show the reliability of APT[86,135]. Subsequent studies on distribution of boron and phosphorus dopants during processing and on boron distribution during ion implantation were also reported[85,136]. Individual planar metal-oxide semiconductor field-effect transistor devices have also been analyzed by[84] and by[137]. Kambham et al.[97,138–140] dealt

with the issue of targeting individual fins. Very recently, correlative microscopy with APT and transmission electron microscopy (TEM) on 30 nm static random access memory (SRAM) planar transistors with Ni–Si contacts has also been shown[141]. Boron profiles for 14 nm fins were reported by[142] albeit on samples specifically prepared for APT.

Thus, intensive studies have been carried out for transistors using APT, but none of the aforementioned studies have shown the application of correlative microscopy (APT and STEM) to 14 nm commercial finFETs, with analysis of gate dielectric stack and fin region for both PMOS and NMOS; 14 nm finFETs have added complexity of their small size apart from being 3D in nature. Furthermore, previous studies have not dealt with as-fabricated commercial devices, but with devices where fabrication was halted midway to obtain and prepare samples for APT. In this report using STEM-EDS and APT, we analyze in detail finFET regions for both NMOS and PMOS fins in as-fabricated devices. PMOS devices are characterized by the presence of Ge (allows strain-induced mobility enhancement) as opposed to the NMOS. The importance of using two complementary techniques is discussed here along with their advantages and shortcomings. APT being a 3D technique, with the ability to observe all elements with equal probability, shapes the future of nanoscale characterization for finFETs.

4.2 Materials and Methods

Scanning electron microscope (SEM) images of individual fins, for both NMOS and PMOS, are shown in Figure 4.1. This aids in correct identification of

the region of interest. The schematic (Figure 4.1 (a)) depicts the Si fin and gate dielectrics. Samples prepared for APT are etched using hydrogen peroxide to remove tungsten from the contacts. The removal of the tungsten increases the analysis success rate by reducing sample fracture during field ionization. The planar view of the device at the contact level, after tungsten etching, is shown in Figure 4.1 (b). The PMOS is identified by the intermittent nature of the fin (fin ends shown) and the NMOS is the device adjacent to it (left panel of Figure 4.1 (a) and Figure 4.1 (b)). APT specimens are extracted and sharpened using standard FIB-based cross-section lift-out and annular milling procedures[143–145] but the APT lift-out differs from TEM/STEM lift-out since a wedge-shaped section is used for APT whereas the TEM/STEM uses a cuboidal block.

4.2.1 Sample Preparation for STEM

Integrated circuits containing SRAM arrays are removed from the packaging and de-bonded using standard protocols discussed in the literature. The chips are then cleaved to the required size and undergo mechanical polishing to the layer of interest; 14 nm SRAM arrays are identified for the PMOS and NMOS regions, using computer-aided design (CAD) layout, in an FEI Helios NanoLab 650 (FEI, Hillsboro, OR, USA) or 450S FIB/SEM system. The region of interest is protected from Ga damage during ion milling using metallic Pt deposited in situ in the FIB using a gas injection system (GIS). The region of interest is then marked down with “X”- type FIB milling patterns to ensure easy identification during

subsequent steps. A lift-out section is prepared by milling rectangular patterns on either side followed by a J-cut.

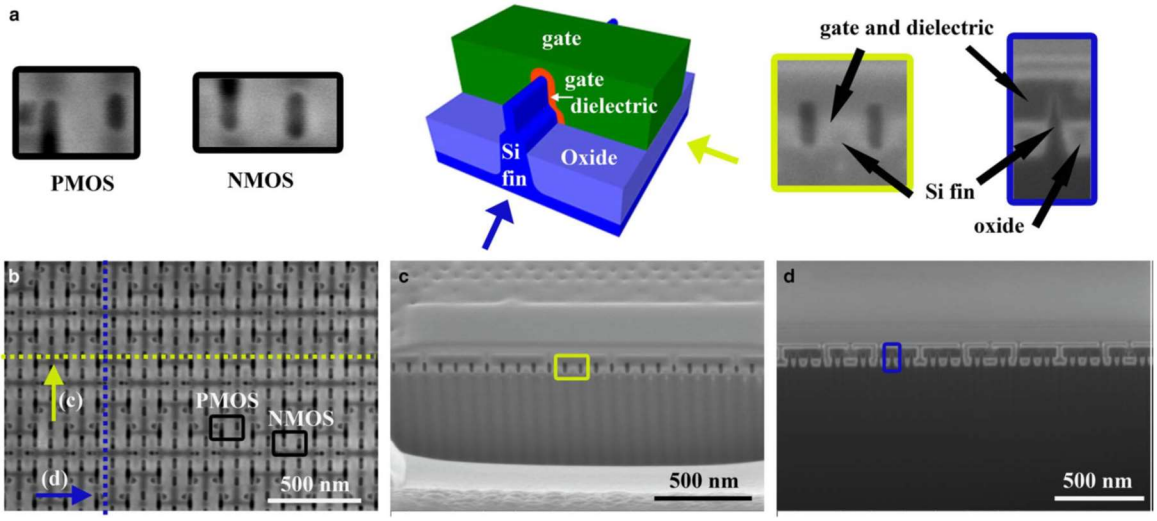

Figure 4.1 (a) Left panel: planar view of individual p-type metal-oxide semiconductor (PMOS) and n-type metal-oxide semiconductor (NMOS) devices that are analyzed using atom probe tomography and scanning transmission electron microscopy. Center panel: schematic of a typical field-effect transistors. The Si fin is shown in blue with a layer of buried oxide, above which the fin protrudes from the substrate. The gate dielectric stack which consists of multiple layers is shown in orange with the gate itself in green (schematic not drawn to scale). Right panel: an individual fin cross-section in two different directions. (b) Scanning electron microscope (SEM) image of a PMOS and a NMOS transistor with the contacts etched, in planar view. (c) Cross-section SEM image of the sample along the gate direction (as shown by the yellow dashed line in (b). (d) Cross-section SEM image of the sample along the fin direction (as shown by the blue dashed line in (b). Individual fins are visible as indicated by the blue box.

The thickness of a lift-out section is typically between 2–3 µm. A micromanipulator is then used to detach the prepared section from the substrate and attach it onto an OmniProbe® Cu grid (Ted Pella, Inc., Redding, CA, USA) suitable for use with a TEM/STEM sample holder. The attached section is then milled down to a thickness of ~150 nm at an accelerating voltage of 30 kV and a beam current of

~0.23 nA. A low accelerating voltage of 5 kV or less and a current of ~68 pA are then used for the final polishing step to remove any re-deposition due to the Ga milling and bring the final thickness within 20 nm. The cross-section parallel to the fins, as shown in Figure 4.1 (c), and perpendicular to the fins, as shown in Figure 4.1 (d), are both used to ensure accurate identification of the region of interest. Additional details and images for the sample preparation are mentioned in Appendix A, Section A.5.

4.2.2 STEM-EDS Measurements

As prepared TEM sections are analyzed using an FEI Tecnai Osiris™ system at 200 kV accelerating voltage. Four windowless silicon drift detectors placed at 90° with respect to each other are used to obtain the chemical maps. A 1 nA beam is used in a ~512 × 512 array with a 25 µs dwell time for ~10 min. The EDS data is then quantified and deconvoluted using the Cliff-Lorimer method.

4.2.3 Sample preparation for APT

Integrated circuits containing SRAM arrays are removed from the packaging and de-bonded using standard protocols. The chips are then cleaved to the required size and undergo mechanical polishing to the layer of interest. The cleaved chips are then etched to remove tungsten (W) from the contacts; 14nm SRAM arrays are identified for the PMOS and NMOS regions, using CAD drawings, in a FEI Helios NanoLab 650 or 450S FIB/SEM system. The PMOS is identified by the intermittent nature of the fin (fin ends shown) and the NMOS is the device adjacent to it (Figure 4.1 (b)). The region of interest is protected from

Ga damage during ion milling using a thin layer (~150 nm) of either metallic (Ni), deposited by sputtering, or insulating (SiO_2) layer, deposited in situ in the FIB using a GIS. This is followed by metallic Pt deposition (~100–200 nm). A wedge-shaped slice of the sample section, with the region of interest is then detached from the sample surface using a micromanipulator. The wedge-shaped slice is prepared by milling rectangular patterns at a tilt angle of 22° and ensuring that the fins are perpendicular to the milling direction. The detached section is then placed on an Axial Rotation Manipulator™ (ARM3™) module and the free-hanging edge is cleaned (milled) to view the fins. One of the walls (depending on the direction of rotation for cross-section sample preparation) is milled to bring the transistor of interest right at the edge (Appendix A, Section A.4). The lift-out wedge is then physically rotated 90°, such that the fins are facing sideways (with respect to the analysis axis) to prepare cross-section tips. The rotated wedge has the fins facing sideways. On the visible gates on top, another layer of either metallic (Ni) or insulating (SiO_2) layer is deposited (~100 nm) followed by Pt (~200 nm). The wedge (due to the rotation) now has one flat parallel wall (parallel with respect to the analysis axis). Thus, a new wedge-shaped section is now prepared out of the existing section where the bottom apex of the wedge is aligned with the top of the fin or the region of interest. The as-prepared wedge is then detached from the ARM3™ module using a micromanipulator; 2 μm long square pieces are cut from the wedge and placed on as-fabricated Si microtip arrays. These are then annularly milled (at 30 kV accelerating voltage and ~0.23 nA followed by ~26 pA

when the end diameter is <800 nm) using a donut-shaped milling pattern to obtain a conical tip with an end diameter <150 nm. A final polishing (using 2 kV accelerating voltage and ~34 pA, and subsequently ~24 pA) is used to remove any residual Pt from the tip surface, which might interfere with the APT results. Additional details and images for the sample preparation are mentioned in Appendix A, Section A.4.

4.2.4 APT measurements

As prepared tips are then quickly transferred to the LEAP system and run in the laser-assisted mode to obtain the 3D atom probe reconstruction. For the PMOS devices, prepared tips are run in a LEAP 4000 XHR (at the Environmental Molecular Sciences Laboratory at Pacific Northwest National Laboratory, Richland, WA, USA) at a base temperature of 50 K and laser energy of 60 pJ with a pulse repetition rate of 125 kHz. A detection rate of 0.005 ions/pulse is used. The NMOS devices are run in the LEAP 5000 XR (Cameca, Gennevilliers, France) at a base temperature of 50 K and laser energy of 60 pJ with the pulse repetition rate of 100 kHz. Obtained data are reconstructed using the Integrated Visualization and Analysis Software (IVAS®) software following the tip profile method.

4.3 Results

4.3.1 STEM

Nanoscale chemical composition maps representative of the elements present in the fin and the gate dielectric layer are shown in Figure 4.2, for both NMOS and PMOS, respectively. The high-angle annular dark field (HAADF) image

of the region probed in the EDS is shown at the left in Figure 4.2. The first row corresponds to a NMOS along the direction of the fin (the direction corresponding to the fins is displayed in Figure 4.1 (d)). The HAADF map for the NMOS (Figure 4.2 (a) left) demonstrates different contrasts for the Si fin and the gate dielectric layers. The large region of light grainy contrast also seen is tungsten (EDS map shown in Appendix A, Section A.6), which has been etched only for APT specimens and not for STEM. The EDS maps show that for the silicon (Si) fin and the gate dielectric layers consisting of Hf, O, Ti, N, Al, and C are clearly visible. The HfO_2 high-κ dielectric forms a thin barrier around the Si fin followed by a thin layer of TiN, then AlC_x and subsequently a thicker layer of TiN before the W gate contact. The TiN layer contrast is visible more so from the N maps as opposed to the Ti maps. The Ti map shows a blurry contrast across the Al layer. The HAADF map along the gate direction for the NMOS, displayed in Figure 4.2 (b), shows the W (light contrast) present in the contact regions (source and drain) and at the center of the gate region for the 14 nm technology node. The HfO_2 high-κ dielectric is present only in the gate region and the Al signals are also seen only in the gate region. Thus, the source-drain contacts are devoid of any HfO_2 or AlC_x layers. In the gate direction also HfO_2 is the layer closest to the fin. Structural irregularities in the Si fin, as well as the HfO_2 high-κ dielectric, are absent from the EDS maps (Figs. 4.2 (a), 4.2 (b)) indicating a working NMOS device.

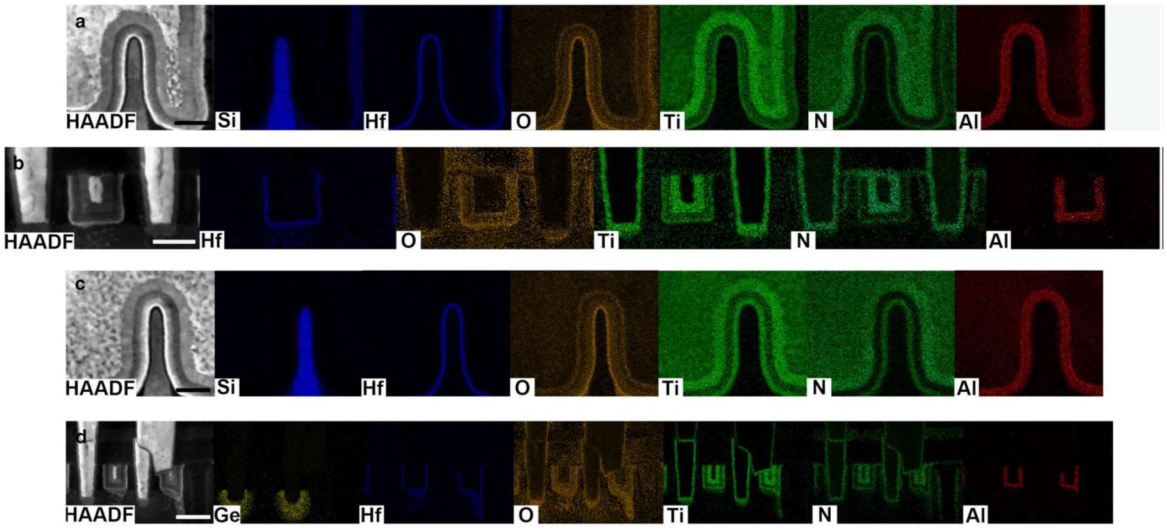

Figure 4.2: High-angle annular dark field (HAADF) image and energy-dispersive X-ray compositional maps (a) for a n-type metal-oxide semiconductor (NMOS) fin, (b) for the gate region in an NMOS fin, (c) for a p-type metal-oxide semiconductor (PMOS) fin, and (d) for the gate region in a PMOS fin. The presence of Ge and the differing fin widths distinguish a PMOS from a NMOS. The Si fin and Hf from the HfO_2 dielectric is shown in blue, O in orange, Ti and N signals from the TiN layer are in green and Al signals from AlC_x are in red. Scale bar: (a, c) 20nm, (b) 30nm, and (d) 50nm.

Figures 4.2 (c) and 4.2 (d) display EDS maps for the PMOS devices. The PMOS devices show similar chemical compositions for the gate dielectric stack as the NMOS devices. The Si fin is also visible in Figure 4.2 (c). There are two important differences between the PMOS and the NMOS device: (a) the Si fin is thicker for the NMOS device compared with the PMOS device (Figure 4.2 (a), 4.2 (c), respectively); (b) the PMOS device is characterized by the presence of Ge in close proximity to the gate region, right under the W contacts. Both these differences, especially the presence or absence of Ge can be used to identify a PMOS from a NMOS device.

Thus, with careful sample preparation and a sensitive EDS detector, a wealth of information on the physical device structure and chemical composition can be obtained from the STEM, however this technique suffers from three shortcomings; (a) with each successive generation of devices, due to reducing sizes the total signal intensity for the EDS will keep decreasing. Low Z elements such as N, O, and Al show a background signal from other regions as well (Figure 4.2). This indicates that the available scattering cross-section for reliable EDS signals from finFETs will ultimately reach its limit. (b) The ability to see dopant elements such as boron is not possible using this technique. Both the low concentration of dopants in finFETs ($10^{18}/cm^3$ corresponding to parts per thousand) as well as the low atomic number makes it difficult for EDS to yield any reliable chemical maps of boron in the STEM. (c) Any sort of 3D information is also missing since the STEM provides 2D information averaged over ~100 nm in the third dimension. Obtaining 3D information becomes more important especially for the PMOS devices where the fins are not continuous and the end points at the source/drain cannot be completely understood using 2D maps from the STEM.

4.3.2 APT

The aforementioned shortcomings of STEM motivated the use of APT, which is more suited to characterize the 3D nature of the finFET device (Figure 4.1 (a)). APT has equal probability of detecting all elements in the periodic table allowing detection of B, C, N, Al, and O for the FETs. It further allows ~10–100 parts per million (ppm) quantitative sensitivity (upto 1 ppm under conditions of low

background counts and large number of atoms collected[146]; which is two orders of magnitude higher than that obtained by EDS[133,144]. Although most techniques provide either compositional or spatial information, APT is unique in its ability to convert time-of-flight mass spectrometry to compositional information (through mass to charge ratio). The sequence of ions and x, y coordinates from a position sensitive detector are converted into 3D spatial information.

The analysis of the Si fin and gate dielectric layers obtained using APT is displayed in Figure 4.3. The absence of Ge as evidenced by the mass spectrum analysis (Appendix A, Section A.3, Figure A.3) allowed identification of these maps as part of a NMOS device. As seen from the leftmost map in Figure 4.3 (a), the Si fin (in blue) is wrapped on three sides by the gate dielectrics. The HfO_2 layer (shown in orange) and the subsequent TiN and AlC_x layer (in green and red, respectively) are also seen on all three sides of the Si fin. The inset shows the HAADF image of the NMOS fin with the black box marking the region that was analyzed in APT. This conclusion is based on the chemical compositions observed from the NMOS atom probe maps, which were captured using a LEAP 5000 XR at Cameca. The gate dielectric layers are observed in succession in the individual atom maps shown in Figure 4.3 (a) (additional maps are shown in Appendix A Section A.1). The HfO_2 high-κ dielectric layer can be analyzed using the HfO maps and the TiN layer is analyzed using the TiN maps. The Ti maps also show a blurry contrast across the AlC_x layer, similar to the STEM-EDS results. Both Al and C maps are useful for analyzing the AlC_x layer itself.

The presence of atoms of different chemical species in regions far apart from the fin cannot be construed as a background signal. As an example, the complete 3D information that could be obtained from the HfO maps is shown in Figure 4.3 (b). Each map corresponds to a rotation of 90°. The atom probe maps display regions of HfO perpendicular to the fin (the first and third maps in Figure 4.3 (b)). When rotated by 90°, these regions would appear as if they were part of a low count background signal (as seen in the HfO map in Figure 4.3 (a)). This can be explained in the following way; during device fabrication, the HfO_2 high-κ dielectric layer is deposited using atomic layer deposition[147] in the pits formed after the fins are fabricated, defining the gate area. HfO_2 covers all the pit walls of the gate area and fin walls also. The region of HfO_2 covering the fin (Figure 4.3 (a)) corresponds to that which was deposited over the fin wall while the perpendicular regions, seen in Figure 4.3 (b), correspond to part of the pit walls of the gate area. A similar analysis can be carried out for the TiN and AlC_x layers also. Supplementary Movie shows a video clip of HfO_2 layer as it completes a 360° rotation to allow a full 3D interpretation. Such detailed visualization of the gate dielectric layers, as well as the fin, has been observed for the first time.

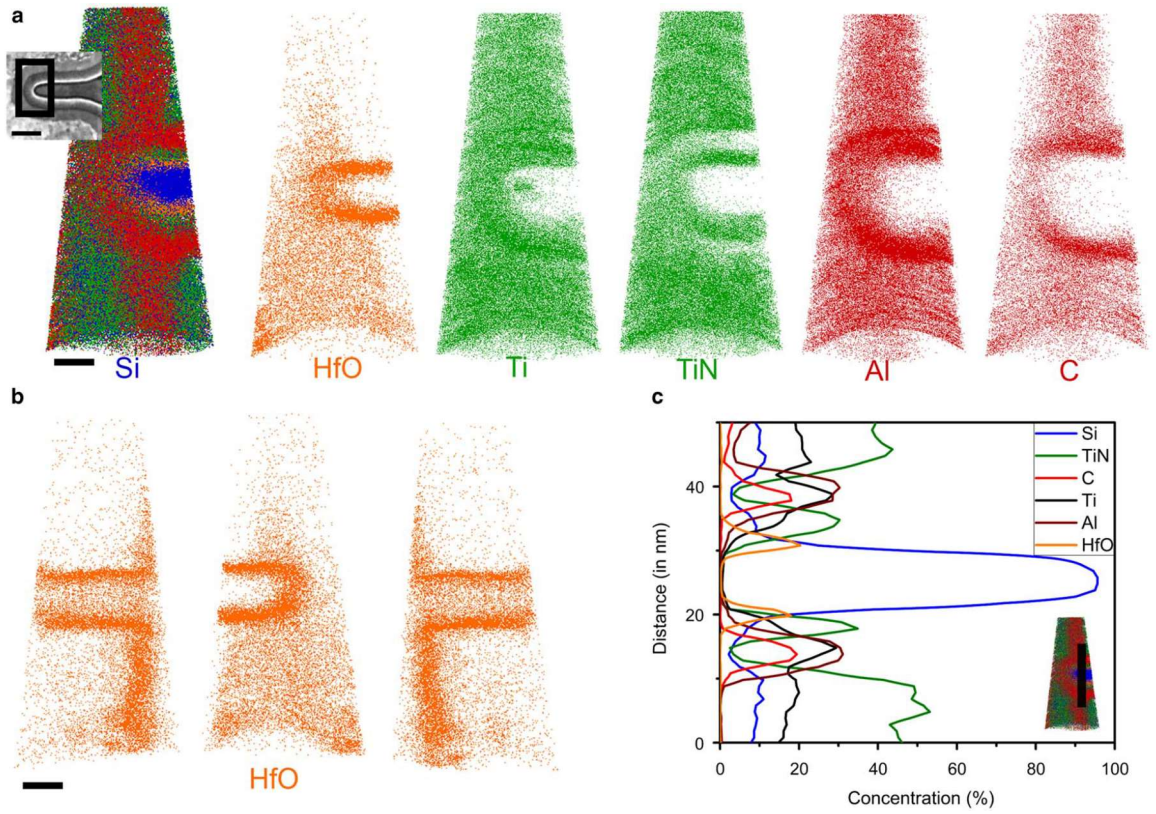

Figure 4.3 (a) Atom probe tomography (APT) maps of a n-type metal-oxide semiconductor fin with inset showing the high-angle annular dark field image for the region of interest captured in APT. The Si fin is covered by the gate dielectric on three sides. (b) APT maps for HfO each rotated by 90° with respect to the previous. (c) Concentration profile across the fin and the gate dielectric stack for each of the chemical species. Scale bar is 25 nm in length.

Further detailed analysis of the dielectric layers can be carried out by measuring their concentration profiles as a function of distance (Figure 4.3 (c)). The region plotted for the concentration profile is shown in the inset (bottom right). The concentration profile is taken across a cylindrical section by averaging the concentration across a circular area of a given radius (here 5 nm) and plotting it as a function of distance. The physical position of the cylindrical section determines the region where the plot is made, with a bin size of 0.1 nm along the distance axis.

From the concentration profile three important inferences can be made; (a) it can be observed that the Si fin (blue curve) is covered by the HfO_2 dielectric on either side (orange curve). This is followed by a thin layer of TiN (green). Subsequently AlC_x (red curves for Al and C) and a thick layer of TiN are present. This is in close agreement with the STEM-EDS maps. The Si fin is devoid of any observable contamination from any of the dielectric stack, as evidenced by the zero concentration of the dielectric layers in the fin region. The concentration of the dielectrics on either side of the fin is also similar indicating uniformity in processing conditions during fabrication. A single peak on each side also hints toward minimal variability in fin wall thickness, which directly affects the device threshold voltage. Such profiles are important in case of failed devices where any anomaly in the concentrations on either side could possibly give rise to device failure. Another observation is that the Si fin concentration also increases after the dielectric stack due to the presence of SiO_2 which is used as the insulating barrier around the fins.

The analysis for a PMOS device is more complicated due to the intermittent nature of the fins and the presence of Ge which strains the region around it. This analysis should be interpreted with caution as the presence of undulating walls or waviness could possibly indicate intermixing or a sporadic evaporation field. APT analysis of a PMOS device is shown in Figure 4.4. Parts of a Si fin and the gate dielectric layer, albeit on two sides, can be observed in the first map in Figure 4.4a. This region is toward the right side of the first map. Apart from this, the map also shows a region of Si toward the left of the map and dielectric regions perpendicular

to the fin but with undulating walls unlike the NMOS maps. Such undulating walls are generally observed for contacts (due to less stringent design considerations) or regions near the contacts (Figure 4.2 (d)). A clear understanding of these undulations with specific emphasis on the effect of the evaporation field will be the subject of future work. The inset shows the HAADF image of the PMOS fin with the black box marking the region that was analyzed in APT. The PMOS device atom probe maps were captured using the LEAP 4000 XHR at Pacific Northwest National Laboratory. As seen from Figure 4.4 (a) the PMOS also shows a similar layered structure as present in the NMOS for the gate dielectric stack (additional maps to aid in the interpretation are shown in Appendix A Section A.2). Figure 4.4 (b) shows the Ge maps, which is a signature for PMOS. Ge is present at the base of the fin region in this map (mass spectrum used for the analysis is shown in Appendix A Section A.3, Figure A.4).

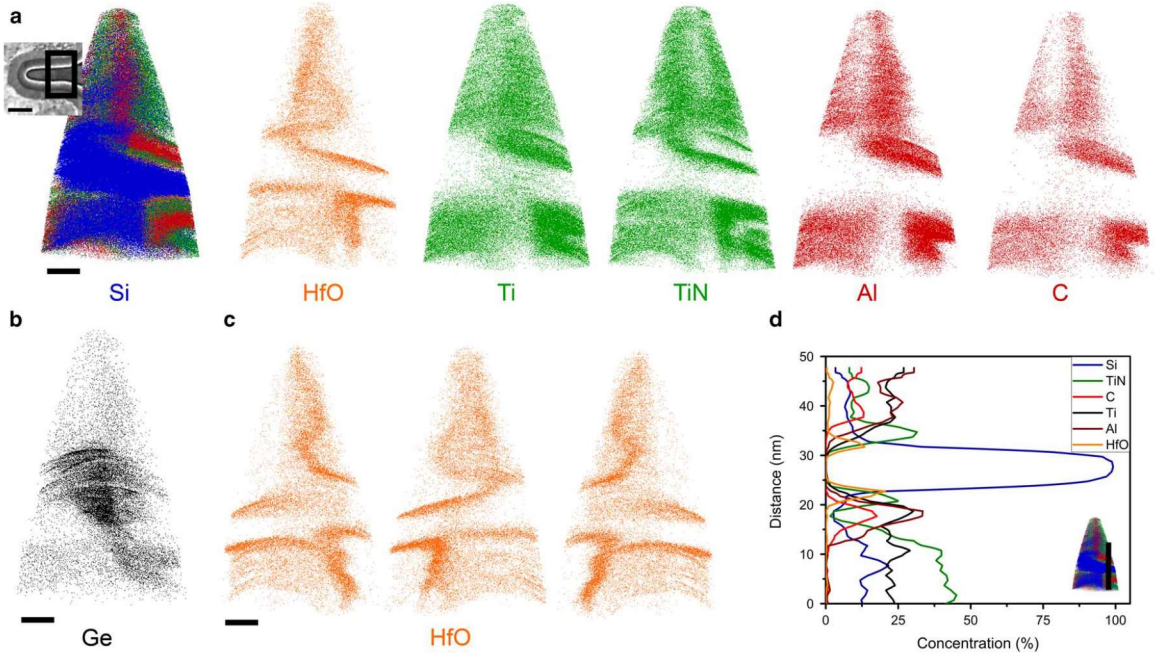

Figure 4.4 (a, b) Atom probe tomography (APT) maps for a p-type metal-oxide semiconductor (PMOS) fin closer to the source/drain contact. Inset: high-angle annular dark field image for the region of interest captured in APT. (c) APT maps for HfO each rotated by 90° with respect to the previous. (d) Concentration profile across the fin and the gate dielectric stack for each of the chemical species. Scale bar is 30 nm in length.

The HfO maps show a twofold V-shaped region at the base of the atom probe map (first map in Figure 4.4 (c)). The left part of this map shows well-defined regions around the fin whereas the right-side shows the perpendicular undulating regions. The same regions can be observed in different views across the other maps in Figure 4.4 (c), each rotated by 90° with respect to the previous one. This V-shaped region at the base also contains O and a small amount of B (Appendix A Section A.2). Thus, for the PMOS, the 3D visualization along with chemical composition was essential for identifying the region closer to the source/drain contact. The concentration profile shown in Figure 4.4 (d) follows the same trends

as that for a NMOS (Figure 4.3 (c)) but provides further information for the PMOS. The slightly different concentrations of the dielectrics on either side of the fin indicate that, closer to the contacts, the control on the layer thickness is less than around the fin-gate intersection, which was seen in the NMOS maps in Figure 4.3.

4.4 Discussion

APT is able to provide detailed spatial (~1 nm for semiconducting heterojunctions) and compositional information (with approximate ppm detection range) for the finFETs which is not possible with STEM. In order to gain confidence in the APT maps, it can be seen that there are similarities between the observed maps. First, the Ti signals in the AlC_x layer is mimicked by both techniques for PMOS and NMOS. Second, the N signal in the STEM maps and the TiN signals from the atom probe maps are useful for understanding the TiN dielectric layer, showing similar features. Third, Al and C signals are consistent across both techniques. Finally, similar distribution for the HfO_2 layer is also observed using both techniques.

A comparison for the thickness of the Si fin and gate dielectric stack, for PMOS and NMOS, by STEM and APT is provided in Table 4.1. The STEM thickness measurement is obtained from the maps itself while APT values are obtained as full width half maximum of the concentrations as a first approximation. The values indicate a tighter spread in the thickness using STEM as opposed to APT.

Table 4.1: Thickness Comparison for the Si Fin and Dielectric Stack for n-Type Metal-Oxide Semiconductor (NMOS) and p-Type Metal-Oxide Semiconductor (PMOS) Using Scanning Transmission Electron Microscopy–Energy-Dispersive X-Ray (STEM-EDS) and Atom Probe Tomography (APT).

	Si Fin	HfO_2	TiN	Al	C
STEM-EDS					
PMOS	–	1.31	3.15	4.58	
NMOS	–	1.25	1.66	3.88	
APT					
PMOS	8.1	1.75	2	4.9	4.2
NMOS	9	2.2	2.35	6.4	3.8

All units are in nm.

Although the APT can provide true 3D maps of various ionic species, some important shortcomings of this technique are worth mentioning here, specifically with regard to how the contrast (thickness) of different layers can be affected by the instrument itself. The APT uses a mass to charge ratio for identification of chemical species which leads to the issue of overlaps for similar mass to charge ratios for different chemical species (e.g., Ti^{3+} and O^{2+}). Thus, care needs to be taken to ensure that the influence of these overlaps on the interpretation is ruled out. The presence of isotopic abundance and physical regions in the maps are often used to rule out most overlap issues. The field evaporation of ions can also cause significant trajectory aberrations for dissimilar elements, which is severe for regular top-down sample preparation in APT[146,148–151]. Further, since the field evaporation process is not uniform due to changes in local electrostatic environment during the evaporation process, the results should be interpreted with

caution as the reconstruction algorithms are based on simple hemispherical models[152]. Therefore, trajectory aberrations due to field evaporation of dissimilar species and spectral overlaps are most likely causing the differences in thickness between STEM-EDS and APT. This brings into focus the role of correlative microscopy used here, whereby two complementary techniques can provide unique information as well as allow greater reliability by supporting the claims based on the other technique.

Such studies, as the one carried out in this paper, are imperative since with each technology node, device to device variability during fabrication can be expected to go up due to the small device size. The tolerance in fin width has been calculated to about 1 nm for industry acceptable variability in electrical parameters for 20 nm finFETs and a tolerance of 10–15% for variations in gate length[153]. Further, diffusion of dopants into the Si channel can cause large changes in the electronic density, known as random density fluctuations; these are an important part of current experimental and computational studies[127–130]. A failed device could hence differ from a working device based on small structural or concentration fluctuations. Thorough analyses call for techniques such as APT and STEM, which can observe the structural and compositional variability and correlate it to the device performance.

4.5 Summary

In conclusion, the chemical and spatial distribution of finFETs were studied using correlative microscopy by employing APT and STEM. Although STEM is able

to provide 2D chemical maps on the fins and dielectrics, its inability to probe low Z dopant atoms or present any 3D maps motivated the use of APT to further our understanding of PMOS and NMOS devices. The APT maps showed the 3D views of the dielectric layers with similarities between both techniques. The TiN signals provide additional information for the finFETs apart from N in the STEM. The thickness measurements show the efficacy of each of these techniques. Although STEM-EDS will ultimately reach its limits due to device scaling and low signal sensitivity in the EDS, the APT with ppm sensitivity and nanoscale spatial resolution will be poised to continue investigations on each new generation of finFETs and other non-Si technologies. In addition, continuous semiconductor process scaling down to 10 and 7 nm aligns well with the APT sample volume, allowing for increased portions of the finFET structure to be analyzed as the transistor geometry scales down. Correlative microscopy will also be important to enhance the reliability in APT results while simultaneously being used for advanced characterization of finFETs. The introduction of 3D integrated circuits and flash memory, such as the VNAND flash technology by Samsung® (Seoul, South Korea), make APT particularly suitable for future applications that require 3D chemical maps.

4.6 Acknowledgements

Chapter 4, in full, is a reprint of the material Parikh, P., Senowitz, C., Lyons, D., Martin, I., Prosa, T. J., DiBattista, M., Devaraj, A. & Meng, Y. S. Three-Dimensional Nanoscale Mapping of State-of-the-Art Field-Effect Transistors

(FinFETs). *Microscopy and Microanalysis* **23,** 916–925 (2017). The dissertation author was the primary investigator and author of this paper. APT measurements and sample preparation were performed by the author. Isabelle helped with the APT measurements for NMOS. Corey and Don worked on the STEM-EDS sample preparation and results. Corey and Don also helped with the interpretation of the APT data.

Chapter 5 : Compositional quantification of high nickel content NCA and NMC battery oxides using Atom Probe Tomography

5.1 Introduction

The shift from gasoline powered to electric vehicles has seen a steady rise over the past few years. With a projected increase in sales of twice as many electric vehicles[154], the development of battery packs that can provide over 300 miles of driving range on a single charge is needed. To achieve this target both automakers and DOE have set aggressive goals for high gravimetric energy density (Wh/kg) for cell chemistry in Li-ion batteries. Increasing the specific capacity (mAh/g) of cathodes, is one such strategy that can reach this goal.

The specific capacity is dependent on the materials composition, with higher Ni content giving higher capacity, at a reasonable cost, as compared to Co. Hence the development of NMC ($LiNi_xCo_yMn_zO_2$) and NCA ($LiNi_xCo_yAl_zO_2$) cathodes where, $x \geq 0.8$ and $z \leq 0.1$ for Mn and ≤ 0.05 for Al have taken the forefront in industrial applications. Unlike $LiNiO_2$ (LNO) where the low thermal stability, high Li-Ni intermixing (which disrupts Li transport channels) and the relative difficulty to form phase pure LNO (due to similar ionic radii for Li and Ni) have prevented its early adoption, Co provides greater structural stability and rate capability, Mn provides cost benefit and covers safety aspects while Al (acting as an electrochemical inactive species), provides greater gravimetric energy density due to its low molecular weight. The presence of Mn/Co or Al/Co also make the pure phase

synthesis straightforward. This has led to both NCA (with x=0.8) and NMC (with $\leq 0.3 < x \leq 0.6$) electrodes being commercialized[3,5,53].

However, NCA and NMC (specifically NMC811- $LiNi_{0.8}Co_{0.1}Mn_{0.1}O_2$) still suffer from a host of different issues [a] gas evolution and increase in internal pressure due to continuous side reactions with the SEI, [b] formation of electrochemically inactive surface disordered phase, that inhibit Li transport and [c] formation of micro-cracks[53,155]. While a clear understanding of some of these issues exist by studying Ni and Co, the role of Al in the structural stability is still missing. Hwang et al. observed surface changes in $LiNi_{0.8}Co_{0.15}Al_{0.5}O_2$ using high resolution transmission electron microscopy (HRTEM) and electron energy loss spectroscopy (EELS)[59]. Their results showed the transition from a layered structure in the bulk to the formation of a spinel phase on the surface, and ultimately a rocksalt phase by probing the O K-edge. Sallis et al. also confirmed that the surface rocksalt phase is NiO based on selective area electron diffraction (SAED) patterns and X-ray absorption (XAS) studies[156]. To add to this understanding, Zhang et al. proposed a mechanism for the transformation from layered to spinel structure, using TEM diffraction patterns at different state of charge (voltage)[157].

To this end, the ability to observe Al distributions have been more elusive due to its low stoichiometric content (1.25% in conventional NCA cathodes). Various analysis techniques such as TEM and secondary ion mass spectrometry (SIMS) donot provide the required spatial and chemical resolution to analyze light

(low atomic number) elements. Moreover strategies to mitigate the above observed issues in advanced cathodes (for obtaining higher specific capacities and improved rate capability) include nanoscale coatings (both through wet chemistry[60] and atomic layer deposition (ALD)[158]), graded compositions from the surface to bulk[61] (to form a Al or Co rich surface for better stability and Ni rich center for high energy density), core shells structures with a Ni rich core and a Ni deficient shell[159] and doping/substitution at concentrations below 1%[160]. These complex cathode compositions would also become increasing more difficult to analyze with conventional 2D based analysis techniques.

Hence the need for a technique that can provide a nanoscale spatial analysis of different elements in a battery cathode in three dimensions (3D) with ppm concentration sensitivity, is now warranted. 3D information can provide answers into the compositional changes (if any) during cycling and the nature of compositional heterogeneity/homogeneity in pristine electrode materials. Such compositional analysis can directly affect electronic properties at the bulk scale and give a better understanding of battery performance.

Atom probe tomography (APT) is one such technique that can provide both the required spatial and chemical resolution needed to analyze battery cathodes currently and continue to do so for complex chemistries being developed. However, for battery cathodes, any technique used should also be able to provide accurate estimate of the stoichiometry. This is important since repeated cycling can lead to small changes in the oxidation state and stoichiometry, which are

indications of material stress, degradation and ultimately material failure. With APT being a new technique, and the possibility of tuning various parameters (such as detection rate, pulse rate, base temperature and laser energy), the close interaction between battery cathodes and APT parameters is a necessary study. But more importantly, Devaraj et al.[114] also demonstrated that an oxide stoichiometry can be severely affected by changing the laser energy with oxygen content diminishing at higher laser energies and preferential evaporation of Mg in a pure MgO system.

To this end, studies on battery cathodes using APT have been limited. Both Diercks et al.[107] and Schmitz et al.[161] have carried out correlative study of lithium cobalt oxide using TEM and APT to observe changes in the composition as function of cycling but with different net compositions on the pristine films. Following this, Devaraj et al. also investigated $Li_{1.2}Ni_{0.2}Mn_{0.6}O_2$, a lithium excess cathode[110], as a function of cycling with close to accurate composition for the transition metals. Maier et al.[108], and Pfeiffer et al.[162] have also investigated $LiMn_2O_4$ with atomic compositions varying widely from the ideal stoichiometry. A correlative study by Mohanty et al.[111] on $Li_{1.2}Mn_{0.55}Ni_{0.15}Co_{0.1}O_2$ to study the degradation mechanism also was able to get good compositional accuracy for Ni and Mn but not for Co. Very recently, Vissers et al.[109] also studied the composition of a 5V spinel to show differences in the surface to bulk chemical composition using APT. A table comparing the atomic composition (as a percentage of the stoichiometric values) is shown in Appendix B Table B.1.

While all these studies have been carried out for mechanistic understanding of batteries, the deviation in the stoichiometry from expected ideal values, make the results qualitative at best. For a quantitative understanding, a systematic parametric investigation of the effect of laser energy on the battery cathode composition is needed. Through our work, we have elucidated this relation between the laser energy and cathode composition using pristine NCA-$LiNi_{0.8}Co_{0.15}Al_{0.05}O_2$ as our model system and comparing it with NMC-$LiNi_{0.8}Co_{0.1}Mn_{0.1}O_2$. Our studies show that there is a stark difference in the composition accuracy with laser energy, in the presence or absence of Al (NCA versus NMC). Our initial studies on NCA have helped to [a] understand how the light-matter (laser energy with cathode oxide) interactions differ in systems with elements that have different evaporation fields , [b] why other studies in literature at different laser energies could obtain close to accurate compositions just for the transition metals and [c] suitable conditions for more accurate analysis of current and future battery cathodes. Through our work we have helped to push the barriers of APT from a qualitative analysis technique towards a quantitative one, which can greatly benefit the battery community at large.

5.2 Methods

Specimen tip preparation using Dualbeam: In order to prepare APT specimen tips, pristine NCA (obtained from Toda and stored in an Ar filled glovebox) with secondary particles having a size of ~5-10 μm are dispersed onto a small (~ 5mm by 5mm) piece of Si wafer with a native oxide layer, using a spatula

in ambient. The as dispersed particles are then lightly crushed using a clean glass slide to break the secondary particles into individual primary particles. The individual secondary particles are shown in Figure 5.1 (a) and the primary particles in Figure 5.1 (c). This process is carried out since specifically for NCA, conventional liftout procedures, on secondary particles (tested early on) did not survive the APT acquisition process under high base voltage. This was possibly due to the poor physical contact between the primary particles, that led to spurious evaporation events in the voltage profile. Such events were not observed once primary particles were used for the analysis.

The prepared samples were then immediately loaded into the main chamber of a Helios FIB at the Environmental Molecular Sciences Laboratory at Pacific Northwest National Laboratory (PNNL), Richland, WA, USA or into the Scios at the San Diego Nanotechnology Infrastructure (SDNI) of UC, San Diego. A micromanipulator was used to individually pick the primary particles, that are sized between 300-500 nm through electrostatic forces between the micromanipulator and the particle. The particles are also placed on Si microtip arrays similarly due to the electrostatic forces (Figure 5.1 (d, e)). After the pick and place, each particle was coated with an e-beam Pt layer ~200 nm thick followed by an ion beam Pt layer between 500-700 nm. The diameter of the circular pattern used for the Pt deposition is larger than the particle dimensions to ensure that the particle is encased in Pt. NCA is particularly difficult to mill under ion beam hence

a total thicker Pt layer is used. The particle with the deposited Pt layer is shown in Figure 5.1 (f).

Following this, critically the annular milling step is carried out at an accelerating voltage of 30kV and ~0.23 nA beam current, until an apex diameter of 800 nm at the sample is reached, following which ~46 pA beam is current is used until the diameter is ≤200 nm. The annular milling and final tip sharpening was always carried out at PNNL. This step is tricky for such a particle pick and place since the center of the particle is lost during the Pt deposition step. Hence using previously saved SEM images, of the particles on the microtip array before any Pt deposition and secondary electron image contrast between NCA and Pt (as seen in Figure 5.1 (i)) is used to target the specimen tip such that the sample (NCA) is within the final tip shape and not deposited Pt.

During the annular milling process also, any holes or gaps in the particles are filled with Pt to allow better tip survivability. This is carried out both on the front and back side of the particle, hence the tips are rotated 180° during the annular milling process, at least 2-3 times before the final tip sharpening at 2 kV accelerating voltage and a beam current of ~35-47 pA. The annular milling process and the final tip sharpening are seen in Figure 5.1 (g-j).

The specimen tip preparation for NMC811 (obtained from EcoPro®) carried out under the same conditions as NCA, with the observation that the milling characteristics of NMC are faster than NCA. A conventional liftout was used here due to the much smaller size of the primary particles making analysis difficult and

higher tip survivability as opposed to NCA. (SEM images for NMC811are shown in Appendix B Figure B.1).

APT acquisition and analysis: The prepared specimen tips were loaded into the LEAP 4000 XHR at the Environmental Molecular Sciences Laboratory at Pacific Northwest National Laboratory, Richland, WA, USA. The data acquisition was carried out at a base temperature of 40 K and laser energy between 0.5-20 pJ (and 1-40 pJ for NMC811) with a pulse repetition rate of 125 kHz. A detection rate of 0.005 ions/pulse is used. The obtained data was reconstructed using the IVAS software with a tip image-based reconstruction. Details of the number of ions collected per run and the output of the corrections are all shown in Appendix B Table B.2.

Electrode processing and coin cell fabrication: For the initial specific capacity testing, the NCA cathodes were prepared using a manual mixing process in a mortar and pestle, where 0.25 g of cathode, and 0.0625 g of carbon black and PVDF binder, each are used. The mixing is carried out for ~40 minutes till the powders form a uniform homogenous color, with care to ensure that excessive force is not used during the mixing process. Following this, the prepared mixture is transferred to an Ar filled glovebox where N-Methyl-2-pyrrolidone (NMP) solvent is added to the mixture followed by a second mixing step for ~ 5min before the slurry is brought into ambient. The slurry is cast on a 9 μm thick Al foil and dried to obtain the electrodes. The prepared electrodes are assembled in an Ar filled glovebox in a 2016 cell configuration versus Li metal.

Galvanostatic testing: Electrochemical testing is carried out for NCA at a C rate of C/3 for both charge and discharge upto 4.8 V. The first cycle voltage profile is shown in Figure 5.1 (b), with a discharge capacity of 199.2 mAh/g as expected.

5.3 Results and Discussion

Before any APT analysis, specimen tip preparation is carried out using the Dualbeam/FIB instruments. The processing conditions for each material is usually different, hence an initial optimization was carried out for the suitable imaging, Pt deposition and annular milling conditions for NCA. Based on the optimized conditions for accelerating voltage and beam current, the specimen tips to be analyzed at different laser energies were prepared. More details about the challenges involved during the sample preparation and the conditions used are provided in the Methods Section. The general workflow used for specimen tip preparation is shown in Figure 5.1 (c-j). At the same time, to ensure that the NCA particles, were of good quality, the electrochemical performance of NCA was carried out using previously optimized slurry preparation and coin cell fabrication protocols. The electrochemical cycling results show the presence of a single-phase solid solution reaction as expected with a discharge capacity of 199.2 mAh/g, which shows that the cathode particles have not degraded prior to APT tip preparation and analysis. Additional cycling data is shown in Appendix B Figure B.2).

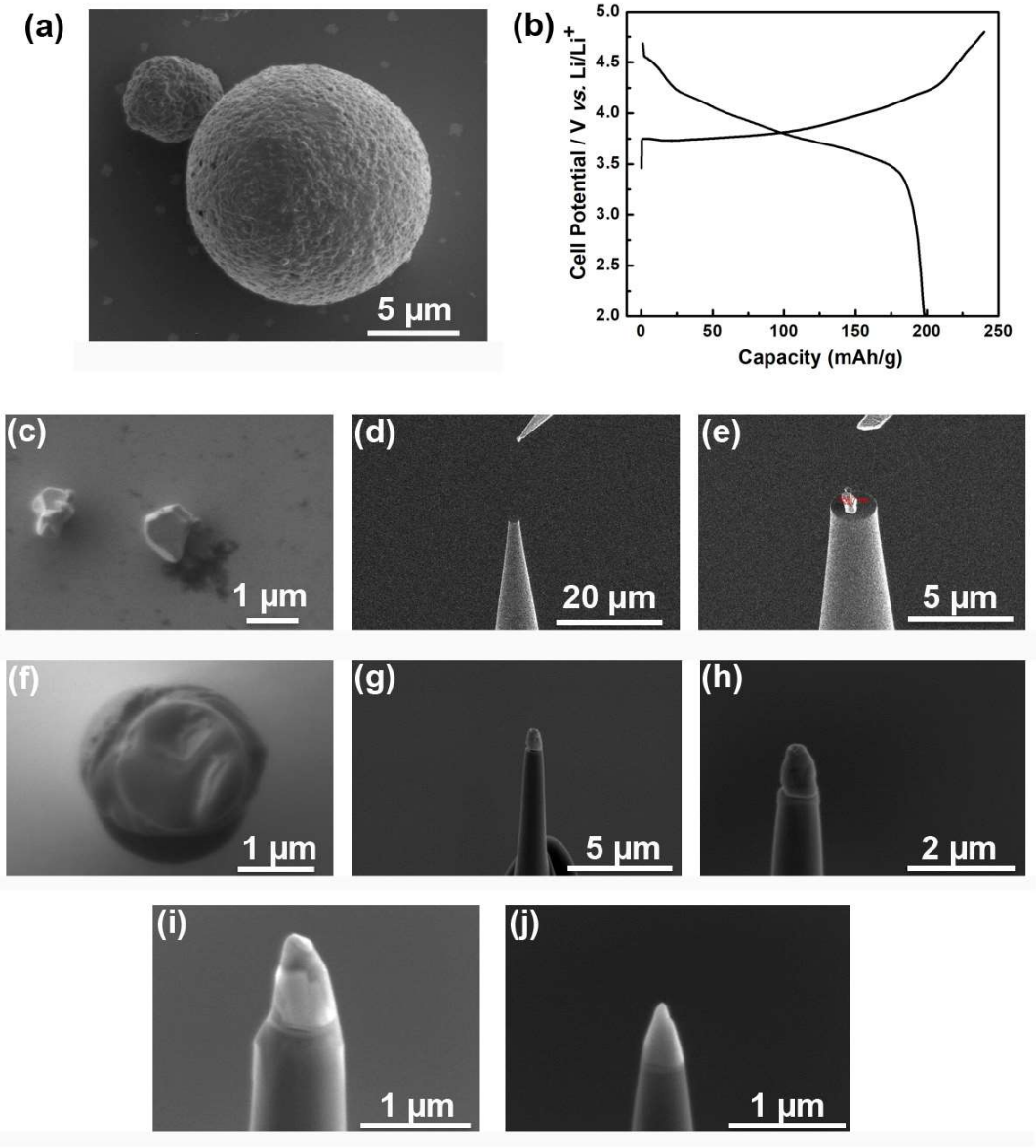

Figure 5.1: SEM images showing the pristine NCA secondary particle (a), the first cycle voltage profile (b) and the steps involved in the APT specimen tip preparation right from the primary particles dispersed on a silicon wafer (c) to the final tip sharpening (j).

Based on the success with the tip preparation and confirming the basic electrochemistry, the parametric investigation at different laser energies was carried out. Figure 5.2 (a, b) shows the atom probe maps for each of the elements

for NCA acquired at a laser energy of 1 pJ. The maps show a homogenous distribution in the pristine state indicating no spurious evaporation. Moreover, the mass spectrum is characteristic in its features for different elements (Figure 5.2 (c)). Understanding of these features is important for comparison with NMC811, which is carried out later on. With correct specimen tip preparation, Li (6 and 7 Da) is seen from the onset of evaporation and no Pt (100-110 Da) or carbon (6 and 12 Da corresponding to C^{2+} and C^{+}) is seen in the mas spectrum analysis. Moreover, the evaporation of Li is exclusively seen as elemental Li, while with Al, Ni and Co the evaporation occurs more so as oxide species.

For Al, which exists as Al^{3+}, elemental evaporation of 1+, 2+ and 3+ charging states are all seen. While for Ni and Co, which also exist as Ni^{3+} and Co^{3+}, only the 2+ and 1+ oxidation states are seen both for elemental Ni and Co and NiO and CoO oxide species. Very rarely, are NiO_2 or CoO_2 are also seen. Ga occurring from the annular milling process is also seen (as Ga^{+} and Ga^{2+}), but at atomic concentrations below 5% and usually restricted to the surface.

Based on the mass spectrum analysis obtained from the first sample, the next set of samples were analyzed according to ensure the presence of abovementioned species in each case so that each acquired dataset could be correctly identified as NCA. The presence of Li was always taken as a signature of battery cathode. Following the mass spectrum analysis, the atomic composition of each of the elements was obtained from the IVAS software by decomposing each peak into its original elements and accounting for background correction.

Laser energies of 0.5, 1, 2, 3, 4, 5, 10 and 20 pJ with 3 specimens tips at 0.5 pJ, 2 at 1pJ and 1 tip each from 2-20 pJ were analyzed for NCA samples (For NMC811, 1, 5, 10, 20 and 40 pJ were used was the testing conditions based on the analysis for the NCA particles). The atomic composition for each element is calculated as a ratio of its share in the total stoichiometry (Li atomic % is 25% since there is 1 Li in a total of (1+0.8+0.015+0.05+2) 4 atoms in the compound) and compared with that obtained directly from APT analysis, as shown in Figure 5.2 (d, e). Separate plots are generated for Al and Co since their low atomic % prevents easy viewing of the changes in the stoichiometry when clubbed into one plot.

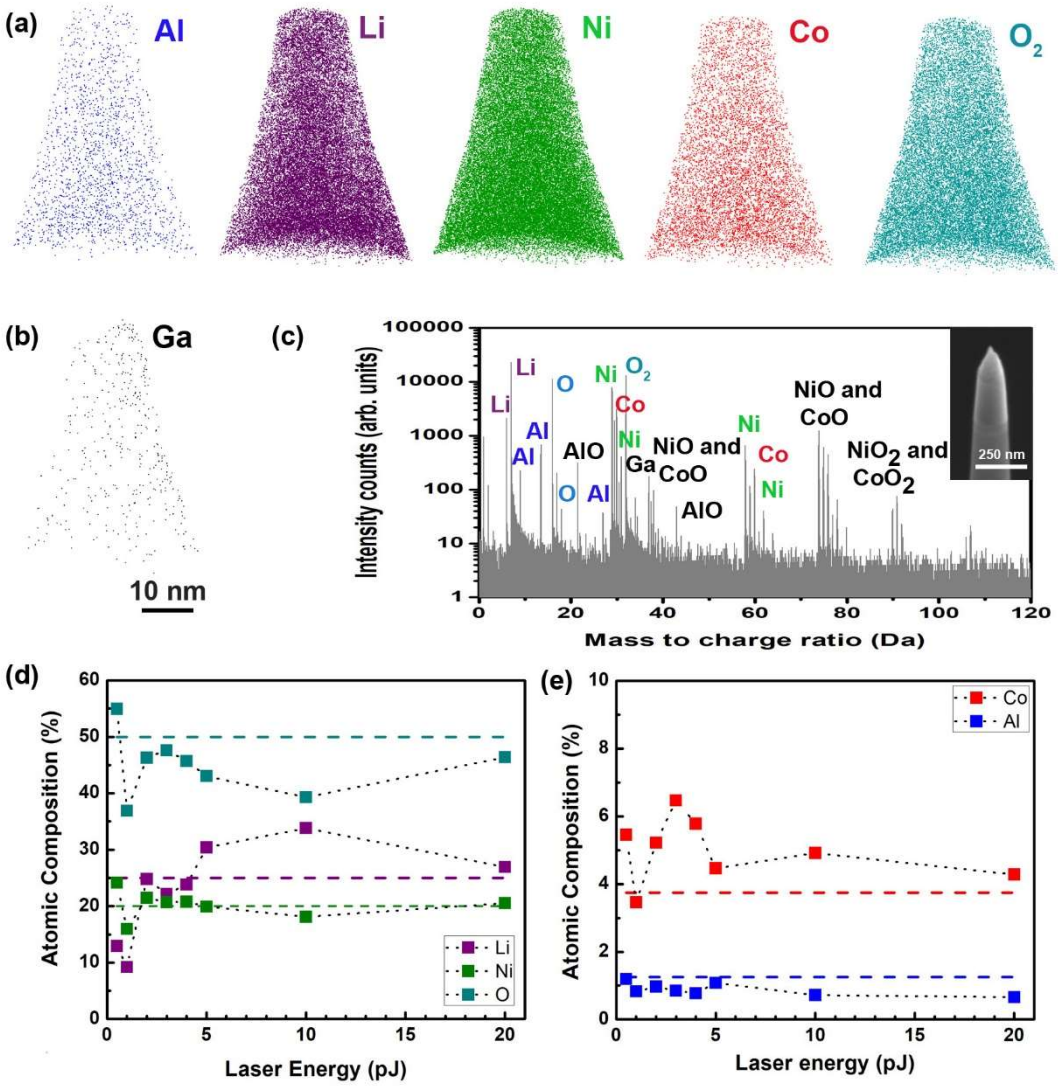

Figure 5.2: Representative atom probe maps (a, b) and mass spectrum analysis (c) for pristine NCA cathode at a laser energy of 1 pJ. (d) and (e) show the parametric investigation of the atomic composition (indicative of the stoichiometry) as a function of laser energy in APT.

The analysis shows interesting trends. First, there is a cross over from being over the ideal composition to under the ideal composition as the laser energy is increased for Li, Ni and O. The crossover here for NCA occurs between 0.5 – 5 pJ but at different laser energies for Li (~5 pJ) versus Ni and O (~1 pJ). This trend is

also seen for NMC811 for the same elements (Li, Ni and O) at the same laser energies, indicative of a phenomena that is unique to battery cathodes. Since cross over occurred within 0.5-5 pJ, this energy range was more closely investigated. Second, the composition for Li, O and Co are as close to ideal as possible when the laser energy is either 2 or 4 pJ and a wide range (2-5 pJ) where Ni composition is ideal. The composition for these elements also reaches back to ideal at 20 pJ. This agrees with reports seen in literature which are usually acquired at 0.5, 1 or 20 pJ where the transition metal compositions are close to accurate specifically for Ni, Co and Mn (NMC based compounds which have been analyzed). Our NMC811 results (shown later in Figure 5.3 (c, d)), also show this same trend, thus providing greater reliability to our results. However, lastly for Al this trend is different, with the composition steadily decreasing with increasing laser energy and 0.5 and 5 pJ giving ideal composition and the range in between deviating by 1-2% from the ideal.

While the compositional analysis at different laser energies for all the elements provides a complete picture, within the battery community and separately the atom probe community, Ni/Co ratios and quantification without oxygen, respectively, are seen as more useful analysis parameters. Ni/Co ratios are indicative of changes in the layered structure and deviations from ideal could mean the formation of surface species. Since oxide quantification at different laser energies is known to decrease with increasing laser energy, occurring from the movement of negatively charged O^- species towards the base of the tip, the

proposed method is to remove O from the quantification and see if the other elements are close to ideal observed. In this respect, Figure 5.4 (a,b), shows the compositional quantification without oxygen and (c) shows the Ni/Co ratio for the samples analyzed. The trends in the absence of O though are similar to the ones seen in Figure 5.2 (d, e) but amplified in the ability to see the deviation from ideal. The better Al quantification at low laser energy is clearly seen in Figure 5.4 (a).

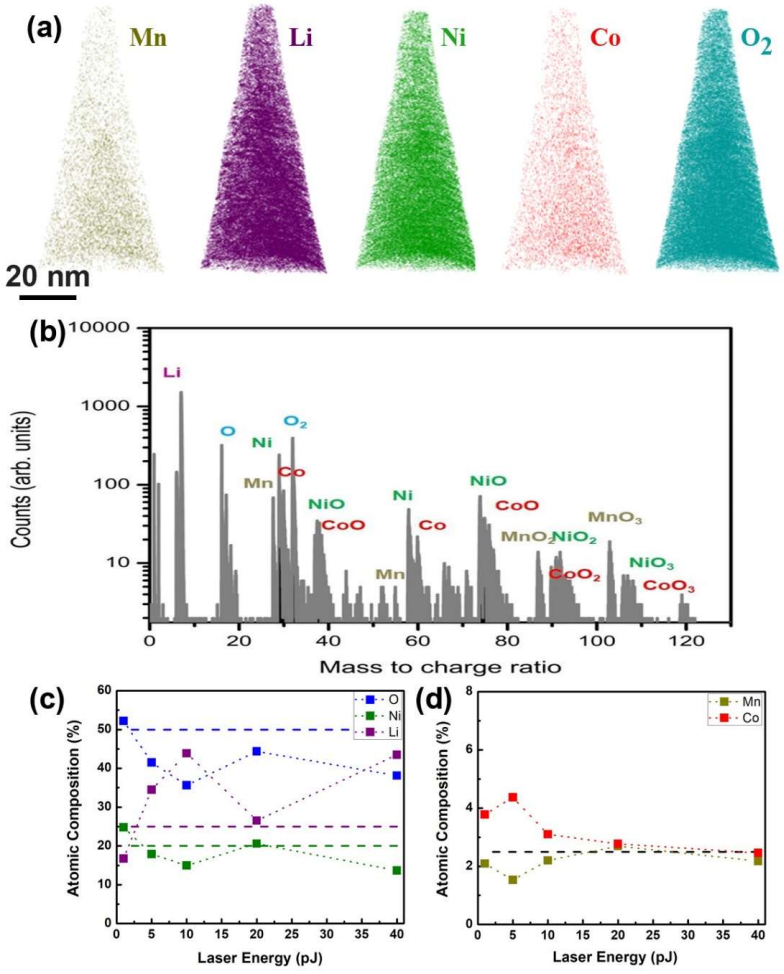

Figure 5.3: Comparison of the APT maps (a), mass spectrum (b) and compositional accuracy at different laser energies (c, d) of NMC811 with NCA (shown in Figure 5.2).

As with the Ni/Co ratio, the ratios obtained deviate by ~20% from ideal values (Figure 5.4 c)), primarily from the large variations in the Co composition seen in Figure 5.2 (e). The result shown here are individually for each tip analyzed. Moreover, the effect of different detection rates is briefly investigated, with 2 different specimen tips, one with a 0.3 % (0.003 ions per pulse) run at 20 pJ and the other with 0.4% (0.004 ions per pulse) run at 5 pJ. Both these showed a Ni/Co ratio much lower than the tip analyzed at 0.5% (0.005 ions per pulse), indicating that the detection rate used for this work is ideal for NCA analysis. However, very high detection rates (~1%) was seen to lead to uneven and sporadic evaporation and increased chances of fracture rates during APT data acquisition.

Following the analysis for NCA and observing the different compositional quantification due to the laser energy, a comparison with NMC811 was carried out next. Based on previous literature reports on transition metal-based battery oxides, the laser energies investigated were 0.5, 5, 10, 20 and 40 pJ. The initial APT maps obtained for NMC811 also showed a uniform composition (Figure 5.3 (a)) and characteristic features in the mass spectrum analysis, as seen in Figure 5.3 (b). While most of the spectral features remain the same, indicating that the evaporation proceeds in a similar fashion across different compounds, of mention is the presence of higher oxidation states oxide of Mn, Ni and Co in presence of Mn as opposed to Al in the system. Moreover, the trend observed here for the laser energy (lesser points were investigated here to get an ideal of the general trend), is different from that seen for with NCA. At 40 pJ, the composition for Ni and Li

both start to deviate from ideal and Mn and Co tending towards the same, indicating that higher laser energies would be detrimental for obtaining the expected ideal composition. However, with the exception of O (which is off by 5%), at 20 pJ, the composition obtained is close to ideal.

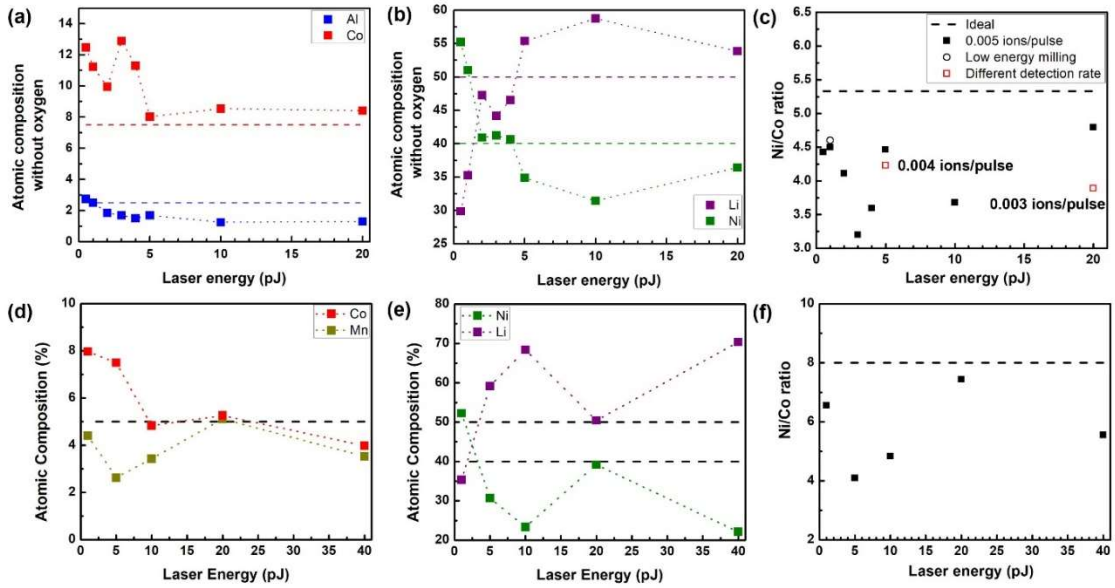

Figure 5.4: Compositional quantification for NCA (without oxygen) seen in (a) for Al and Co and (b) for Li and Ni. Comparison of the Ni/Co ratio and effect of detection rate on the ratio at different laser for each sample is shown in (c). (d), (e) and (f) show the same comparison for NMC811.

Further an analysis of Ni/Co ratio here for different laser energies also converges close to the ideal value for 20 pJ (Figure 5.4 (f)). Based on our results, the evaporation behavior is highly dependent on the interaction of the laser energy with the complex mix of elements having varying evaporation field. Li has a low evaporation field leading to an underestimation of the composition at very low laser energies (<5 pJ) but also an overestimate over 20 pJ where preferential evaporation is highly likely to happen. This is seen both for NCA and NMC, and

agrees with the understanding of how Li as a metallic species would evaporate, which is what occurs here due to elemental Li evaporation seen in the mass spectrum (Figure 5.2 (b) and Figure 5.3 (b)). For all the other elements, the trends are counterintuitive, since the evaporation energies of the oxide species need to be considered too, which is tricky to estimate in itself. It seems that the evaporation of these species is governed by the individual field energy of elemental species and the oxide species, giving rise to a more complex behavior. With Ni and Co having higher evaporation fields (35-42 V/nm), Mn which comes in close at 30 V/nm can provide ideal conditions a 20 pJ for all the elements to meet stoichiometry. However, with Al at ~15 V/nm, a compromise has to be made, where lower energies (0.5-5 pJ) are suitable for Al analysis and higher laser energies (20 pJ) for Ni and Co analysis. Our study also explains how other reports in literature which were analyzed at particular laser energies were either completely off in their quantitative compositions or could be accurate for the transition metals. Moreover, none of the aforementioned studies have explored the parametric investigation in presence of Al, such as NCA, where a careful quantitative analysis will be more challenging.

5.4 Conclusion

In conclusion, a parametric investigation of the effect of laser energy on the quantitative composition of pristine NCA cathodes was carried out. The analysis indicated that the presence of Al, a low evaporation field element with Ni and Co (high evaporation field elements) leads to a complex behavior where all three

elements donot reach ideal stoichiometry at one particular laser energy. Al composition is better quantified at lower laser energies and Ni and Co better at higher laser energies. On comparison with NMC811, where Al is replaced with Mn, 20 pJ of laser energy provides accurate composition. The reasons for this behavior based on the interplay between the evaporation field of both the elemental and oxide species is discussed and how the analysis pertains to more relevant parameters for the community such as Ni/Co, Ni/Mn ratio. Through our work, we have provided very clear directions on how future analysis of both NMC and NCA can be carried, specially before and after cycling to get more quantitative results from APT.

5.5 Acknowledgements

Chapter 5, in full, is currently being prepared for submission for publication, Parikh, P., Chung, H., Vo, E., Banerjee, A., Devaraj, A. & Meng, Y.S. On the stoichiometric quantification of high nickel content NCA and NMC battery oxides using Atom Probe Tomography. The dissertation author was the primary investigator and author of this paper. Haelie (Hyesueng Chung) was responsible for the electrochemistry for NCA cathodes. Ethan helped with the APT data acquisition.

Chapter 6 : Direct observation of Li during first cycle lithiation of silicon anodes

6.1 Introduction

Li-ion batteries are at the center of the next energy revolution, with intensive efforts on materials chemistry development, lifetime diagnosis, novel electrode processing and production line manufacturing occurring all over the world. At the electrode level, while the cathode has seen great improvements with the introduction of both NMC and NCA[2,5], graphite has and continues to be the anode of choice. The introduction of alloy anodes, that have high specific capacities and high gravimetric energy densities[3,4,6], can now lead to improvements in anode chemistries, with silicon that can compete with graphite on cost. An environmentally benign nature (at micro-scale), low operating potentials versus Li and compatibility with current slurry processing techniques are other advantages that make it an attractive choice[62].

However, the large volume expansion that plagues all alloy anodes including silicon, creates issues at the electrode level that causes rapid capacity fade. These issues, such as electrical isolation of the electrode, particle pulverization due to the mechanical stress and continuous consumption of electrolyte forming a thicker SEI-solid electrolyte interphase (hindering Li transport), are all a result of lithiation of the silicon particles[81].

While multiple mitigative strategies exist at the electrode level such as tailoring of the binder through supramolecular chemistry[65,66], use of intermetallic

matrices[163], thin film based anodes[75], formation of silicon-carbon composites[69,70], tailoring the silicon shape, size and morphology[62,72,74] and also restricting the operating potentials, the crux of the issue still pertains to volume expansion and subsequent contraction.

In this respect, various reports have tried to better understand this lithiation process. Gu et al.[77] observed the in-situ lithiation of silicon anodes both during charge and discharge by embedding nanoparticles onto a carbon fiber. Using transmission electron microscopy (TEM), they were able to observe the formation of a distinct interface between silicon and lithiated silicon during first charge and subsequent formation of porous silicon right after discharge, possibly indicative of Li clusters. McDowell et al.[78] expanded on this understanding by carrying out the in-situ TEM study on hydrogenated amorphous silicon nanoparticles (on a silicon nanopillar), where a two-phase reaction mechanism was proposed for lithiation similar to crystalline silicon. Amorphous silicon does not undergo pulverization until ~870 nm unlike crystalline silicon that can pulverize above ~ 160nm.

Liu et al.[164] also used in-situ TEM and theoretical calculations to measure the kinetics of lithiation in silicon nanowires. They proposed a self-limiting mechanism that would prevent further lithiation of the crystalline core due to the stress from the lithiated phase ultimately slowing down the lithiation rate. Seidlhofer et al.[165] studied the lithiation in silicon thin films using operando neutron reflectivity to observe the formation of a surface Li rich region ($Li_{2.5}Si$) and a deeper growth region with lower Li content ($Li_{1.1}Si$) compared to the surface. Radvanyi et

al.[166] also provided a similar composition content of $Li_{3.1}Si$, in the lithiated shell of microsilicon particles. To this end, Shen et al.[79], also observed the lithiation behavior in porous silicon showing a larger fracture diameter of ~1.52 μm than previously reported of 160 nm in nanoparticles. Liu et al.[80] also observed anisotropic volume expansion in silicon nanowires and peeling mechanism at the atomic scale in (111) direction for the formation of Li_xSi[167].

All these studies, explored how the lithiation happens with different silicon morphologies, proposing uniform lithiation layers with single composition and sharp interfaces where the lithium content drops off rapidly in nano and micrometer sized particles. However, right at the interface, the amorphous nature of Li_xSi prevents any additional analysis of the lithium distribution (being investigated using TEM) and the depth resolution provided by Auger electron spectroscopy is in tens of nms at best. Understanding this interface is critical since it determines the onset of the strain that is responsible for the effects observed at the macroscale.

Moreover, observing Li in itself is a daunting challenge, with only recently, successful measurements carried out using cryo-FIB and cryo-TEM on lithium metal anodes[168]. To study lithiated silicon anodes though at the nanoscale, we devised the use of atom probe tomography (APT), that can directly observe Li. Moreover, the presence of silicon and Li_xSi, an alloy would make APT data acquisition relatively straightforward as compared to the more complex oxide analysis. Using an environmental transfer chamber, we ensure no air exposure between the glovebox to FIB to APT instruments. Through our analysis on the

lithiated silicon, [1] at the onset of lithiation, [2] full lithiation upto 50 mV and [3] In the delithiated state, we provide a comprehensive understanding of the Li distribution in each case and a robust method to analyze lithiated systems using APT.

6.2 Methods

Electrode processing: Silicon anodes were prepared using powder with an average size of 1-5 μm obtained from Alfa Aesar. The electrode composition is 50 wt% silicon, 25 wt% of super P carbon (obtained from MTI Corp) and 25 wt% of a composite binder with equal wt% of PAA and CMC. The stock solution of 3.2 wt % of CMC-Na (sodium carboxymethyl cellulose, M_w 250 000, Sigma-Aldrich) dissolved overnight in deionized (DI) water and 10 wt% for PAA (M_v of 450,000 Da and obtained from Sigma Aldrich) was used. A Si:C composite was first prepared by mixing 0.504 g of Si and 0.252 g of Super P carbon in a glovebox and milled (outside the glovebox) at 300 rpm for 46 minutes with a 15 min rest period. The binder solution (dissolved in deionized water) was added next to the Si:C composite, in this case both the CMC and PAA solutions one after another.

This was followed by a second mixing step in a Thinky mixer through a multi-step process starting at 500 rpm for 1 minute, then 1000 rpm for another minute and finally at 1800 rpm for another 9 minutes. Each step contained a minute of rest in between to allow cooling of the slurry.

The obtained slurry was coated on a copper foil by using a doctor blade and the as prepared electrode was dried at 80 °C overnight under a vacuum to

completely remove residual water in the electrode. Following this another heating step at 160°C was carried out for 2 hours to copolymerize the CMC-PAA into one branched polymer network. This step was based on a modified protocol based on the work on nanoparticles of silicon by Koo et al[169].

Test samples for optimizing the entire process from electrode processing to APT analysis were first carried out on electrodes with only the PAA binder at 6 wt% stock solution maintaining the loading and without the additional heating step at 160°C. These electrodes did not undergo the composite processing step for Si:C in the ball mill as mentioned for the CMC-PAA since the ball milled samples did not give reproducible electrochemistry at silicon anode loadings of 1 mg/cm^2.

Coin cell fabrication: The electrode sheet was cut into a disk and used for the battery tests. The mass of the Si active material on the electrode was ~1 mg/cm^2, which is equivalent to ~2.5 mAh/cm^2. This electrode was assembled in a 2032 coin cell using a polymer separator (C480, Celgard Inc., USA). A carbonate based electrolyte of equal weights of ethylene carbonate and diethylene carbonate (EC:DEC) with 10 wt% of fluoroethylene carbonate (FEC) as an additive was used. The electrolyte was obtained from Gotion and used as is. Battery-grade lithium metal was chosen as the counter electrode. Coin cells were assembled in a glovebox purged with Ar gas and maintained at a moisture level at or below 5 ppm.

Electrochemical tests: The coin cells were assembled, and electrochemical performance tests were performed using an Arbin battery cycler in galvanostatic mode, limiting the charge and discharge potentials to 1.0 V and 0.05 V vs. the Li

counter electrode (note that “charge” here refers to lithium alloying into the Si anode or lithiation). The open circuit voltage of the coin cells was monitored for 24 hours (10 hours for samples with PAA binder) to allow the electrolyte to completely wet the electrode and then the cells were charged and discharged at a C-rate of C/20 for the formation cycle and C/10 for subsequent cycles (only for cells monitored for their electrochemical cycling retention). For the initial lithiation study, a C-rate of C/20 was used. The percent capacity retention was calculated with respect to the first discharge capacity. All electrochemical measurements were carried out at room temperature in ambient.

Sample transfer protocols: Prepared coin cells were then disassembled using a de-crimping die and washed with 150 µl of dimethyl carbonate (DMC) and dried in an the Ar glovebox. The dried disks were then cut into smaller pieces that could fit into a regular sized SEM stub with the microtip array attached on it (Refer to Appendix C Figure C.1). This limitation was based on the maximum stub size that could fit into the environmental transfer rod used for air-free transfer to the load lock of the Scios Dualbeam/focused ion beam (FIB) instrument at the San Diego Nanotechnology Infrastructure (SDNI) of UC, San Diego. Care was taken to ensure that the carbon tape used for this initial transfer and sample preparation process was devoid of any moisture, by drying it at 50°C in a drying oven for 24 hours, a half hour vacuum drying in the glovebox antechamber and an additional storage of 24 hours in an Ar filled glovebox before being used. Residual moisture from the tape was found to significantly affect the surface morphology (as seen in

Appendix C Figure C.1. From the 4 set of samples, (a) test samples (with PAA binder only) lithiated to 50 mV, (b) CMC-PAA samples lithiated to 0.1 V (onset of lithiation), (c) CMC-PAA samples lithiated to 50 mV (fully lithiated state) and (d) CMC-PAA samples lithiated to 50 mV and delithiated to 1V; individual silicon particles for samples (a) and (c) were picked up and placed onto microtip arrays at UCSD and the (b) and (d) at PNNL itself in the same manner. The pick and place here was directly from the electrode itself using the micromanipulator, as shown in Figure 6.2 (d-f).

APT specimen tip preparation using cryo FIB: The prepared samples, once placed onto microtip arrays, were then coated with electron beam and ion beam Pt to ensure that a good seal before being transported to PNNL. Care was taken to ensure minimal exposure of the sample to electron and ion beam due to the sensitive nature of the sample. Following this, the samples on a microtip array, attached on an SEM stub were brought back into the glovebox. The microtip array was carefully detached from the stub and attached onto a Cu clip which could then be loaded back into the Quanta FIB at the Environmental Molecular Sciences Laboratory at PNNL, for further processing and then directly into the APT using an air-free transfer shuttle developed in-house at PNNL.

For annular milling, the FIB was cooled down to liquid nitrogen temperatures and the milling and tip sharpening process carried out then to prevent any Li diffusion. Importantly, this annular milling process was carried out with the microtip held by a Cu clip instead of carbon tape on the SEM stub, since the carbon

adhesive was seen to become brittle at cryo temperatures (Appendix C Figure C.2 (c)). Also, the milling process at room temperature did not create any change in morphology of the specimen, unlike that seen with Li metal itself (also shown in Appendix C Figure C.2 (a, b)), however cryo-milling ensured that any concerns with damage to Li if at all could be alleviated.

APT data acquisition and analysis: Right after the tip sharpening process, the prepared tip specimens were transferred into the APT system using the environmental transfer shuttle and through specifically designed high vacuum ($<10^{-7}$ mbar) chamber directly in the buffer of a LEAP 4000 XHR at the Environmental Molecular Sciences Laboratory at Pacific Northwest National Laboratory, Richland, WA, USA. The data acquisition was carried out at a base temperature of 40 K and laser energy of 20 pJ for final analysis, with a pulse repetition rate of 125 kHz. The obtained data was reconstructed using the IVAS software with a tip image-based reconstruction.

6.3 Results and discussions

In order to understand the lithiation mechanisms, the electrochemical performance of the silicon anodes needs to be investigated first. The first cycle charge and discharge voltage profile is shown in Figure 6.1 ((a) for the test sample and (b-d) for the analyzed samples). Micrometer sized silicon is taken as the morphology of choice since the nanosized particles (~50 nm) are difficult to prepare into specimen tips using the pick and place method in FIB. The anodes give a practical reversible (discharge) capacity of 2529 mAh/g and a coulombic

efficiency (CE) of 83% which is similar to the specific capacities obtained in literature[72]. However, the capacity retention is poor due to pulverization of the particles associated with the mechanical stress due to volume expansion and contraction (Appendix C Figure C.3). With the primary focus here on understanding the lithiation mechanism, which is independent of the type of binder chemistry (as seen through the comparison between the first cycle voltage profiles in Figure 6.1 (a) versus (d)), efforts on improving the capacity retention have not been investigated. However, the obtained specific capacity in the first cycle indicates that the processing and the galvanostatic testing conditions used are optimal and donot affect the interpretation of the results in any way. Another point to note is that the half-cells are allowed to equilibrate before disassembly providing for a realistic ex-situ analysis of the lithium distribution.

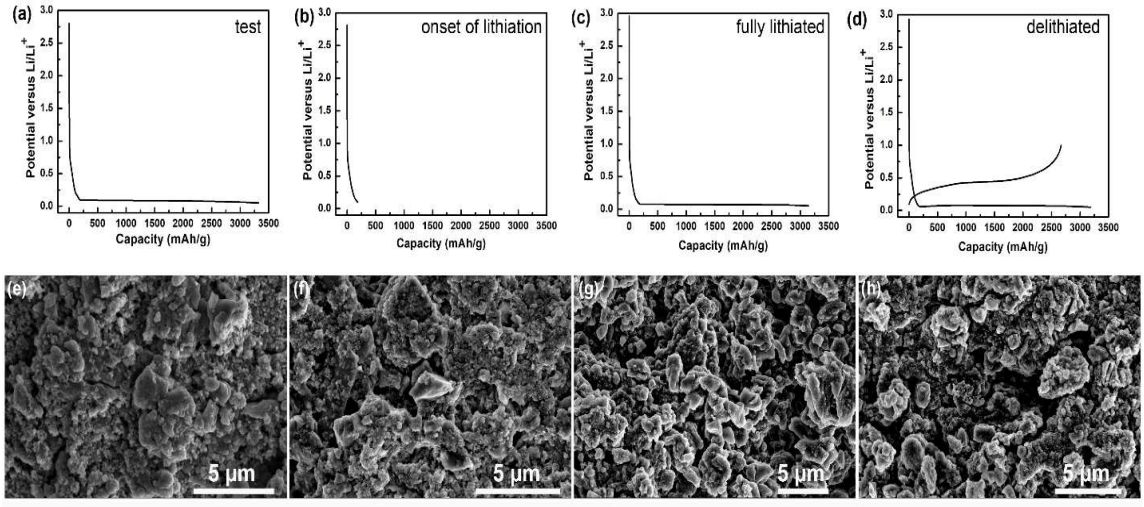

Figure 6.1: Voltage profiles and SEM images for all 4 sets of samples analyzed including the test sample.

Based on the optimized electrochemistry, the specimen tip preparation is carried out next. As mentioned in the Methods section, the samples at different state of charge are evaluated (fully lithiated with PAA binder as test samples, with CMC-PAA binder (1) lithiated to 0.1 V, (2) fully lithiated to 50 mV and (3) fully delithiated to 1 V). Even before any nanoscale analysis is carried out, the scanning electron microscopy (SEM) images seen in Figure 6.1 (e-h), show differences within the first cycle itself. For the sample, lithiated to 0.1 V (onset of lithiation); Figure 6.1 (f), the clear facets of the crystalline silicon micro particles are still observed. On further lithiation to 50 mV, the swelling of individual particles, indicate of the volume expansion and formation of amorphous Li_xSi are seen (Figure 6.1 (g)). At 1V, after delithiation (Figure 6.1 (h)), the formation of cracks is already seen showing that the initial (formation) cycle is critical in silicon anodes for long term cycling.

The specimen tip preparation is carried out as per the protocol shown in Figure 6.2. In brief, the disassembled electrodes, as seen in Figure 6.2 (a), are placed onto an SEM stub with a microtip array inside an Ar filled glovebox. The samples are then directly transferred into the FIB system using an environmental chamber that can be brought into the glovebox and is fitted to the loadlock chamber, and then directly transferred into the main chamber of a FIB system (Figure 6.2 (b, c)). The sample stage (both at UCSD and PNNL) are fitted with nitrogen gas lines connected to liquid nitrogen tanks that can cool the sample close to liquid nitrogen temperatures (~-185-150°C) The environmental transfer is an

important step of the process since the electrodes are highly sensitive to moisture. In the presence of even 50 µl deionized water on the electrode surface, rapid bubbling and complete washing away of the electrode is seen (evidence for this is provided in Appendix C Figure C.4). Another important step is the presence of silicon within the annular milling region for the final specimen tip preparation. To ensure this, on test samples energy dispersive x-ray spectroscopy (EDX) is carried out to identify, which contrast in the SEM corresponds to which region (Si or carbon). Evidence for this is shown in Appendix C Figure C.2 (a, b).

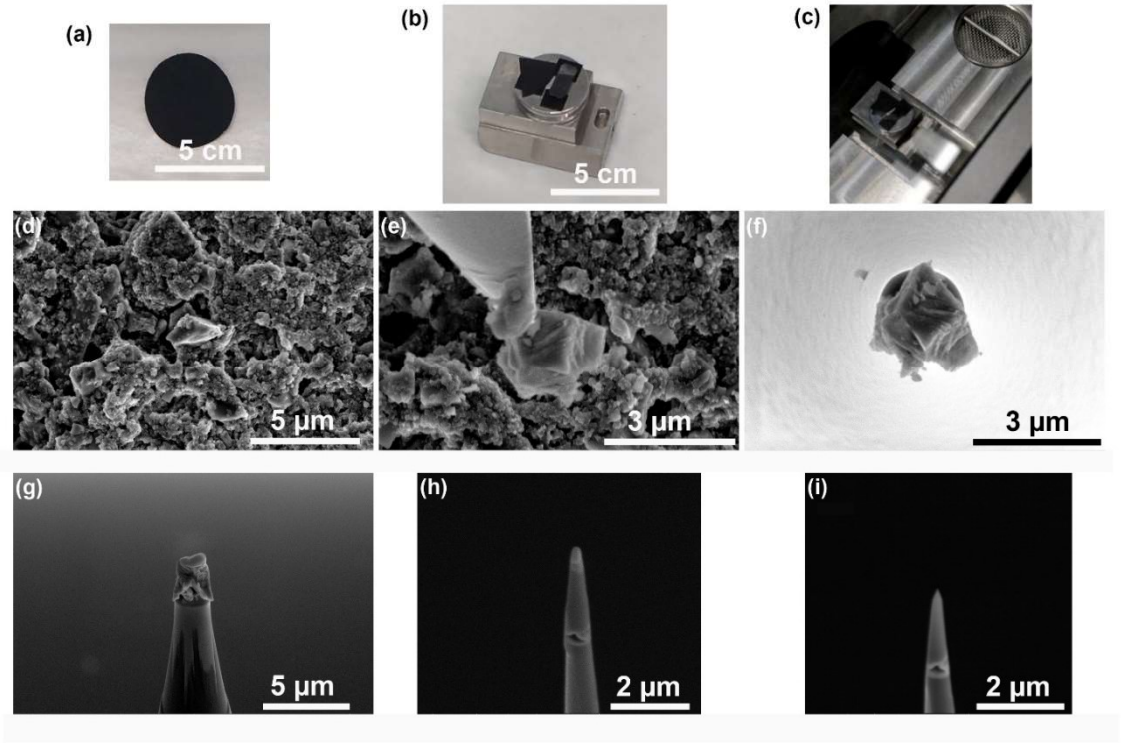

Figure 6.2: Specimen tip preparation shown for the sample at the onset of lithiation (0.1V). (a) Disassembled electrode, (b) shows a piece of the electrode attached adjacent to the microtip array on a single SEM stub, (c) direct transfer to the loadlock of a Scios FIB, without air exposure, (d-f) shows the direct pick and place directly from the electrode followed by (g-i) annular milling to obtain the final tip.

The APT data acquisition was carried out first on test samples, to ensure that evaporation of Si and Li are seen, and any optimization needed for the laser energy is carried out. Since the tips were essentially, Li, Si and Li_xSi alloy primarily, without any oxides in there, a change in composition with laser energy is not expected in there. Hence, a laser energy of 20 pJ is used. Lower laser energies are not sufficient to allow evaporation until very large base DC voltages of 4-5 kV are reached, leading to a very small (200-300k ions) number of evaporation ions and not sufficient z depth for a good analysis. At higher laser energies (40 pJ and higher), non-uniform preferential evaporation of Li is seen. After running multiple samples from the test batch at 20 pJ, the actual samples at different state of charge were then run at the same conditions. The initial runs analyzed using the IVAS software showed a clear distinct interface between Li and Si indicating the prowess of APT for intended analysis. The concentration profile is shown in the Appendix C Figure C.5, where a clear interface with Li on one side and Si on the other is seen. However, an increase in the oxygen composition is also seen at the interface, and a slight increase in Ga and Pt, were concerning at first. This was possibly due to accidental air (moisture) exposure or reaction of the Li with the surface silicon oxides. But analysis of the other samples (as seen in Figure 6.3, showed no presence of O, Ga or Pt (less than 0.2%), when the samples were not fully lithiated indicating that this species were possibly from the electrolyte decomposition and pulverization of the silicon anode. Hence the profiles obtained are representative of realistic conditions in a silicon anode and not based on

lithiation of particles in absence of binder or electrolyte or carbon, as seen in previous reports.

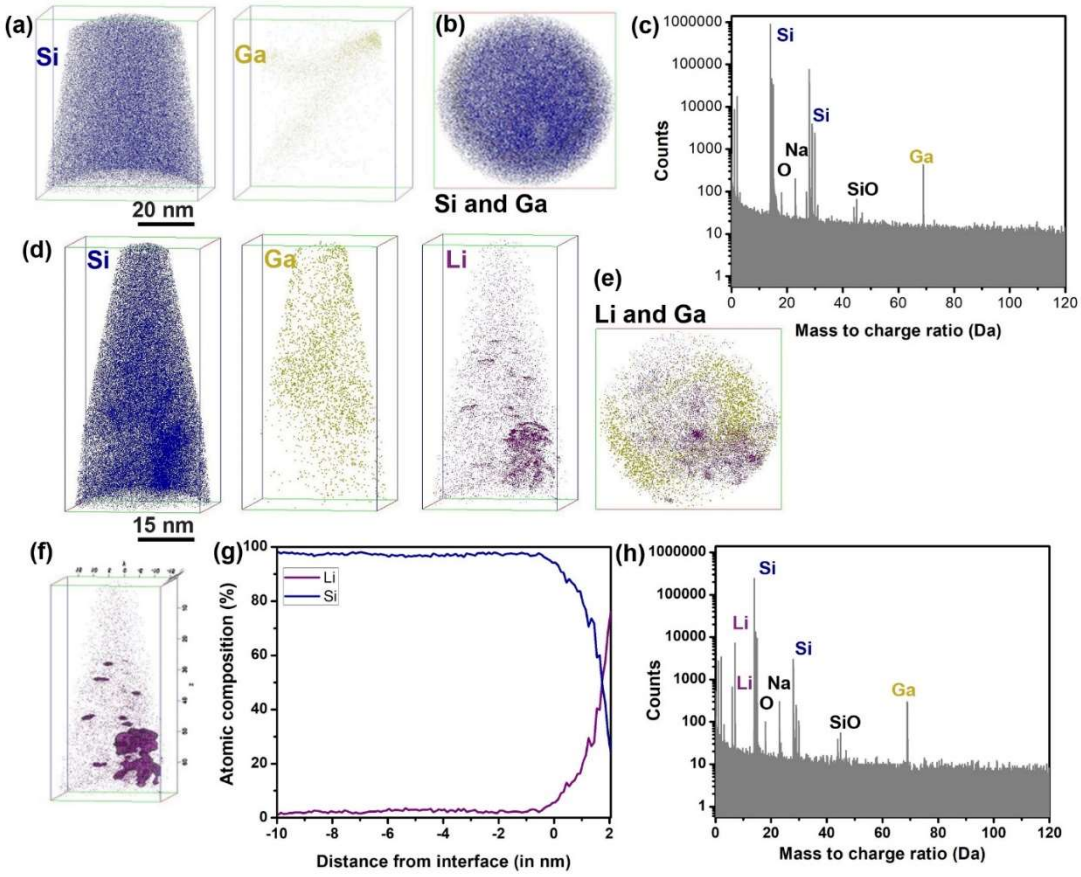

Figure 6.3: APT maps and analysis for samples at 0.1 V, onset of lithiation (a-c), and 1V, delithiated (d-h). At 0.1V, more than 99% of the composition is Si, and the top view pattern (b), shows that absence of the X-pattern characteristic of Si microtip, indicating the Si is from the electrode. On delithiation, Li is seen, possibly trapped in the silicon electrode (d) however, the Li and Ga distributions are not at the same spatial position (e). The Na in the mass spectrum (c, h) is from the binder.

For the samples analyzed at the onset of lithiation, the composition contains primary of Si (>99%) with no Li. The mass spectrum shows the presence of Ga and O but at concentrations less than 1%. This was following the same process used for other samples, indicating that the effect of moisture, oxygen during the

processing did not influence the results and the success of the protocols followed for an air-free transfer. Also, the evaporation of silicon from the anode as opposed to the base of the microtip arrays (seen from the top view of the atom probe maps, Figure 6.3 (b)), is verified due to the absence of an X-feature in the evaporation pattern, which is characteristic of the microtip array. The compositions and analysis obtained is seen in Figure 6.3.

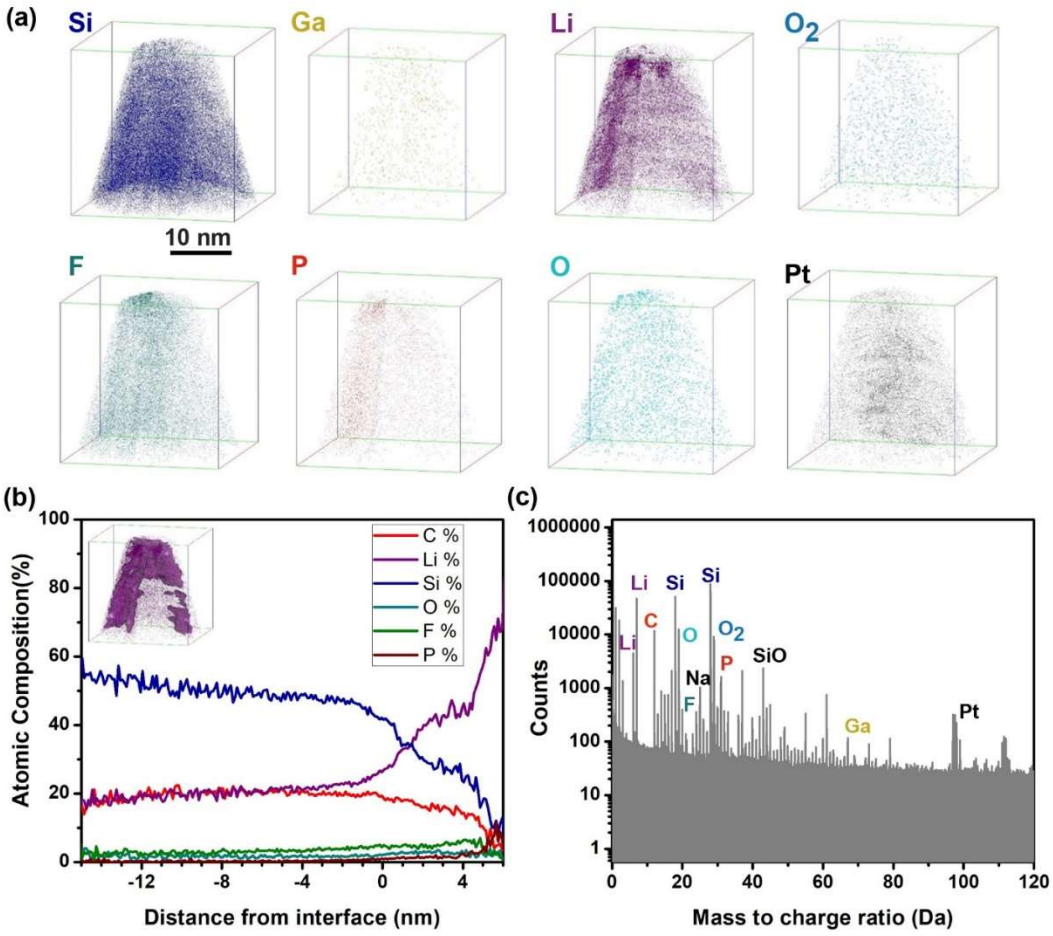

Figure 6.4: Atom probe maps and mass spectrum analysis for fully lithiated samples at 50 mV.

At the fully lithiated state at 50 mV, the mass spectrum (as compared to 0.1 V and 1 V both) is more complex with the presence of both electrolyte decomposition species and carbon, from the silicon-carbon composite formed (Figure 6.4 (c)). As seen in Figure 6.1 (g), the volume expansion and particle pulverization prevent uniform silicon evaporation and a host of different species are seen. However, as seen with the atom probe maps (Figure 6.4 (a)), clear regions of silicon and Li all along the depth of the reconstructed maps is seen in different distinct regions. The presence of the inhomogeneous composition, along with those for the 1V sample, indicates that the features observed, are not an artefact or from the APT evaporation dynamics but as a result of the sample itself.

Additional analysis of the obtained maps using iso-concentration surfaces (at Li % of 20) and proxigram maps across the interface (Figure 6.3 (g) and Figure 6.4 (c)) clearly show how the gradual decrease in the Si concentration and increase in Li concentration that is more rapid away from the interface. Towards the end of the interface, at a distance of 6 nm from the iso-concentration surface (for Figure 6.4 (c)), the sharp increase in Li is accompanied by an increase in the P and F distributions also indicative of $LiPF_6$ salt from the electrolyte or its decomposition product. However, across the entire atom probe maps and as seen in the composition table in Appendix C Table C.1, the total Li concentration is far greater than both F and P as well as O indicating that the Li seen is as a result of lithiation of Si and not in its entirety from any electrolyte salt or any Li carbonates, inorganic Li species in the solid electrolyte interphase (SEI).

Additionally, and more surprisingly, at the fully delithiated state at 1V, the presence of Li is seen in some specimen tips (Figure 6.3 (d)). The mass spectrum here too is far simpler showing, primarily Si as seen with ~ 1.8 % Li. However, Li isoconcentration surfaces at 20% Li in the APT maps show the presence of Li clusters. In this respect, Gu et al.[77] had observed the presence of porous Si on first delithiation, hinting at Li cluster formation. Here, we provide direct proof of these clusters. However, the Li clusters are not seen in all specimen tips, which means that the volume expansion and contraction at the electrode level is very disjointed.

Having directly observed the Li maps at different state of charge, the discussion follows as such. At the onset of lithiation, the silicon is crystalline with no contamination of O into the particle, either from the electrode processing or the FIB conditions or APT analysis. As lithiation proceeds, the particles swell and pulverize as they get lithiated. The lithiated silicon-silicon interface does not contain a sharp Li distribution but it gradually increases over ~5 nm, thus distributing the strain. Having a smaller particle size or pores, hence, would help with the recovery of the strain on delithiation possibly better than larger particles. On delithiation though, the Li does not completely leave the silicon particles and in some places is trapped in the structure, either inducing residual strain or in other forms, ultimately leading to Li loss and capacity fade. By observing the Li profiles directly, the strain in the system is better understood and new mitigative strategies based on the lithiation mechanism can be developed.

6.4 Conclusion

Direct observation of the Li distribution profiles was carried using APT, in conjunction with milling and sample transfer protocols that prevented any exposure to ambient. The analysis at the different state of charge showed a gradual increase in the Li concentration across the interface for ~ 5 nm and not a sudden sharp rise as proposed in other reports. The presence of Li on delithiation also indicated either trapped Li or presence of residual strain, both of which are detrimental to the silicon anode. Our findings give a clear understanding of how direct observation of Li at the nanoscale is necessary for such critical lithiation studies and how our protocols can be transferred to analyze other sensitive components and materials in Li-ion batteries.

6.5 Acknowledgements

Chapter 6, in full, is currently being prepared for submission for publication, Parikh, P., Zhang, Y., Damien, D., Trieu, O., Fang, C., Banerjee, A., Perea, D., Devaraj, A. & Meng, Y.S. Direct observation of Li during first cycle lithiation of silicon anodes. The dissertation author was the primary investigator and author of this paper.

Chapter 7 : Role of 4-tert-Butylpyridine as a Hole Transport Layer Morphological Controller in Perovskite Solar Cells

7.1 Introduction

As an emerging photovoltaic technology with significant potential for commercialization, hybrid organic−inorganic perovskite solar cells (PSCs) have developed rapidly in recent years[16,170–172]. With a certified 22.1% power conversion efficiency,[9] compatibility with flexible substrates,[173,174] and low fabrication energy consumption,[175–177] PSCs are attracting enormous interest in both the academic and industrial field. As a p−i−n junction solar cell, a typical PSC has multiple layers and interfaces[26,178]. Understanding the function of these components in PSCs can facilitate improvements in device efficiency and stability[179]. Currently, a large number of researchers are focused on understanding the working mechanisms of the perovskite intrinsic layer and electron transport layer[178,180–182]. However, investigations into the role of additives in the hole transport layer (HTL) remain relatively limited[183–185].

Traditionally, the HTL for PSCs consists of 2,2′,7,7′- tetrakis(N,N-di-p-methoxyphenylamine)-9,9′-spirobifluorene(Spiro-OMeTAD), bis(trifluoromethane)sulfonimide lithium salt (LiTFSI), and 4-tert-butylpyridine (tBP) (For molecular structures of the HTL components see Supporting Information, Figure D.1)[171]. This combination was first applied in solid state dye-sensitized solar cells (ss-DSSC)[186,187]. In ss-DSSC, Spiro- OMeTAD is the hole transport material, LiTFSI is the p-dopant, and tBP is the additive that acts as a

recombination blocking agent[186,188]. The function of tBP in ss-DSSC is the same as in liquid-based DSSC: tBP can adsorb on the surface of mesoporous TiO_2, which is the photoanode for DSSC. The adsorption of tBP on TiO_2: (1) suppresses direct contact between TiO_2 and electrolytes/hole transport materials to reduce charge recombination; and (2) negatively shifts the TiO_2 conduction band to increase the V_{oc} of DSSC[189,190]. Due to the similarity in the device architecture for ss-DSSC and PSC, tBP is assumed to fulfill the same role in PSCs as in liquid-based DSSC or ss-DSSC[188,191,192].

However, in DSSC, dyes are discrete organic molecules which are difficult to organize into a continuous layer, whereas in PSCs, the intrinsic perovskite layer penetrates into the pores of the TiO_2 layer and also tops it as a capping layer. This suppresses the possibility of direct contact between tBP and TiO_2. Moreover, in ss-DSSC, LiTFSI triggers the oxidation of Spiro-OMeTAD[193,194]. In PSCs, despite the LiTFSI trigger, the oxidation reaction can only proceed if the perovskite layer also contributes to this process in a certain spectral range (>450 nm)[195]. The combined effect of the perovskite capping layer and the spectral dependence of the oxidation reaction would allow new interactions among the components in HTL (specifically tBP) and between the HTL and intrinsic perovskite layer. This calls for a re-evaluation of the role of tBP as a charge recombination inhibitor and investigations into new interactions between the perovskite capping layer and tBP. Such detailed studies will ultimately help researchers clearly understand how

PSCs works and provide effective solutions to the stability issue ensuring better success of this technology toward commercialization.

Recent reports have observed pin-holes in the HTL of PSCs[46]. These are considered to contribute to the poor stability of PSCs; oxygen and moisture in ambient environment can permeate through these pin-holes and cause degradation of the perovskite intrinsic layer, but the reason for the generation of pin-holes in HTL is still unclear[47].

In this work, tBP is found to function as a morphology controller in the HTL of PSCs. Our observations suggest that, tBP reduces phase separation in the stock solution prior to spin-coating. This effect improves the film quality of the HTL by decreasing inhomogeneous regions. Using scanning electron microscopy (SEM), we prove that the presence of tBP significantly influences the HTL surface, by reducing the number of “pits” (also reported as pinholes[46,47]). On the other hand, high-resolution cross-section transmission electron microscopy (TEM) images show that the HTL undergoes morphological changes after long-term (>1000 h) storage of PSC. With the help of atom probe tomography (APT), 3D visualization of the water distribution at HTL/perovskite interface is possible. By combining the phenomena, we observe in TEM and APT, a PSC failure process mechanism is proposed, along with the morphological change of the HTL due to the evaporation of tBP. Our results indicate that tBP not only fulfills its function as previously reported for ss-DSSC but also acts as a morphology controller directly affecting device stability.

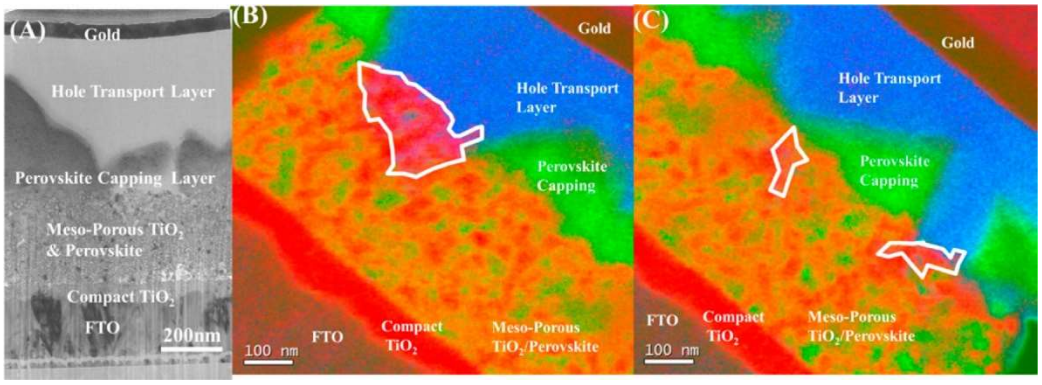

Figure 7.1: Correlation between perovskite coverage and HTL infiltration. (a) Bright-field TEM cross-section image of PSC prepared by focused ion beam (FIB). (b) Energy filtered-TEM mapping of a PSC cross-section with poor perovskite coverage. (Blue indicates Spiro-OMeTAD, red TiO_2, and green perovskite. Regions where the HTL infiltrates the mesoporous TiO_2 are outlined in white.) (c) EF-TEM mapping of a PSC cross-section with rich perovskite coverage. (Blue indicates Spiro-OMeTAD, red TiO_2, and green perovskite. Regions where the HTL infiltrates the mesoporous TiO_2 are outlined in white.)

7.2 HTL Infiltration Behavior in PSCs

The majority of our samples in this study are prepared by focused ion beam (FIB) and were utilized high-quality SEM and TEM imaging[196–199]: The FIB milling/polishing process ensured that the sample had a smooth surface. Furthermore, using a FIB-based milling process allowed the sample to be thinned to the 100 nm required for TEM characterization. As shown in Figure 7.1 (a), the morphological contrast for every layer in PSC is distinguishable in BF-TEM. Based on FIB-prepared PSC samples for cross-section TEM imaging, we progress toward understanding the infiltration extent of HTL in PSCs. In ss-DSSC, the pore filling percentage of the HTL in a mesoporous TiO_2 photoanode is around 60−85% (the thickness of mesoporous TiO_2 is ~2.8 μm)[200,201]. These reports also demonstrate that reducing mesoporous TiO_2 layer thickness can increase the pore filling

percentage. In mesoporous TiO_2-based PSCs, the optimized thickness of mesoporous TiO_2 is around 300−400 nm[171]. If the HTL infiltrates into mesoporous TiO_2 to the same extent as it does in ss-DSSCs, the pore filling percentage in PSCs should be higher than 60−85% because of the thinner TiO_2. However, our observations show that the pore filling percentage of the HTL in TiO_2 is much lower than 60% due to the presence of the perovskite layer that has infiltrated the mesoporous TiO_2 layer.

In PSC, the majority of the TiO_2 surface is covered with a perovskite capping layer, although some regions have poor coverage. Here, three components cross-section energy filtered TEM (EF-TEM) mapping is applied to display the infiltration behavior of HTL under the competing effect of the perovskite infiltration in mesoporous TiO_2. Two PSC samples were prepared by FIB for EF-TEM, one with poor perovskite capping layer coverage on top of the mesoporous TiO_2, the other one with rich perovskite capping layer coverage. As shown in Figure 7.1 (b), even in perovskite poor coverage regions, the infiltration of the HTL into mesoporous TiO_2 is limited. Most of the pores within the TiO_2 layer are filled with perovskite instead of HTL (Figure 7.1 (b) green regions). In TiO_2 with pores deeper than 150 nm from the surface, no HTL is observed. However, when the perovskite coverage is better, as shown in Figure 7.1 (c), the area of TiO_2 infiltrated by the HTL is even smaller. The EF-TEM mapping indicated that under the competition of the perovskite, the infiltration of the HTL to mesoporous TiO_2 is limited. The more

perovskite capping layer cover on top of TiO_2 the less the HTL can infiltrate into the mesoporous TiO_2.

In previous reports, a penetration depth of ~100 nm for the HTL is observed, which show strong agreement with our experimental observations[198]. Since then, several groups have adopted superior fabrication procedures. A denser perovskite capping layer can further limit the pore-filling of the HTL in TiO_2. Moreover, in planar heterojunction PSCs, which are devoid of mesoporous TiO_2, the TiO_2/HTL interface is further reduced. However, tBP is still used in majority of PSC architectures and device configurations. Hence, it should function differently in PSCs than in DSSCs.

7.3 tBP HTL Morphology Control Effect

Due to the limited penetration depth and low pore filling percentage, the TiO_2/ HTL interface in PSCs is much smaller than in ss-DSSCs. As a result, tBP acts only minimally to prevent direct contact between Spiro-OMeTAD and TiO_2. However, as we observe, tBP does control the morphology of the HTL.

Before adding tBP, as shown in Figure 7.2 (a), the HTL solution used for spin-coating is phase-separated: the LiTFSI/acetonitrile solution (acetonitrile is the solvent to dissolve LiTFSI before adding to Spiro-OMeTAD solution) is immiscible with the Spiro-OMeTAD/chlorobenzene solution (chlorobenzene is the solvent for spin-coating of HTL). The majority of the LiTFSI/acetonitrile solution tends to accumulate at the bottom of the Spiro-OMeTAD/chlorobenzene solution as small liquid droplets. After adding tBP, as shown in Figure 7.2 (b), all liquid droplets

disappear, which indicates that tBP improves the solubility of LiTFSI in the Spiro-OMeTAD solution. It is possible that some complexes are formed by tBP and LiTFSI to reduce the phase separation in HTL solution and further influence the morphology of the HTL after spin-coating.

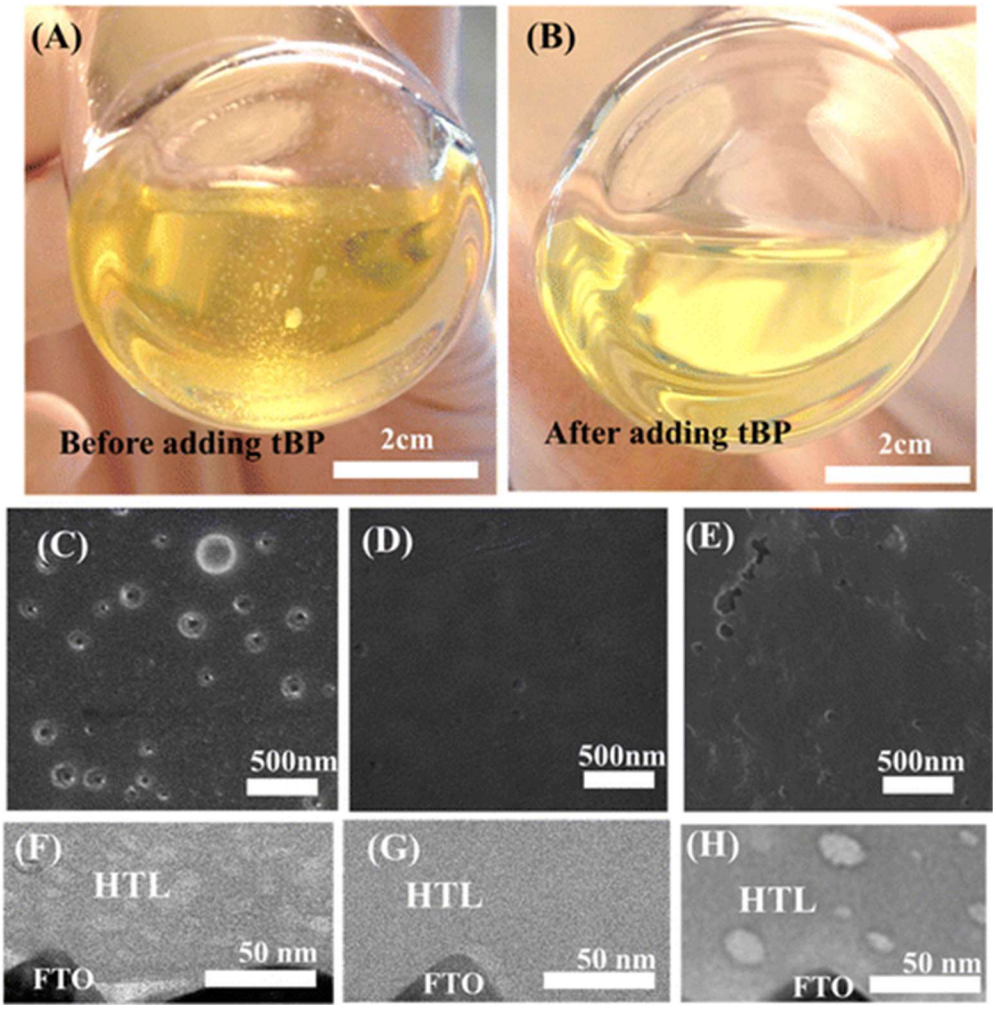

Figure 7.2: Photographs of HTL solution used for spin coating. (a) Before adding tBP and (b) after adding tBP. Top-view SEM images of the freshly prepared HTL (c) without tBP, (d) with tBP, and (e) with tBP after overnight vacuum treatment (10^{-4} Pa). Cross-section BF-TEM images of the freshly prepared HTL (f) without tBP, (g) with tBP, and (h) with tBP after overnight vacuum treatment (10^{-4} Pa).

Because the existence of tBP guarantees the uniformity of HTL solution, as a result, it can affect the morphology of the spin-coated films. Several freshly prepared HTL samples were characterized by SEM/TEM as shown in Figure 7.2 (c−h). In Figure 7.2 (c), a top-view SEM image show that pits form on the surface of the HTL in the absence of tBP. After adding tBP, as Figure 7.2 (d) displays, both the size and the number of the pits are significantly reduced. The homogeneous nature of the solution facilitates formation of a uniform film with a limited number of pits.

In order to prove that these pits in the HTL are indeed formed due to a lack of tBP, overnight vacuum treatment (10^{-4} Pa) was applied to a HTL with tBP. It is reported that tBP evaporates under vacuum environment and no X-ray photoelectron spectroscopy signals are observed related to tBP elements[46]. As shown in Figure 7.2 (e), the number and the size of the pits on the surface of the HTL increase after overnight vacuum treatment. The morphological change from Figure 7.2 (d) to (e) can be attributed to the evaporation of tBP. Its disappearance/reduction causes the HTL film to revert back to an inhomogeneous state, thereby resulting in the reappearance of more pits. Moreover, a few pits are located in the HTL even with tBP (Figure 7.2 (d)), which we ascribe to the volatile nature of tBP on the surface. tBP can partially evaporate at the surface of the HTL, allowing a small portion of LiTFSI to regather and form pits.

To further study the morphological control of tBP on the HTL, FIB was used to prepare cross-section HTL samples with and without tBP. This enabled us to

observe the morphology of the bulk of the film via BF-TEM at high resolution. Figure 7.2 (f-h) are the BF-TEM images of the HTL cross-section without tBP, with tBP and with tBP after overnight treatment, respectively. In Figure 7.2 (f), without tBP, the HTL has an inhomogeneous morphology. Several bubble-like structures appear in the HTL. When the HTL contains tBP, as shown in Figure 7.2 (g), the bulk of the film is homogeneous. After overnight vacuum treatment of the tBP-contained film, Figure 7.2 (h), inhomogeneous regions appear again. For the various treatment histories, the morphology of the inhomogeneous regions in the tBP-free sample and that of the vacuum treatment tBP sample are slightly different, but the size and the distribution of the inhomogeneous regions for these two samples are in the same range.

In addition, we also characterized the tBP-contained film after thermal annealing. 200 °C was selected as the heat treatment temperature, as this temperature is above the boiling point of tBP and below the melting points for LiTFSI and Spiro-OMeTAD. The morphology of the top view (Supporting Information, Figure D.2 (a)) and the cross-section view (Supporting Information, Figure D.2 (b)) of the thermal annealing film is characterized. In Figure D.2 (a), the number and size of the pits on the surface of the HTL increase after heat treatment. However, the morphology and location of the inhomogeneous regions in cross-section image of the annealed tBP sample is different compared with the vacuum treatment sample and the tBP-free sample. The inhomogeneous regions of the tBP-free and vacuum treatment samples show more small bubble-like regions that

are mainly located at bulk of the film. These inhomogeneous regions show brighter contrast compared with the rest of the film. While in Figure D.2 (b), the annealed sample's inhomogeneous regions are on top of the film, they show darker contrast compared with the rest of the film. These differences can be attributed to the melting of LiTFSI on 200 °C homogenizes bulk of the thermal annealing film; however, it still cannot prevent the surface morphological change due to the evaporation of tBP. In conjunction with the top view SEM and cross-section TEM results (Figure 7.2 (c-h), Supporting Information Figure D.2 (a) and (b)), it is obvious that tBP can affect both the surface and bulk morphology of HTL.

Previous reports described the nonuniform structure of the HTL as "pinholes": the authors proposed that the pinholes pass through the entire HTL layer, which put moisture and air in direct contact with the surface of perovskite layer and trigger further degradation[46,47]. If pinholes did indeed exist in the HTL, a cross-section TEM image of a PSC would reveal this specific morphology. However, the cross-section TEM images (Figures 7.1 and 7.2) prove that the HTL is uniform (in the presence of tBP). In Supporting Information, Figure D.3, a cross-section BF-TEM image of a PSC showing a larger region for the HTL also indicates that the bulk of the HTL is homogeneous and contains no pinholes. On the other hand, the metal (top electrode)/HTL interface is not flat, which suggests that the surface morphology has shallow pits instead of pinholes (Supporting Information, Figure D.4). To demonstrate the difference between a "pit" and "pinhole" in the HTL, a picture is shown in Supporting Information, Figure D.5: although the

morphology of the HTL looks similar from a top view, in the cross-section the “pinholes” and “pits” are easy to distinguish. To get the accurate morphological information on HTL and to prevent the FIB process from damaging the sample, two measures were taken into our experiment: (1) Before FIB process, all samples were pre-deposited with a metal protecting layer (Pt or Ir 200 nm and then 2 μm Pt), which can prevent the beam from damaging the top of the HTL. (2) During FIB thinning process, only 5 kV voltage and 7 pA current were applied to the sample when the sample thickness is smaller than 200 nm. This measure can minimize the beam-induced damage to only 10 nm[202].

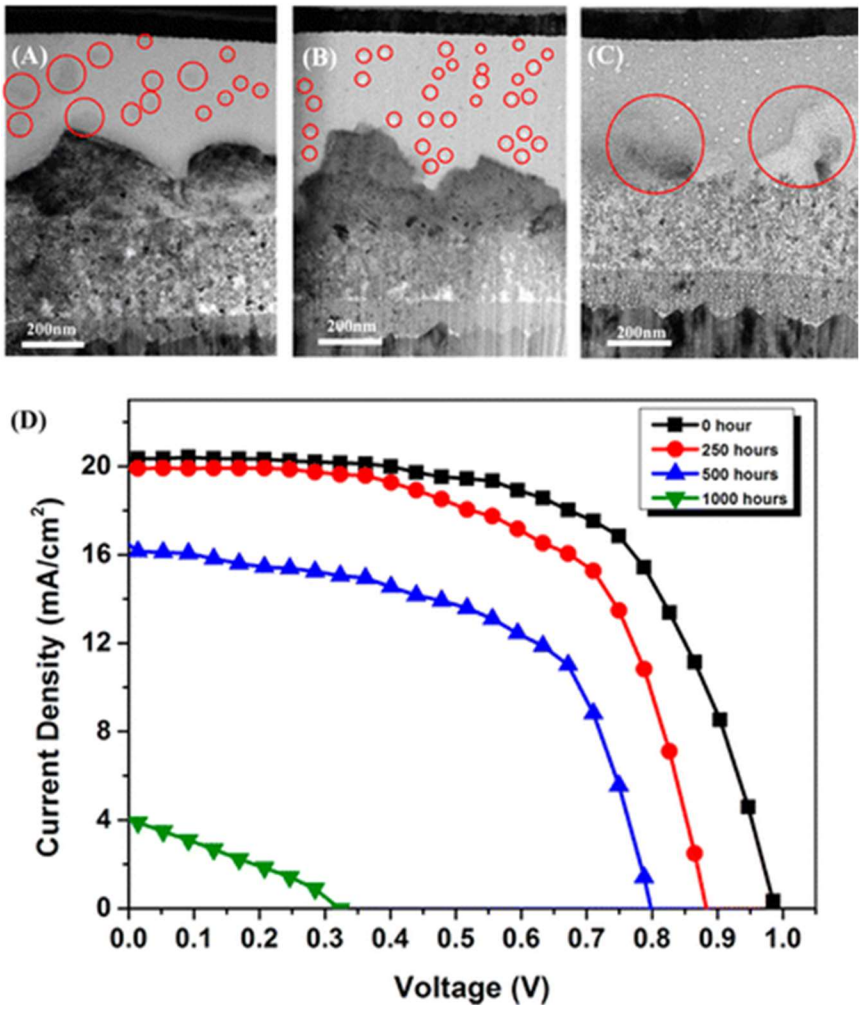

Figure 7.3: BF-TEM cross-section images of the long-term morphological change in the HTL after (a) 200 h storage (inhomogeneous regions in the HTL marked with red circles), (b) 500 h storage (bubble structures in the HTL marked with red circles), and (c) 1000 h storage (degraded perovskite capping layer marked by red circles). (d) *J*–*V* curves of the stored perovskite solar cells. Each curve is the average of 10 cells prepared at the same batch of the TEM sample.

7.4 HTL Morphological Change in PSCs

Apart from our observation of pits on the surface of the HTL (in the absence of tBP), its effect on the stability still needed further investigation. Since the evaporation of tBP can also lead to morphological change of the HTL as mentioned earlier, we suspect this effect exists in a real device and finally influences the

device performance. To study this mechanism, we observe the long-term morphological change of the HTL in an unsealed full PSC. We store the PSC samples under ambient dark conditions with 10% moisture for 1000 h. Four samples for BF-TEM were prepared by FIB on the same cell after different storage times (0, 200, 500, and 1000 h).

As shown in Figure 7.1 (a), at the start, the HTL is homogeneous. As discussed before, that is because tBP promotes miscibility of LiTFSI and Spiro-OMeTAD. After 200 h, as Figure 7.3 (a) displays, inhomogeneous dark regions appear on the HTL. These regions are due to the accumulation of Li salt which occurs due to the loss of tBP by evaporation. Figure 7.3 (b) shows the morphology of the HTL after 500 h. The majority of the dark regions disappear, even as bubble-like structures are generated. This likely occurs because of the hygroscopicity of LiTFSI: moisture can easily react with the accumulated LiTFSI seen in Figure 7.3 (a). The hydration of LiTFSI therefore leads to the bubble structures in the HTL. Finally, in Figure 7.3 (c), after 1000 h, the perovskite has decomposed. These images display that the morphological change, in other words, the failure process of PSCs, is initiated from the HTL instead of the perovskite layer followed by eventual degradation of perovskite. The related photo current density−voltage curves (J−V curves) and device parameters for the stored cells are shown in Figure 7.3 (d) and Table 7.1. Compare with the freshly prepared PSCs (12.6%), the performance decays of the 250 h (10.9%) and 500 h (7.51%) PSCs are not as obvious as the 1000 h PSCs. It is consistent with the TEM results since the

decomposition of the perovskite layer at the first 500 h is limited while at 1000 h, perovskite layer has decomposed.

Table 7.1: Cell Parameters of the Perovskite Solar Cells Stored for 1000 h at 10% Humidity Ambient Dark Conditions

	V_{OC} (V)	J_{SC} (mA/cm^2)	fill factor	efficiency (%)
0 h	0.987	20.38	0.63	12.6
250 h	0.886	19.97	0.62	10.9
500 h	0.799	16.16	0.58	7.51
1000 h	0.331	3.90	0.29	0.38

On the basis of the morphology control effect of tBP on HTL and the failure process of the PSCs, a mechanism regarding the long-term morphological change in a perovskite solar cell is presented now. As displayed in Figure 7.4, at the start (right after device fabrication), the existence of tBP guarantees a uniform HTL, with minimal shallow pits located on the surface the of the HTL. After tBP evaporates, the Li salt accumulates, shown as dark circular regions. These regions are further hydrated to create void structures in the HTL which finally lead to decomposition of the perovskite layer. It should be noted that these events may not strictly proceed one after the other but may instead occur at the same time. During the LiTFSI hydration process, for instance, the decomposition of the perovskite may have already begun since water is already in the HTL.

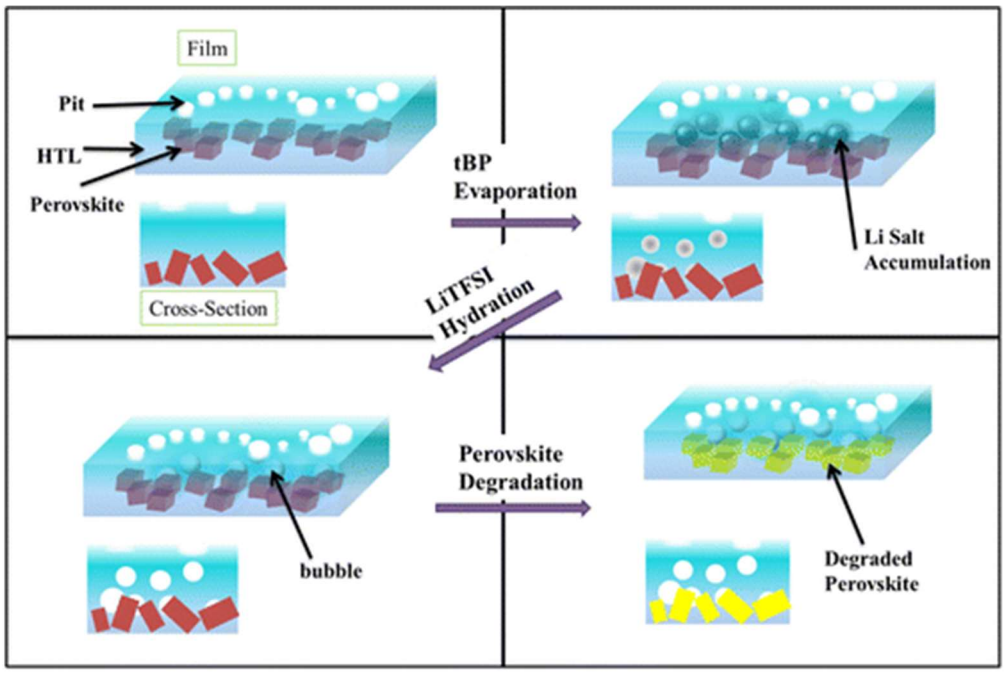

Figure 7.4: Schematic of the morphological change of the HTL/perovskite layers as they are stored in dark conditions.

7.5 Humidity Accumulation Characterizations in PSCs

To further confirm that the lack of tBP can lead to the increasing amount of water in HTL, four fresh-prepared Spiro-OMeTAD films with various components combinations were characterized by Fourier transform infrared spectroscopy (FTIR). As shown in Figure 7.5, films of pure Spiro-OMeTAD (black line), Spiro-OMeTAD/tBP (red line), and Spiro-OMeTAD/tBP/ LiTFSI (dark green line) all display similar peaks. That is because the primary component of the HTL film is Spiro- OMeTAD (in accordance with the weight percentage of the HTL spin-coating solution). However, a water peak is observed in the Spiro-OMeTAD/LiTFSI sample (blue line). This broad peak at ~3600 cm^{-1} corresponds to the O−H stretching mode of water in FTIR. In contrast, no water peak appears in the Spiro-

OMeTAD/tBP/LiTFSI sample (dark green line). This indicates that tBP prevents the accumulation of LiTFSI in Spiro-OMeTAD films, thereby reducing the possibility of LiTFSI hydration since the material is well dispersed throughout the Spiro-OMeTAD and shielded by tBP. The mechanism of how tBP prevents LiTFSI hydration at a chemical level will be the scope of our future work.

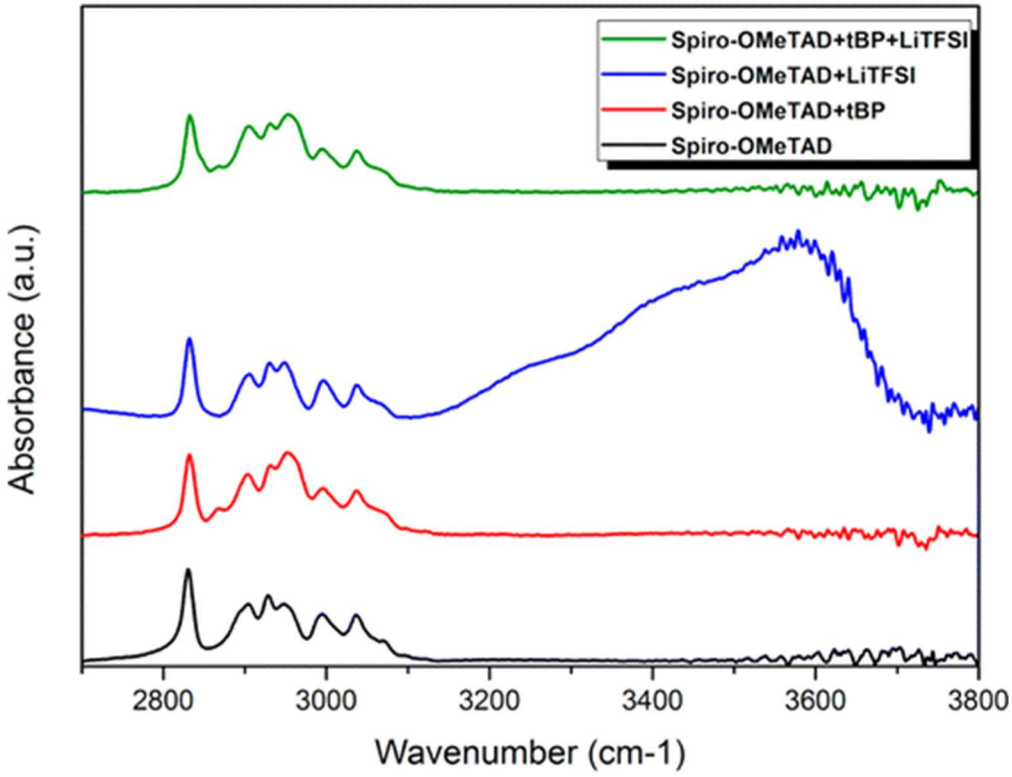

Figure 7.5: FTIR spectra of Spiro-OMeTAD films with various component combinations.

The FTIR study confirmed the presence of moisture in films without tBP, but in order to visualize that moisture truly exists in the HTL for a full cell device structure, we utilized laser-assisted atom probe tomography (APT). With the unique ability of APT to obtain three-dimensional (3D) position information and compositional mapping of energy materials[110,112], we constructed a map of the

water accumulated in PSCs at the HTL/perovskite interface. The PSC devices were stored for over 500 h prior to sample preparation for APT analysis. This corresponds to the morphology of Figure 7.3 (b). In this state, as mentioned before, tBP would evaporate allowing the accumulation of LiTFSI and its possible hydration.

Figure 7.6 (a) displays a perovskite solar cell cross section wedge lifted out for preparing an atom probe needle specimen. Various layers in the device architecture are clearly visible. The annular milling process during final stages of the needle specimen preparation was controlled to retain the HTL layer on the specimen apex and then proceed to the perovskite layer below, with the interface in between. In Figure 7.6 (b), the APT maps show the clear boundary between F (red) and Pb (blue), corresponding to the perovskite/HTL interface. Pb and F maps are used since they are the sole indicators for perovskite and LiTFSI respectively, not present in any other layers. Although fluorine signatures can be obtained from the FTO (fluorine doped tin oxide) layer, atomic positions of F above the Pb region do not conform to the position of the FTO layer. Another caveat is the low analysis temperature used for APT analysis (60 K) which is below the phase transition temperature for the intrinsic perovskite layer. We do not expect that the phase transition would affect the ordering of the layers and the interfaces.

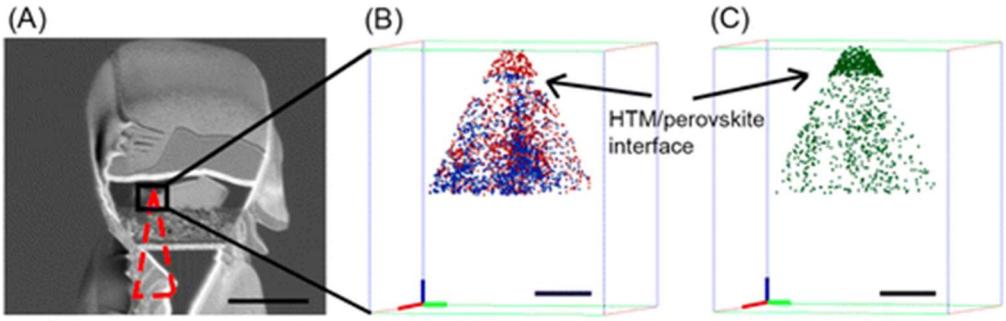

Figure 7.6: 3D APT maps of HTL/perovskite layers after long-term storage (>500 h). (a) SEM image of an APT sample section attached on a Si micropost prior to annular milling by FIB. The red section shows the analysis area. (The scale bar is 1 µm.) (b) 3D elemental maps of Pb (blue dots, from perovskite $CH_3NH_3PbI_3$) and F (red dots, from $TFSI^-$ in HTL). (c) APT map of H_2O showing its distribution in 3D. (Scale bars in b and c are 10 nm. Shown in green is the *x*-axis, red corresponds to the *y*-axis, and blue is the *z*-axis.)

As shown in Figure 7.6 (c), the chemical map for water indicates a strong concentration at the specimen apex region as opposed to the entire region of analysis. To the best of our knowledge, such a strong concentration could not possibly occur from a background signal (see Supporting Information, Figure D.6 for a more quantitative analysis). This region of water accumulation is concurrent with regions of high F concentration. Thus, we conclude that water accumulates in the HTL rather than the perovskite layer.

In comparison to similar chemical maps for F and H_2O, using freshly prepared samples (see Supporting Information, Figure D.7 for more details) with no aging, the total counts for H_2O and F ions are 5 times higher. These observations are also consistent with our TEM results and FT-IR data. In PSCs samples stored in ambient under dark conditions, the amount of tBP in the HTL is

reduced due to its relatively low boiling point and volatile nature. As a result, the HTL prefers to adsorb water due to the hygroscopicity of LiTFSI.

In conclusion, the function of tBP in PSCs was re-evaluated to understand its influence on device stability. Due to the limited penetration depth of HTL into mesoporous TiO_2, it is unlikely that the additive serves only to prevent contact between the Spiro-OMeTAD and TiO_2 layers as traditionally assumed. Based on our observations, tBP functions as a morphological controller for the HTL. It prevents phase separation of LiTFSI and Spiro-OMeTAD during spin-coating of the solution, resulting in a uniform HTL film. The absence of tBP leads to inhomogeneous films and also causes the appearance of large pits on the surface of the HTL. tBP-free HTL easily absorbs water due to the hygroscopicity of accumulated LiTFSI and further lowers the stability of PSCs. In PSCs stored in ambient dark conditions for 1000 h, the slow evaporation of tBP (as it is the only liquid component in PSCs) leads to all of the above-discussed phenomena. Li salt accumulates and generates “dark regions” in the HTL. These dark regions then turn into void bubble structures due to the hydration of Li salt. Finally, the water contained in the HTL contributes to perovskite degradation. Since the evaporation of tBP is a primary contributor to the poor stability of PSCs, we suggest that the performance of PSCs can be enhanced by utilizing other pyridine derivatives that can fulfill the same functions as tBP but have much higher boiling points.

7.6 Acknowledgements

Chapter 7, in full, is a reprint of the material Wang, S., Sina, M., Parikh, P., Uekert, T., Shahbazian, B., Devaraj, A. & Meng, Y. S. Role of 4- *tert* -Butylpyridine as a Hole Transport Layer Morphological Controller in Perovskite Solar Cells. *Nano Letters* **16,** 5594–5600 (2016). The dissertation author was the co-author of this paper. APT measurements and sample preparation were performed by the dissertation author.

Chapter 8 : Summary and Future work

Energy devices have become increasing more complex with the presence of different materials chemistry, dopant distributions, nanoscale coatings and multiple interfaces, whose interactions are not completely understood. To enable the next revolution in green energy, a nanoscale analysis of the individual elements and how they interact is necessary. Changes in the distribution of elements can provide clues on device mechanisms, enhancement in electronic/electrochemical properties and even origins of degradation mechanisms. Hence studying the chemical distribution is an important aspect of the energy challenge that warrants more attention. The focus of my thesis was hence, on overcoming this challenge as it applies to different aspects of green energy, using atom probe tomography (APT) as a primary analysis technique.

APT provides a method to observe the distribution of elements with nanometer spatial resolution and ppm level chemical sensitivity (along with equal detection efficiency for all elements of the periodic table), this fulfilling the requirements to observe and explore a wide range of energy materials. Starting with semiconductor devices (useful for energy management and monitoring systems), the individual finFETs were captured in a single APT specimen tip through careful targeted sample preparation techniques (Chapter 4). This was carried out using focused ion beam. A comparison with conventional STEM-EDX measurement provided better reliability with APT analysis which gave similar results.

Semiconductor devices using silicon was chosen as the first system to work with as similar devices at a larger scale have been explored using APT and it allowed us to create a baseline for the technique and analysis before moving on to relatively unexplored and more challenging, battery cathode and anodes. Following this battery cathodes were explored next (specifically NCA and NCM) to identify the reasons for higher capacity and retention provide by Al. However, in order to obtain accurate composition for all the elements (including Al), a parametric investigation for the cathodes was necessary. It was observed recently for oxide materials that the composition is dependent on the laser energy, with oxygen composition diminishing with higher laser energy.

In Chapter 5, with NCA we observed that a similar trend was seen for O but it was mirrored with Al also. On the other hand, Ni, Co and Li showed a separate trend with a close to accurate composition at 20 pJ as well as cross over point between 0-5pJ. This indicated that the presence of Al (a low evaporation field) element when combined with Ni and Co; both much higher evaporation field elements, provided a complexity in the evaporation behavior such that an accurate stoichiometry for all elements together was not possible at the same laser energy. In contrast, NMC composition, where Ni, Co and Mn have similar evaporation fields allowed better evaporation behavior with a single laser energy where all the elements were close to accurately described.

Based on the contrasting trends of 2 different relevant cathode particles, which would make further cycling analysis more difficult, the attention was focused

on more simpler systems, silicon, used as anode materials for Li-on batteries. As shown in Chapter 6, the lithiation behavior lithiated silicon, essentially an alloy that was far easier to run in APT was investigated. The Li distribution profiles obtained would help to understand the points of maximum strain that causes volume expansion. The challenges here were associated with sample preparation due to the high reactivity of Li to both moisture and to ion beam used for milling. Thus, air free transfer protocols and cryogenic temperatures were used for the sample preparation. Based on the observed results, a lithium distribution profile was observed and presence of residual Li after the first lithiation indicating not only how the lithiation occurs but also how residual Li (possibly in the metallic state) is responsible for the low first cycle coulombic efficiency.

Following this, perovskite solar cells stacks were investigated next, a more challenging system due to the presence of organic layers. However, our success in identifying the pathway for moisture ingress into the devices based on the concurrent F and moisture maps (Chapter 7) indicated that APT can now indeed be used as an application-based instrument to study energy materials.

All these different systems explored in the FIB for sample preparation and in the APT for nanoscale analysis has now given a good set of directions on where the next efforts can be focused. These can be divided into 2 different aspects [a] Continued exploration on more efficient methods for sample preparation for higher tip survivability and [b] novel applications to understand current challenges in batteries.

Towards the former, the next steps would to develop coatings (either Ni itself or oxide-based coatings) that can be deposited on as prepared tips right before deposition. Preliminary Cr based coatings have provided significant success. These coatings should have an evaporation field close to that of Si, on which the specimens are prepared. This would also allow the analysis of complete secondary particles of cathodes from the surface to the bulk which is necessary for degradation of cathodes over cycles. Another avenue would be to explore other final tip preparation methods, apart from FIB, such as etching methods for better control on final tip shape which also affects tip survivability.

On the other end, for novel applications, understanding alloy-based anodes and Li metal anodes, due to their metallic nature is possible with APT. Observing Li distributions in alloy anodes, as well as inorganic products formed on Li metal and Li distributions in dendrites or mossy Li could be enabled next. For electrolytes, the development of solid-state sulfur and oxide-based materials can be studied as they interface with the cathode. A similar parametric investigation (like NCA and NMC) and targeted specimen preparation (like finFETs) would be needed before actual application study to ensure that the effects observed are not an artefact from the instrument.

Moreover, cryogenic techniques developed during the silicon anode study in combination with cryo TEM sample preparation techniques used heavily in the field of biology, can be extended now to liquid electrolyte samples that are freeze

dried to capture the liquid electrolyte-electrode interface and better understand the SEI.

Thus, the field of nanoscale analysis of energy devices, has been sprung wide open now and building on the knowledge for materials, sample targeting and APT analysis developed in this thesis, the next set of challenges can be understood and mechanisms developed more carefully.

Appendix A

Supplementary Information for Chapter 4

Three-dimensional nanoscale mapping of state of the art finFETs

A.1: Atom probe tomography for NMOS- maps for other species

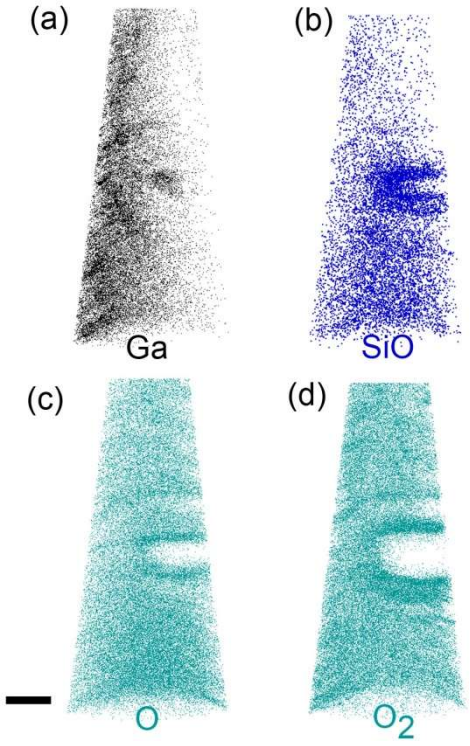

Figure A.1: APT maps of Ga, SiO, O, and O_2 for a NMOS fin. (a) The Ga is from contamination during the ion milling process in the FIB (focused ion beam). The milling conditions used is to ensure that minimum Ga damage occurs during the sample tip preparation. (b) The SiO maps show a higher concentration close to the fin (Figure 4.3 (a)) due to close proximity of Si and O (from the HfO_2 layer). (c, d) The O and O_2 maps are also shown. The O maps show a higher concentration close to the interface of the fin and the HfO_2 dielectric. Scale bar is 25 nm.

A.2: Atom probe tomography for PMOS: maps for other species

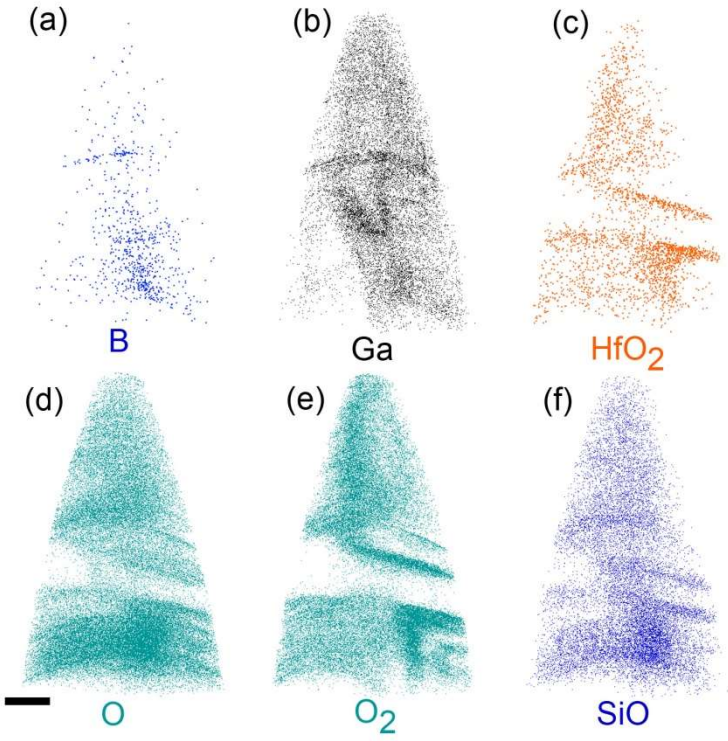

Figure A.2: APT maps of B, Ga, HfO_2, SiO, O and O_2 for a PMOS fin.(a)The B shows a concentration close to the bottom of the map around the same region where the SiO and O signals are present. Boron is present closer to the source/drain contacts indicating the region near the contacts that has been captured in APT. (b) The Ga is from contamination during the ion milling process in the FIB (focused ion beam). (c) The HfO_2 maps are shown here. They mimic the HfO signals (Figure 4.4(a)) both indicating the presence of a HfO_2 dielectric layer. (d, e) The O and O_2 maps are also shown. The O maps show a higher concentration at the bottom of the map between the two HfO walls, which along with the SiO maps (f) indicates the buried oxide layer between fins (Figure 4.1(a). Scale bar is 30 nm.

A.3: Mass spectrum analysis for APT

The mass spectrum for the PMOS and the NMOS maps obtained from APT is shown here. The labels are shown for the most intense peaks. Peaks that could not be identified are also shown with an asterisk. Maps not shown in Figure 4.3

and 4.4 and in Figure A.1 and Figure A.2 have a very low intensity and do not provide any new insights from what can be seen in other maps.

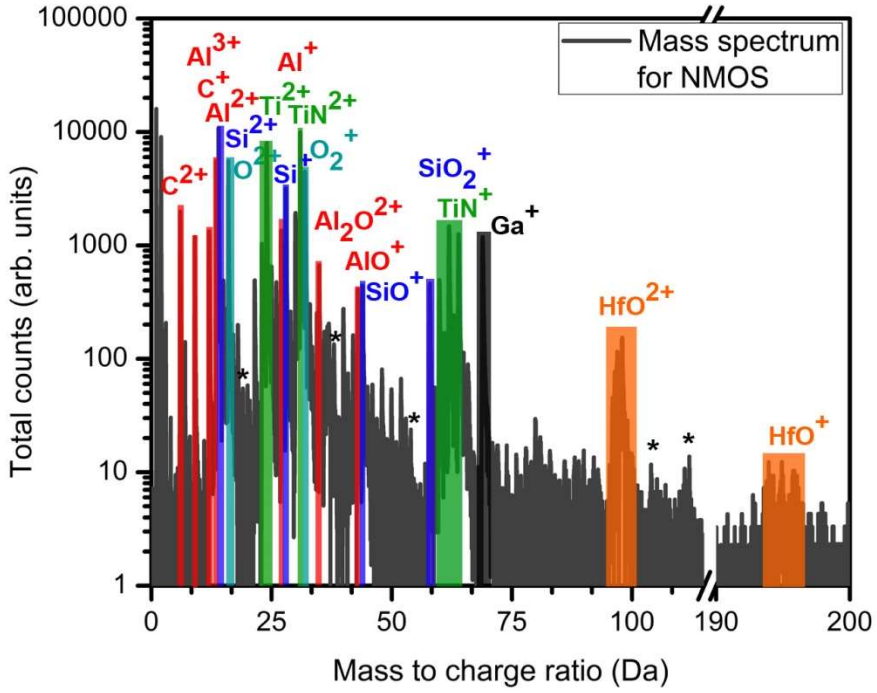

Figure A.3: Major peaks analyzed in the mass spectrum of the NMOS device shown in Figure 4.3. Chemical signatures of Si and all the dielectric layers are present in the mass spectrum.

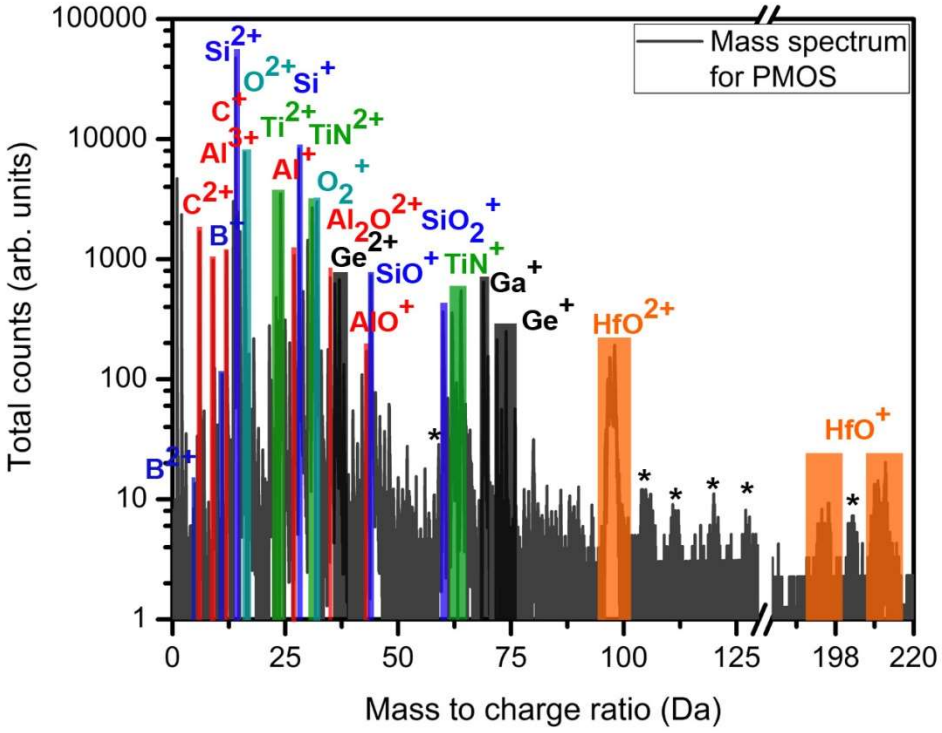

Figure A.4: Major peaks analyzed in the mass spectrum of the PMOS device shown in Figure 4.4. Chemical signatures of Si, Ge and all the dielectric layers are present in the mass spectrum.

A.4: Sample preparation for APT

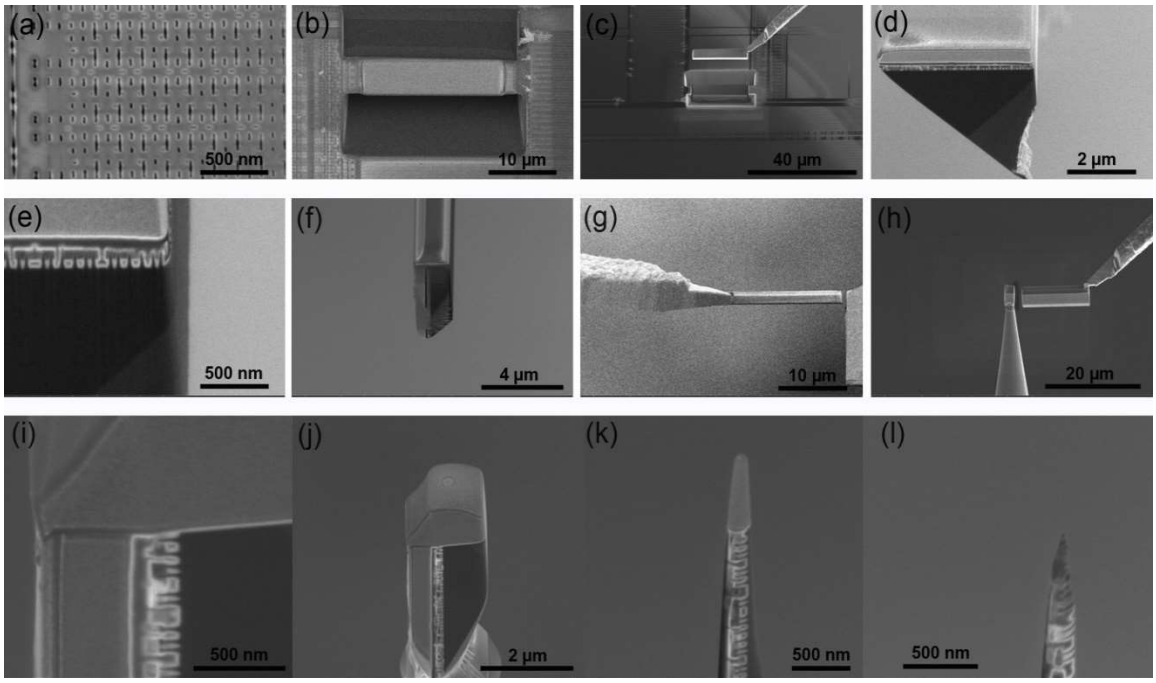

Figure A.5: Cross-section sample preparation process for APT. The region of interest is identified from the SEM images (Figure 4.1 (b)) as seen in (a). A protection coating is deposited and milling trenches are made at an angle of 22° (b). The sample wedge is then picked up using a micromanipulator in situ (c); and the wedge is attached onto the ARM® module. As seen in (e), the right side wall is milled to ensure the transistor of interest is at this wall. The sample is now physically rotated 90° so that the fin of interest faces upwards and another wedge is made such that the fin aligns with the bottom end of the wedge section (f). This section is now picked up using a micromanipulator (g); and smaller sections of it are attached onto a Si microtip array (h). (i) Shows a magnified image of the fin at the apex of the smaller section with protective coatings on two sides and (j) shows one of the smaller sections attached to a microtip array. Annular milling is now carried out to reduce the end radius to less than 200 nm (k); and a final low current, low voltage milling step ensures a conical tip (l).

A.5: Sample preparation for TEM

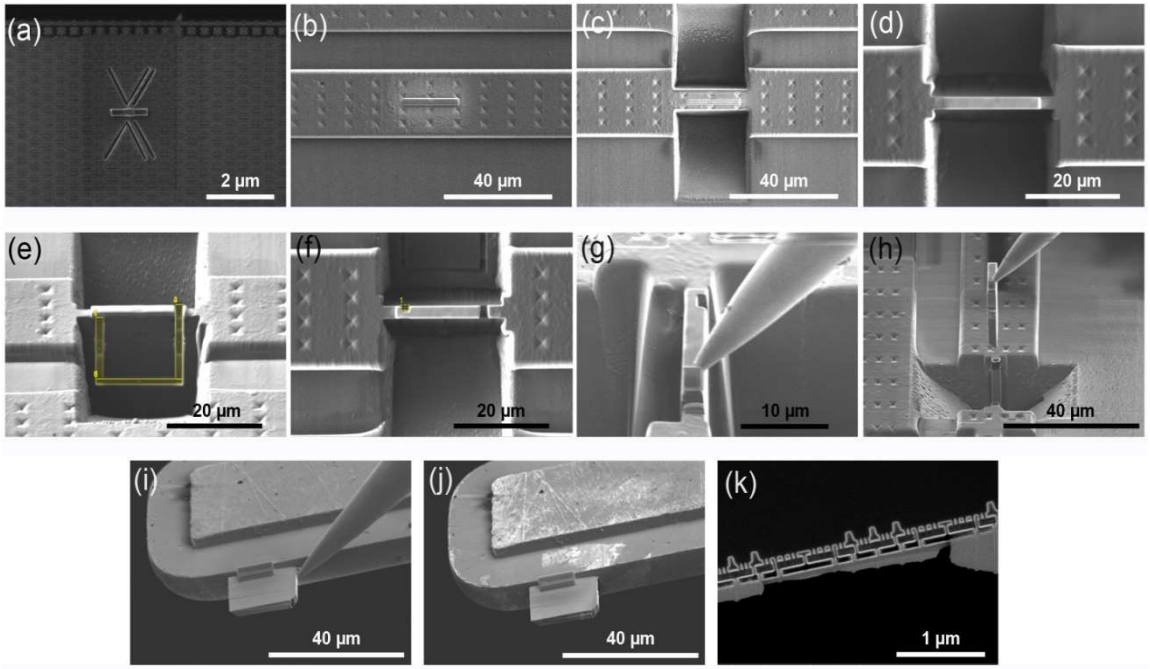

Figure A.6: Sample preparation process for an inverted S/TEM cross-sectional lamella. The region of interest is protected by an e-beam induced deposition, which in addition to lines milled with the FIB column, serve as a fiducial as well, as seen in (a). A larger ion beam induced deposition is placed over the ROI (b). Bulk trenches are milled with the FIB on each side of the lamella as seen in (c). Using a lower ion beam current, the trenches are milled closer to the ROI (d). A “J” shaped pattern is milled with the FIB at 0° stage tilt to nearly free the lamella from the substrate (e). As seen in (f), a small box pattern is milled with the FIB to aid sample release in a subsequent step. The stage is now tilted to 0° and rotated 90° and a micromanipulator is brought in close proximity with the lamella and subsequently welded (g). The sample is then milled completely free from the substrate and the micromanipulator is used to transport the lamella (h). The micromanipulator is rotated 180° (not shown), and the lamella is welded to a TEM grid loaded in a specialized holder (i). The micromanipulator is milled free from the lamella (j) and the holder is manipulated (not shown) so the grid is oriented vertically. Finally, the lamella is thinned using successively lower ion beam accelerating voltages until a damage free lamella of the desired thickness is produced (k).

A.6: STEM-EDS additional maps

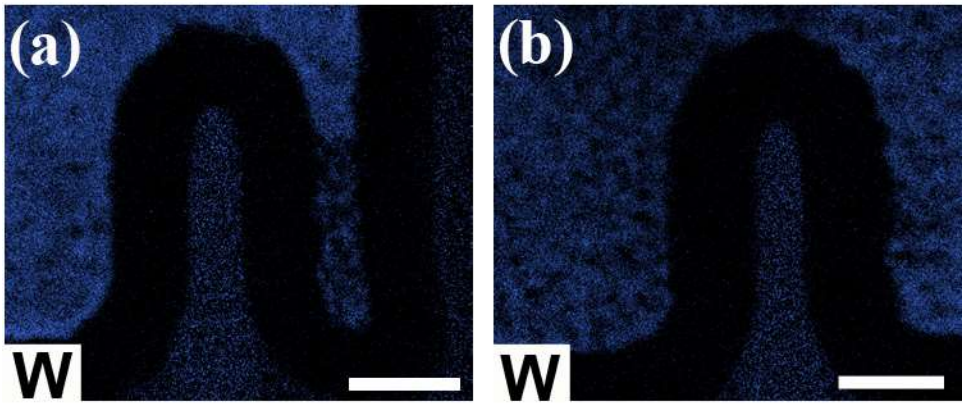

Figure A.7: EDS map of W for (a) NMOS and (b) PMOS fin respectively. Scale bar is 20 nm each.

Appendix B

Supplementary Information for Chapter 5

Compositional quantification of high nickel content NCA and NMC battery oxides using Atom Probe Tomography

Table B.1: Comparison of the atomic composition (in bold) versus the ideal composition for different cathodes analyzed using APT.

System	Atomic composition
$Li_{1.2}Ni_{0.2}Mn_{0.6}O_2$[110]	Li 30% (**41.4%**), Ni 5% (**6.2%**), Mn 15% (**16.6%**), O 50% (**35.7%**)
$LiMn_2O_4$[108]	Li 14% (**22%**), Mn 28.5% (**36%**), O 57% (**41%**)
$LiMn_2O_4$[162]	Li 14% (**25%**), Mn 28.5% (**37%**), O 57% (**38%**)
$LiCoO_2$ (pouch cell prep) [107]	Li 25% (**20%**), Co 25% (**30%**), O 50% (**50%**)
$LiCoO_2$ (thin film) [161]	Li 25% (**28.4%**), Co 25% (**25.8%**), O 50% (**44.2%**)
$Li_{1.2}Mn_{0.55}Ni_{0.15}Co_{0.1}O_2$[111]	Li 25% (**20%**), Co 25% (**30%**), O 50% (**50%**), Mn 13.75% (**15.8%**), Ni 3.75% (**4.4%**)

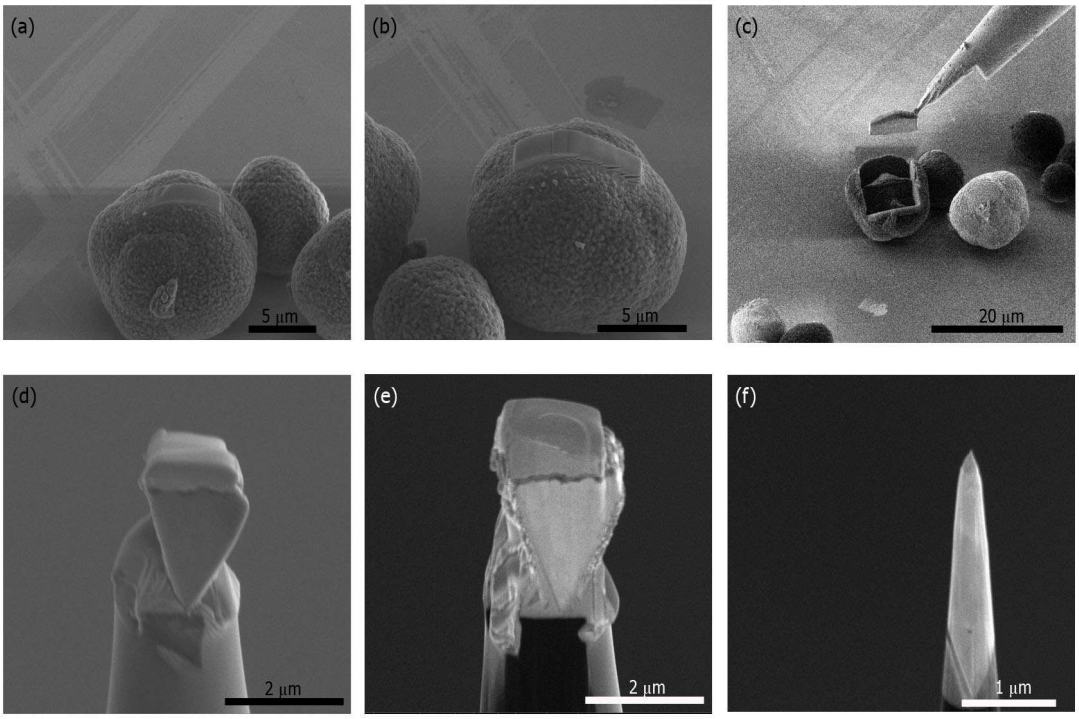

Figure B.1: Specimen tip preparation for NMC811, which is easier using the conventional method of lift-out on the secondary particles itself as opposed to NCA.

Table B.2: Conditions used for the specimen tips analyzed and the output of the fitting for each tip in terms of the FHWM and FWTM (tenth maximum) parameters.

sample	temp	Pulse energy	Pulse rate	Detection rate	Number of ions	FHWM	FHTM	Single events	Multiple events
M2_5743	40	0.5 pJ	100 kHz	0.5	330,000	1023.3	469.1	53.9	44.6
M18_5822	40	0.5 pJ	100 kHz	0.5	806,948	1090	514.6	63.3	35.9
M22_5818	40	0.5 pJ	100 kHz	0.5	1,509,016	1126.6	542.2	65.5	33.7
M15_8373	40	1 pJ	100 kHz	0.5	442,186	1036.8	465.6	67.3	31.6
M17_8387	40	1 pJ	100 kHz	0.5	1,426,880	1150.4	535.2	67.7	31.6
M19_8389	40	5 pJ	100 kHz	0.4	625,382	537.3	138.5	69.2	29.9
M13_8371	40	10 pJ	100 kHz	0.5	948,928	658.4	121.3	64.4	34.9
M11_7564	40	20 pJ	100 kHz	0.3	697,229	264.5	93.9	71.4	27.7
New data									
M22_8439	40	20 pJ	100kHz	0.5	970,506	412.9	116.2	69.3	29.8
M21_8433	40	5 pJ	100 kHz	0.5	463,048	630.8	168.4	61.1	37.8
M2_8341 (low energy milling)	40	1 pJ	100 kHz	0.5	849743	1127.3	519.8	62.8	36.4
M3_8430	40	20 to 5 pJ transition	100 kHz	0.5	1,475,349	480.6	163.1	67.9	31.3

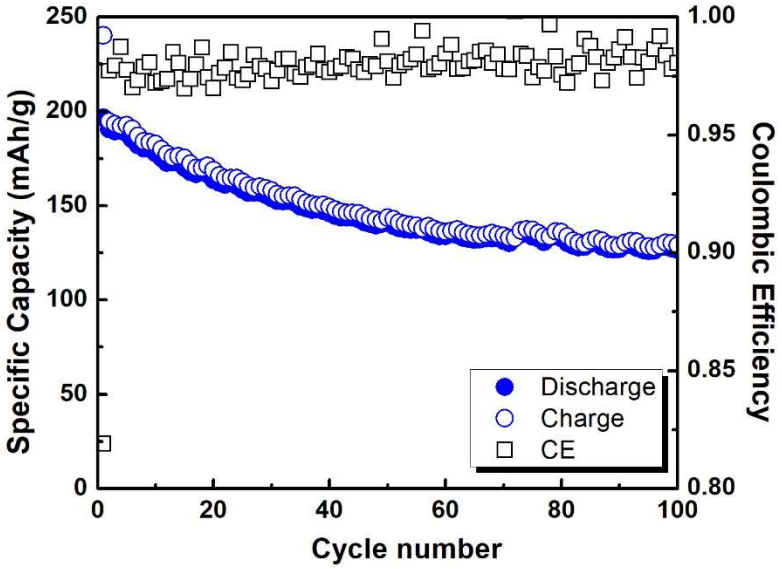

Figure B.2: Specific capacity and Coulombic Efficiency over 100 cycles for the NCA electrodes used for this study.

Appendix C

Supplementary Information for Chapter 6

Direct observation of Li during first cycle lithiation of silicon anodes

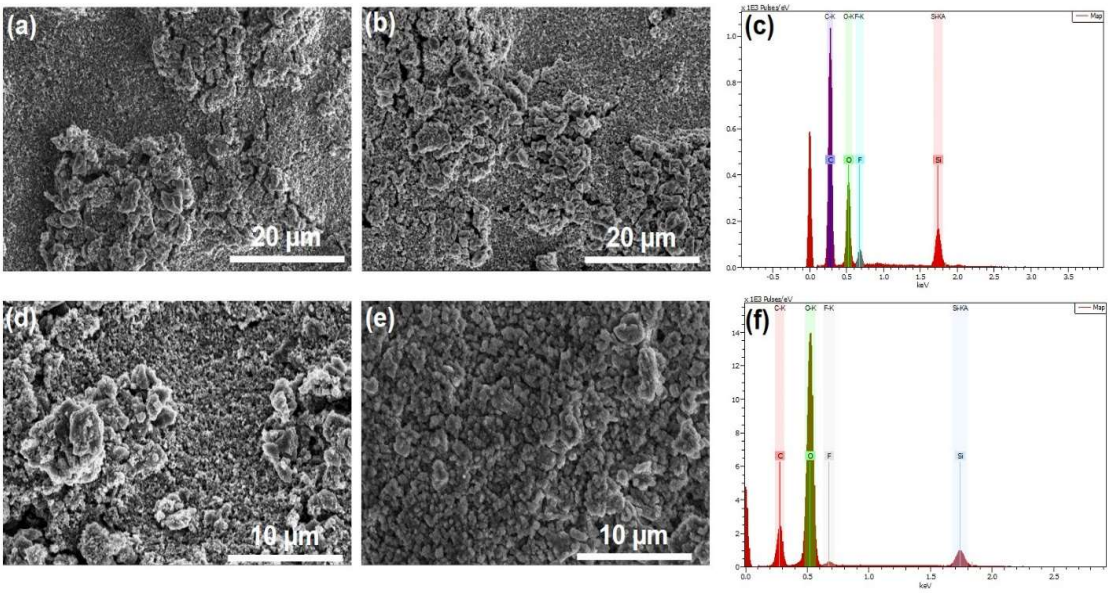

Figure C.1: Comparison of the SEM images (at 50 mV) when the correct drying protocols were followed (a) before and (b) after and (c) EDX pattern corresponding to (c), showing a small oxygen content. With residual moisture in the carbon tape, the morphology can change drastically, (d) before and (e) after and (f) EDX spectrum showing the increase in the oxygen content for the SEM image shown in (e).

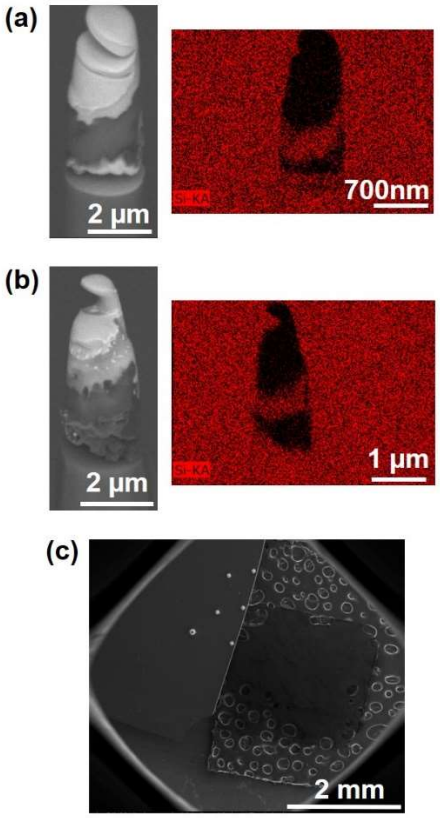

Figure C.2: Comparison of the morphology of the silicon anodes without (a) and with (b) cryogenic milling showing no differences. However, any changes in Li cannot be observed at this scale. (c) Movement of the microtip array due to hardening (brittleness) of the adhesive at cryo temperatures.

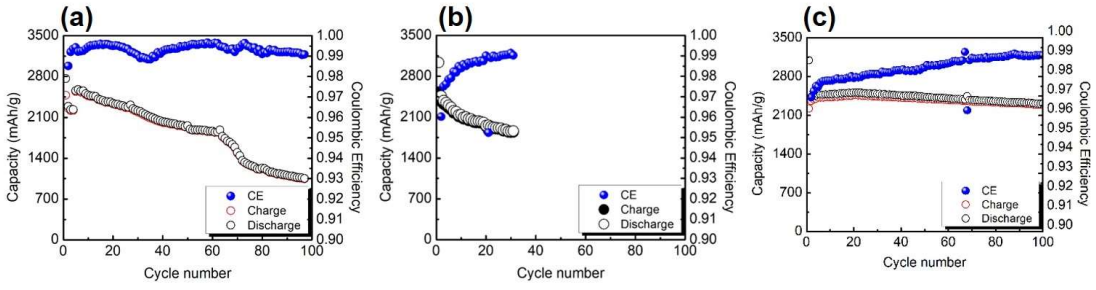

Figure C.3: Capacity retention of micro-silicon with PAA binder (a), CMC-PAA copolymer binder (b) and nano-silicon with PAA binder (c), all in half cell configuration. The micro-silicon cells are at a loading of 1 mg/cm^2 and nano-silicon at 0.5 mg/cm^2.

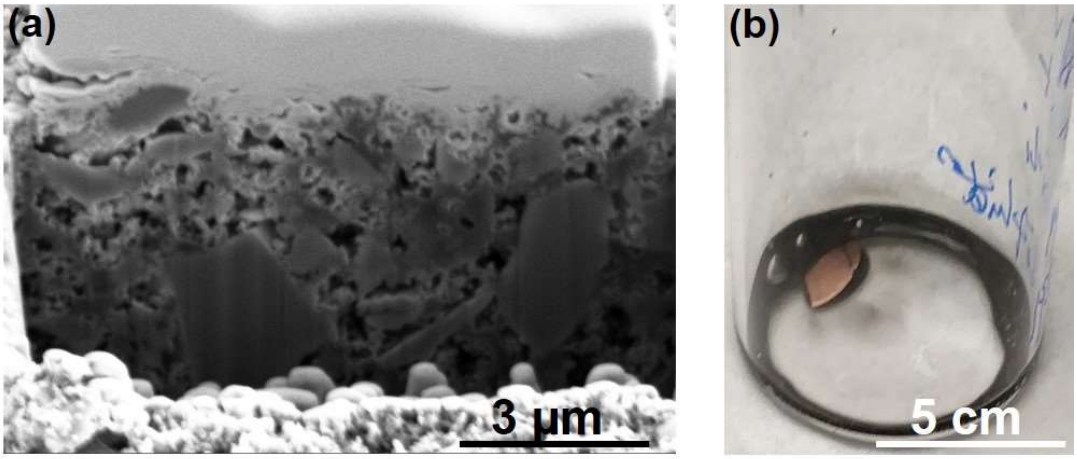

Figure C.4: (a) Porous morphology of the micrometer sized silicon anode making regular liftout and APT analysis a challenging task and (b) Electrode dissolution (with bubbling) within seconds using 50 µl deionized water.

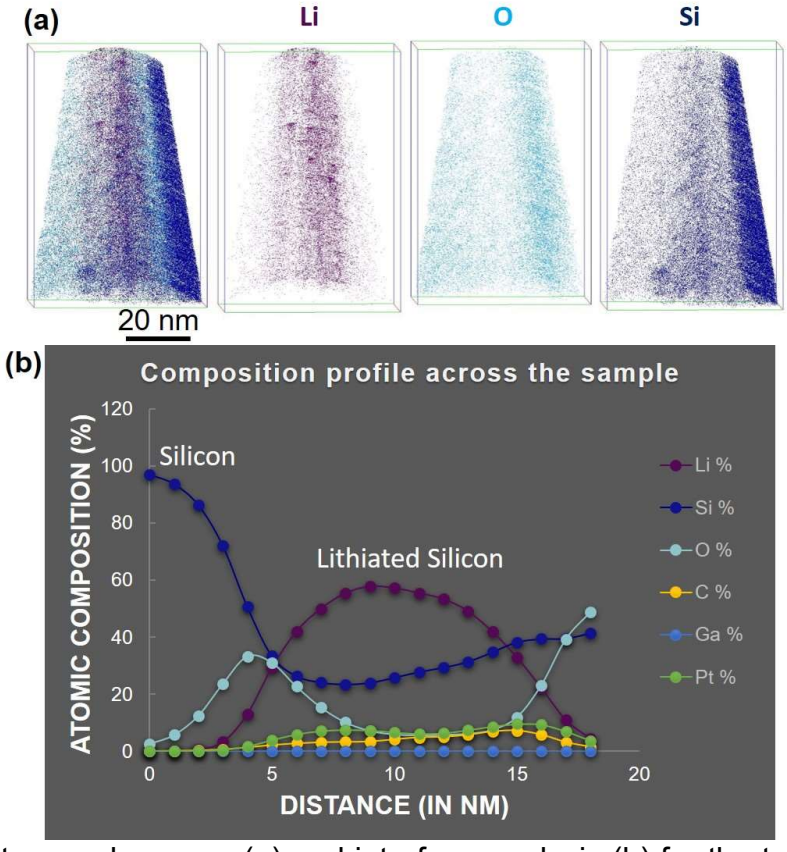

Figure C.5: Atom probe maps (a) and interface analysis (b) for the test sample at 50 mV.

Table C.1: Atomic Composition for each element (for specimen tip at 50 mV lithiation) obtained from the mass spectrum analysis using IVAS software.

	Atomic composition (%)
Li	25
Si	45.7
O	1.5
Ga	0.06
Pt	2
C	20
F	4
P	0.6

Appendix D

Supplementary Information for Chapter 7

Role of 4-tert-Butylpyridine as a Hole Transport Layer Morphological Controller in Perovskite Solar Cells

D.1 Methods

All reagents, unless otherwise stated, were purchased from Sigma-Aldrich. *Methylammonium iodide (MAI) synthesis*: 15 mL of 33 wt% methylamine solution in anhydrous methanol was reacted with 15 mL of 57 wt% hydroiodic acid in a flask for 1 hour. After evaporating all solvents, the mixture was dissolved in anhydrous ethanol. Ethyl ether was used to precipitate MAI from the solution. The MAI was dried overnight in a vacuum oven, and a white crystalline powder was obtained as the final product.

Perovskite solar cells (PSCs) fabrication: PSC fabrication was based on the sequential deposition method[171]. A TiO_2 compact layer was spin-coated on cleaned FTO glass. After sintering, a mesoporous TiO_2 layer was spin-coated onto the TiO_2 compact layer and sintered again. PbI_2 (Alfa Aesar) was dissolved in dimethyl formamide and spin-coated onto mesoporous TiO_2. Then the films were dipped in MAI solution (isopropanol as the solvent). After thermal annealing, the films were spin-coated with a solution containing Spiro-OMeTAD (Merck), tBP, and LiTFSI which were dissolved in chlorobenzene. Finally, 80 nm of gold was evaporated onto the films. For more detailed information (spin-coating speed/time, solution concentration, and annealing condition)[195].

Characterization:

Scanning Electronic Microscopy (SEM) images were taken with a FEI SFEG UHR SEM operated at 10kV. Samples were coated with iridium before taking SEM images to avoid beam drift for semiconducting and insulating materials.

Transmission electron microscopy (TEM) images were taken with a FEI 200kV Sphera Microscope. Samples for TEM were prepared by focused ion beam (FEI Scios DualBeam FIB/SEM). Regions of interest were deposited with 2 um thick Pt for protection during ion etching. After etching from the substrate, the samples were lifted by a tungsten needle (FEI EasyLift LT NanoManipulator). Before disconnecting the sample from the needle, samples were attached onto the FIB lift-out grid (Copper PELCO FIB Lift-Out Grid). Subsequently samples attached onto the lift-out grid were thinned to within 100 nm by a Ga^{2+} ion beam. In addition, the EFTEM images and EELS spectra were acquired using a Gatan Enfina spectrometer with a collection angle of 52 mrad and convergence angle of 30 mrad.

Samples for atom probe tomography (APT) were prepared and analyzed at the Environmental and Molecular Sciences Laboratory at PNNL. In brief samples were prepared from fabricated PSC devices, in the form of tips, using FEI Helios dual-beam focused ion beam/scanning electron microscope (FIB/SEM) equipped with an Omniprobe. A wedge-shaped lift-out section was prepared by milling at 22 degrees. The liftout section was controlled using an in-situ micromanipulator

(Omniprobe) and 2 μm sections were cut and affixed on a Si microtip array followed by Pt deposition on either side to hold the wedge in place. An annular milling pattern with progressively smaller diameter was used to get the shape of a tip. A final low beam energy (~ 2kV) exposure was used to give the tip its final shape as well as remove surface regions, which are prone to maximum Ga damage. The end radius at the tip was less than 100 nm.

As prepared sample tips were then analyzed using a LEAP (local electrode atom probe) 4000XHR with a detector efficiency of ~40%. A temperature of 60 K and laser energy (~ 100 pJ) was used to ensure field evaporation of ions in a regular manner. The laser energy, detection rate and temperature were optimized for our samples. The reconstruction to obtain the 3-D maps and the analysis were done using the IVAS® software.

Fourier transform infrared spectroscopy (FTIR) with attenuated total reflectance (ATR) attachment (Nicolet 6700 with Smart-iTR) was applied for the FTIR test. Samples for FTIR were spin-coated on CaF2 substrates at 2000 r.p.m. and 30 s as thin films.

D.2 Supplementary Data

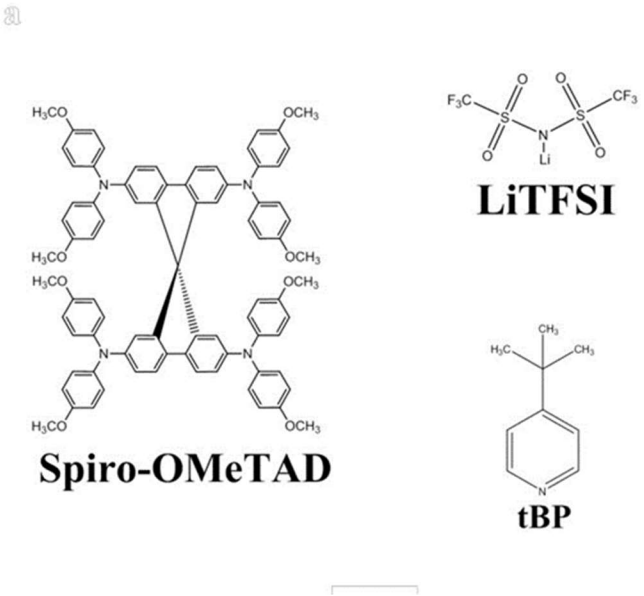

Figure D.1: Molecular Structures of the components in the HTL for PSCs: Spiro-OMeTAD, LiTFSI and tBP.

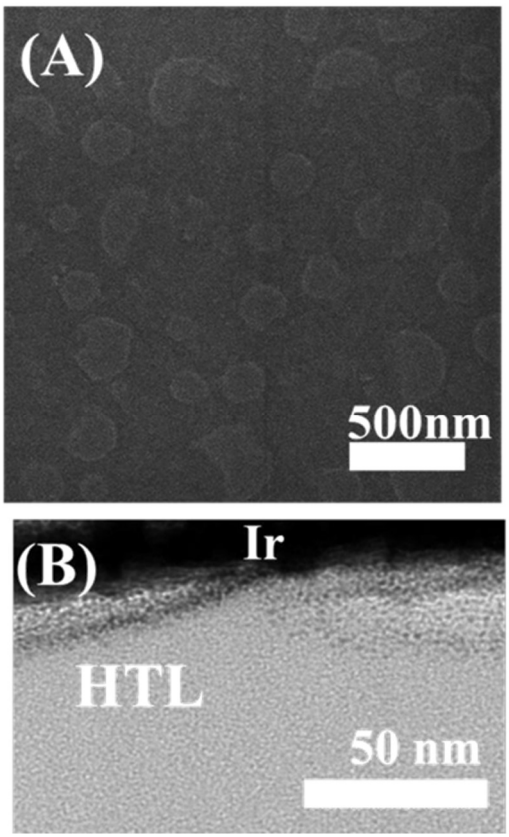

Figure D.2: (a) Top-view SEM images of the freshly prepared HTL with tBP after thermal annealing treatment. (b) Cross-section BF-TEM images of the freshly prepared HTL with tBP after thermal annealing treatment.

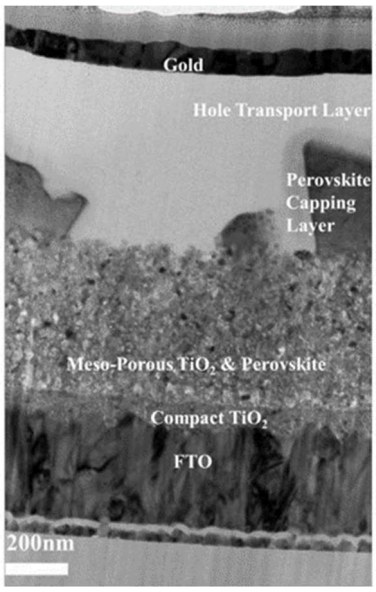

Figure D.3: Cross-section BF-TEM image of a PSC, which indicates that the HTL has a homogeneous morphology. The sample was intentionally prepared with less perovskite coverage in order to display more HTL area.

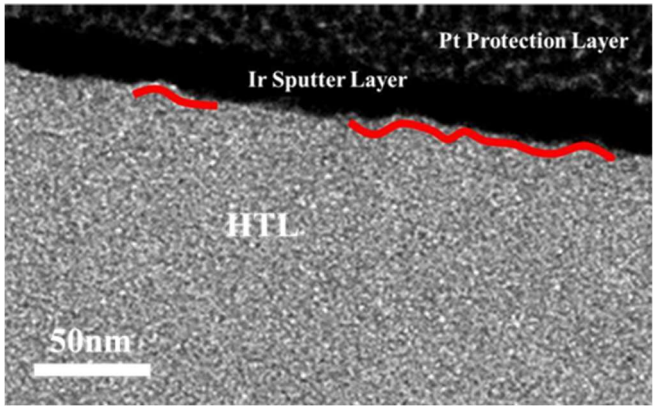

Figure D.4: Cross-section BF-TEM image of the HTL with a metal capping layer. It reveals the curved structure of the HTL/metal interface. The red line marks the curved portions of the interface. The sample was prepared by FIB.

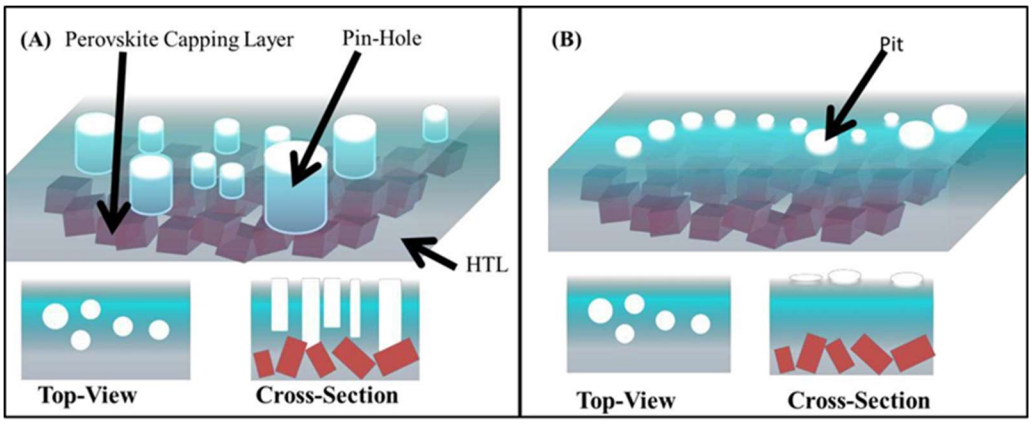

Figure D.5: Schematic of the HTL with a perovskite capping layer (a) pin-hole model; (b) pit model. They have similar top-view morphology, but the cross-section morphology is clearly distinguishable.

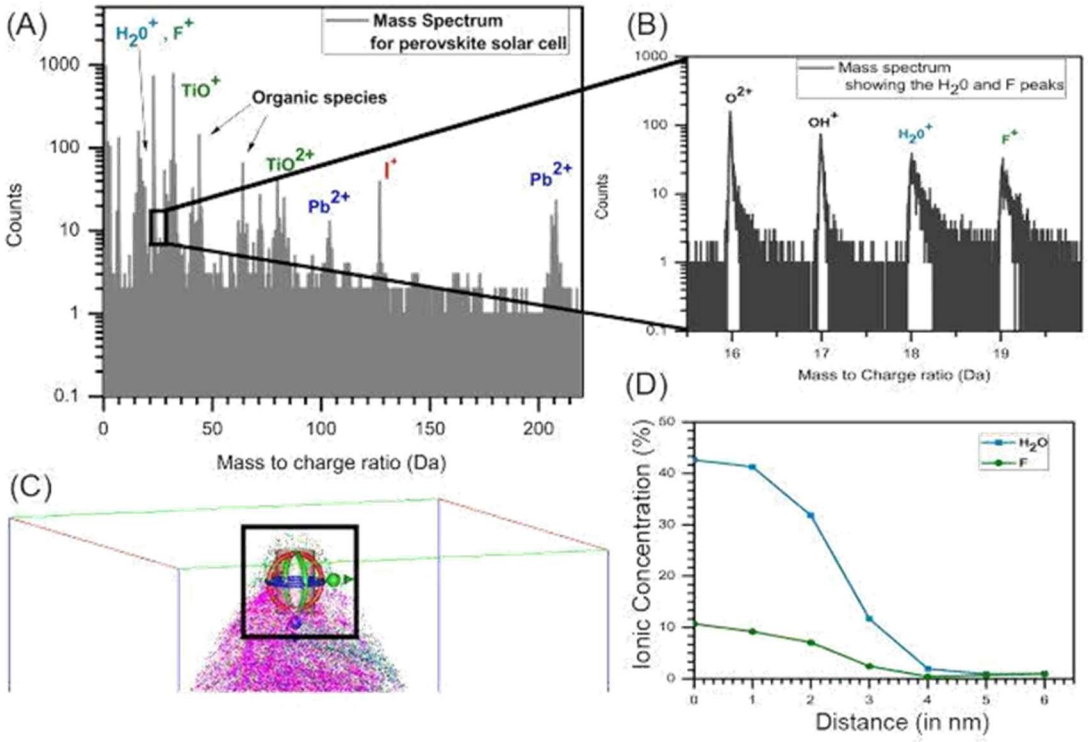

Figure D.6: Additional analysis for atom probe tomography performed on perovskite solar cells. (a) Shows the mass spectrum for the analysis region shown in Figure 7 main text. (b) Zoom in of the mass spectrum for the region marked by the black box in (a). The peak for H2O is clearly visible. The high intensity of this peak does not fit the isotopic ratios as expected for O^{2+}. (c) The analysis region (marked by the black box) for the 1-D concentration profile. (d) 1-D concentration profile showing the decrease in F and H_2O species across the interface.

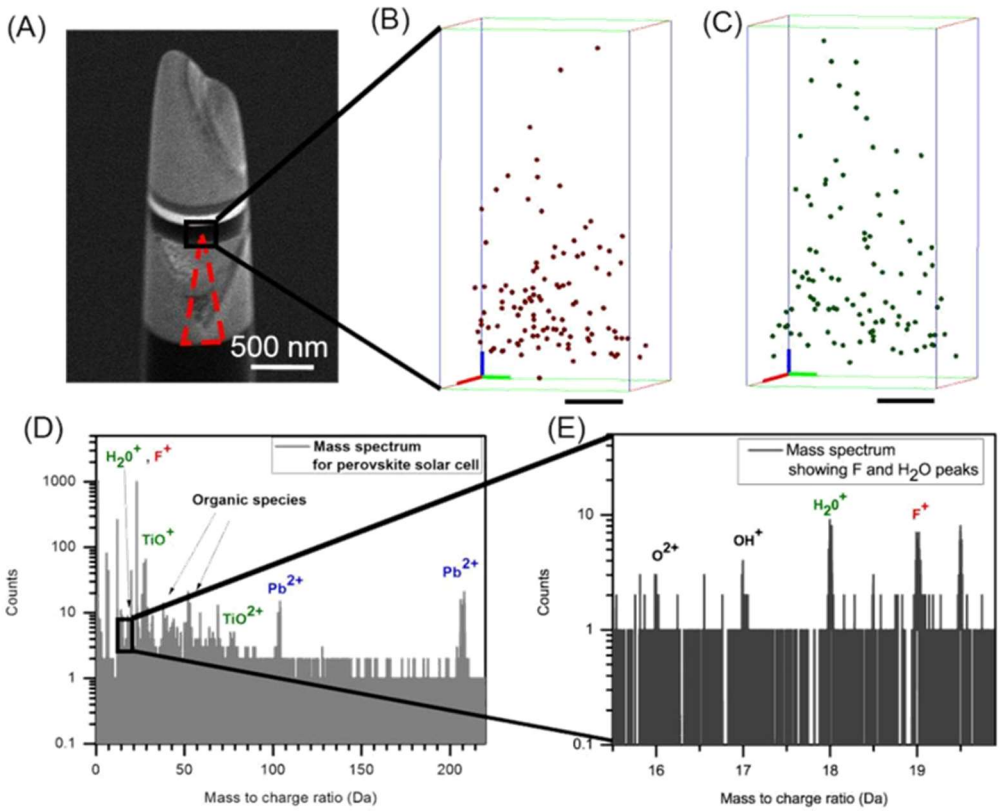

Figure D.7: Analysis for atom probe tomography performed on freshly prepared perovskite solar cells (cells that were prepared into tips and analyzed right after device preparation to prevent influence of moisture). (a) Shows the SEM image for the analysis region with tip going from the hole transport layer into the perovskite layer. (b) APT map of F (fluorine) showing its distribution in 3D (c) APT map of H_2O showing its distribution in 3D. (Scale bar in (b) and (c) are 8 nm. Shown in green is the x-axis, red corresponds to the y-axis and blue is the z-axis.) (d) Shows the mass spectrum for the analysis region shown in (a). (e) Zoom in of the mass spectrum for the region marked by the black box in (d). The peak for H_2O is clearly visible. The high intensity of this peak does not fit the isotopic ratios as expected for O^{2+}. In comparison to Figure D.6 (b) the maximum ionic count for both F and H_2O are 5 times lower in the freshly prepared sample, validating the role of tBP both as an agent to improve miscibility and reduce the moisture content of the hole transport layer.

References

1. Whittingham, M. S. Lithium Batteries and Cathode Materials. *Chem. Rev.* **104,** 4271–4302 (2004).

2. Ellis, B. L., Lee, K. T. & Nazar, L. F. Positive Electrode Materials for Li-Ion and Li-Batteries. *Chem. Mater.* **22,** 691–714 (2010).

3. Nitta, N., Wu, F., Lee, J. T. & Yushin, G. Li-ion battery materials: present and future. *Mater. Today* **18,** 252–264 (2015).

4. Zhang, W.-J. A review of the electrochemical performance of alloy anodes for lithium-ion batteries. *J. Power Sources* **196,** 13–24 (2011).

5. Liu, W., Oh, P., Liu, X., Lee, M.-J., Cho, W., Chae, S., Kim, Y. & Cho, J. Nickel-rich layered lithium transition-metal oxide for high-energy lithium-ion batteries. *Angew. Chem. Int. Ed Engl.* **54,** 4440–4457 (2015).

6. Goriparti, S., Miele, E., De Angelis, F., Di Fabrizio, E., Proietti Zaccaria, R. & Capiglia, C. Review on recent progress of nanostructured anode materials for Li-ion batteries. *J. Power Sources* **257,** 421–443 (2014).

7. Armstrong, R. C., Wolfram, C., de Jong, K. P., Gross, R., Lewis, N. S., Boardman, B., Ragauskas, A. J., Ehrhardt-Martinez, K., Crabtree, G. & Ramana, M. V. The frontiers of energy. *Nat. Energy* **1,** 15020 (2016).

8. Perez, R. & Perez, M. A FUNDAMENTAL LOOK AT ENERGY RESERVES FOR THE PLANET (2009).

9. Best Research-Cell Efficiency Chart | Photovoltaic Research | NREL. at <https://www.nrel.gov/pv/cell-efficiency.html>

10. Shockley, W. & Queisser, H. J. Detailed Balance Limit of Efficiency of p-n Junction Solar Cells. *J. Appl. Phys.* **32,** 510–519 (1961).

11. Solar Thermal Power Plants - Energy Explained, Your Guide To Understanding Energy - Energy Information Administration. at <https://www.eia.gov/energyexplained/?page=solar_thermal_power_plants>

12. Light Generated Current | PVEducation. at <https://www.pveducation.org/pvcdrom/solar-cell-operation/light-generated-current>

13. Hersch, P., Zweibel, K. & Institute, S. E. R. Basic Photovoltaic Principles and Methods. 71

14. Battaglia, C., Cuevas, A. & Wolf, S. D. High-efficiency crystalline silicon solar cells: status and perspectives. *Energy Environ. Sci.* **9,** 1552–1576 (2016).

15. Shah, A., Torres, P., Tscharner, R., Wyrsch, N. & Keppner, H. Photovoltaic Technology: The Case for Thin-Film Solar Cells. *Science* **285,** 692–698 (1999).

16. Kojima, A., Teshima, K., Shirai, Y. & Miyasaka, T. Organometal Halide Perovskites as Visible-Light Sensitizers for Photovoltaic Cells. *J. Am. Chem. Soc.* **131,** 6050–6051 (2009).

17. Green, M. A., Ho-Baillie, A. & Snaith, H. J. The emergence of perovskite solar cells. *Nat. Photonics* **8,** 506–514 (2014).

18. Grätzel, M. The light and shade of perovskite solar cells. *Nat. Mater.* **13,** 838–842 (2014).

19. Yin, W.-J., Yang, J.-H., Kang, J., Yan, Y. & Wei, S.-H. Halide perovskite materials for solar cells: a theoretical review. *J. Mater. Chem. A* **3,** 8926–8942 (2015).

20. Matsui, T., Yamamoto, T., Nishihara, T., Morisawa, R., Yokoyama, T., Sekiguchi, T. & Negami, T. Compositional Engineering for Thermally Stable, Highly Efficient Perovskite Solar Cells Exceeding 20% Power Conversion Efficiency with 85 °C/85% 1000 h Stability. *Adv. Mater.* **31,** 1806823 (2019).

21. Zhao, D., Wang, C., Song, Z., Yu, Y., Chen, C., Zhao, X., Zhu, K. & Yan, Y. Four-Terminal All-Perovskite Tandem Solar Cells Achieving Power Conversion Efficiencies Exceeding 23%. *ACS Energy Lett.* **3,** 305–306 (2018).

22. Jiang, Q., Zhao, Y., Zhang, X., Yang, X., Chen, Y., Chu, Z., Ye, Q., Li, X., Yin, Z. & You, J. Surface passivation of perovskite film for efficient solar cells. *Nat. Photonics* **13,** 460 (2019).

23. Tong, J., Song, Z., Kim, D. H., Chen, X., Chen, C., Palmstrom, A. F., Ndione, P. F., Reese, M. O., Dunfield, S. P., Reid, O. G., Liu, J., Zhang, F., Harvey, S. P., Li, Z., Christensen, S. T., Teeter, G., Zhao, D., Al-Jassim, M. M., Hest, M. F. A. M. van, Beard, M. C., Shaheen, S. E., Berry, J. J., Yan, Y. & Zhu, K. Carrier lifetimes of >1 μs in Sn-Pb perovskites enable efficient all-perovskite tandem solar cells. *Science* **364,** 475–479 (2019).

24. Jung, E. H., Jeon, N. J., Park, E. Y., Moon, C. S., Shin, T. J., Yang, T.-Y., Noh, J. H. & Seo, J. Efficient, stable and scalable perovskite solar cells using poly(3-hexylthiophene). *Nature* **567,** 511 (2019).

25. Gonzalez-Pedro, V., Juarez-Perez, E. J., Arsyad, W.-S., Barea, E. M., Fabregat-Santiago, F., Mora-Sero, I. & Bisquert, J. General Working Principles of CH3NH3PbX3 Perovskite Solar Cells. *Nano Lett.* **14,** 888–893 (2014).

26. Marchioro, A., Teuscher, J., Friedrich, D., Kunst, M., van de Krol, R., Moehl, T., Grätzel, M. & Moser, J.-E. Unravelling the mechanism of photoinduced charge transfer processes in lead iodide perovskite solar cells. *Nat. Photonics* **8,** 250–255 (2014).

27. Yang, G., Tao, H., Qin, P., Ke, W. & Fang, G. Recent progress in electron transport layers for efficient perovskite solar cells. *J. Mater. Chem. A* **4,** 3970–3990 (2016).

28. Mahmood, K., Sarwar, S. & Mehran, M. T. Current status of electron transport layers in perovskite solar cells: materials and properties. *RSC Adv.* **7,** 17044–17062 (2017).

29. Ke, W., Fang, G., Liu, Q., Xiong, L., Qin, P., Tao, H., Wang, J., Lei, H., Li, B., Wan, J., Yang, G. & Yan, Y. Low-Temperature Solution-Processed Tin Oxide as an Alternative Electron Transporting Layer for Efficient Perovskite Solar Cells. *J. Am. Chem. Soc.* **137,** 6730–6733 (2015).

30. Calió, L., Kazim, S., Grätzel, M. & Ahmad, S. Hole-Transport Materials for Perovskite Solar Cells. *Angew. Chem. Int. Ed.* **55,** 14522–14545 (2016).

31. Chen, Q., Zhou, H., Hong, Z., Luo, S., Duan, H.-S., Wang, H.-H., Liu, Y., Li, G. & Yang, Y. Planar Heterojunction Perovskite Solar Cells via Vapor-Assisted Solution Process. *J. Am. Chem. Soc.* **136,** 622–625 (2014).

32. Salim, T., Sun, S., Abe, Y., Krishna, A., C. Grimsdale, A. & Ming Lam, Y. Perovskite-based solar cells: impact of morphology and device architecture on device performance. *J. Mater. Chem. A* **3,** 8943–8969 (2015).

33. Wang, Z., Shi, Z., Li, T., Chen, Y. & Huang, W. Stability of Perovskite Solar Cells: A Prospective on the Substitution of the A Cation and X Anion. *Angew. Chem. Int. Ed.* **56,** 1190–1212 (2017).

34. Wang, R., Mujahid, M., Duan, Y., Wang, Z.-K., Xue, J. & Yang, Y. A Review of Perovskites Solar Cell Stability. *Adv. Funct. Mater.* **0,** 1808843

35. Brenner, T. M., Rakita, Y., Orr, Y., Klein, E., Feldman, I., Elbaum, M., Cahen, D. & Hodes, G. Conversion of Single Crystalline PbI2 to CH3NH3PbI3: Structural Relations and Transformation Dynamics. *Chem. Mater.* **28,** 6501–6510 (2016).

36. Jang, D. M., Park, K., Kim, D. H., Park, J., Shojaei, F., Kang, H. S., Ahn, J.-P., Lee, J. W. & Song, J. K. Reversible Halide Exchange Reaction of Organometal Trihalide Perovskite Colloidal Nanocrystals for Full-Range Band Gap Tuning. *Nano Lett.* **15,** 5191–5199 (2015).

37. Eperon, G. E., Habisreutinger, S. N., Leijtens, T., Bruijnaers, B. J., van Franeker, J. J., deQuilettes, D. W., Pathak, S., Sutton, R. J., Grancini, G., Ginger, D. S., Janssen, R. A. J., Petrozza, A. & Snaith, H. J. The Importance of Moisture in Hybrid Lead Halide Perovskite Thin Film Fabrication. *ACS Nano* **9,** 9380–9393 (2015).

38. Ko, H.-S., Lee, J.-W. & Park, N.-G. 15.76% efficiency perovskite solar cells prepared under high relative humidity: importance of PbI 2 morphology in two-step deposition of CH 3 NH 3 PbI 3. *J. Mater. Chem. A* **3,** 8808–8815 (2015).

39. Gao, H., Bao, C., Li, F., Yu, T., Yang, J., Zhu, W., Zhou, X., Fu, G. & Zou, Z. Nucleation and Crystal Growth of Organic–Inorganic Lead Halide Perovskites under Different Relative Humidity. *ACS Appl. Mater. Interfaces* **7,** 9110–9117 (2015).

40. Han, Y., Meyer, S., Dkhissi, Y., Weber, K., M. Pringle, J., Bach, U., Spiccia, L. & Cheng, Y.-B. Degradation observations of encapsulated planar CH 3 NH 3 PbI 3 perovskite solar cells at high temperatures and humidity. *J. Mater. Chem. A* **3,** 8139–8147 (2015).

41. Yang, J., Siempelkamp, B. D., Liu, D. & Kelly, T. L. Investigation of CH3NH3PbI3 Degradation Rates and Mechanisms in Controlled Humidity Environments Using in Situ Techniques. *ACS Nano* **9,** 1955–1963 (2015).

42. Frost, J. M., Butler, K. T., Brivio, F., Hendon, C. H., van Schilfgaarde, M. & Walsh, A. Atomistic Origins of High-Performance in Hybrid Halide Perovskite Solar Cells. *Nano Lett.* **14,** 2584–2590 (2014).

43. Leguy, A. M. A., Hu, Y., Campoy-Quiles, M., Alonso, M. I., Weber, O. J., Azarhoosh, P., van Schilfgaarde, M., Weller, M. T., Bein, T., Nelson, J., Docampo, P. & Barnes, P. R. F. Reversible Hydration of CH3NH3PbI3 in Films, Single Crystals, and Solar Cells. *Chem. Mater.* **27,** 3397–3407 (2015).

44. Jena, A. K., Kulkarni, A. & Miyasaka, T. Halide Perovskite Photovoltaics: Background, Status, and Future Prospects. *Chem. Rev.* **119,** 3036–3103 (2019).

45. Zhou, H., Chen, Q., Li, G., Luo, S., Song, T., Duan, H.-S., Hong, Z., You, J., Liu, Y. & Yang, Y. Interface engineering of highly efficient perovskite solar cells. *Science* **345,** 542–546 (2014).

46. Hawash, Z., Ono, L. K., Raga, S. R., Lee, M. V. & Qi, Y. Air-Exposure Induced Dopant Redistribution and Energy Level Shifts in Spin-Coated Spiro-MeOTAD Films. *Chem. Mater.* **27,** 562–569 (2015).

47. Jung, M.-C., Raga, S. R., Ono, L. K. & Qi, Y. Substantial improvement of perovskite solar cells stability by pinhole-free hole transport layer with doping engineering. *Sci. Rep.* **5,** 9863 (2015).

48. Hadjipaschalis, I., Poullikkas, A. & Efthimiou, V. Overview of current and future energy storage technologies for electric power applications. *Renew. Sustain. Energy Rev.* **13,** 1513–1522 (2009).

49. Khaligh, A. & Li, Z. Battery, Ultracapacitor, Fuel Cell, and Hybrid Energy Storage Systems for Electric, Hybrid Electric, Fuel Cell, and Plug-In Hybrid Electric Vehicles: State of the Art. *IEEE Trans. Veh. Technol.* **59,** 2806–2814 (2010).

50. Chalk, S. G. & Miller, J. F. Key challenges and recent progress in batteries, fuel cells, and hydrogen storage for clean energy systems. *J. Power Sources* **159,** 73–80 (2006).

51. Roy, P. & Srivastava, S. K. Nanostructured anode materials for lithium ion batteries. *J. Mater. Chem. A* **3,** 2454–2484 (2015).

52. Mizushima, K., Jones, P. C., Wiseman, P. J. & Goodenough, J. B. LixCoO 2 (0<x<1): A NEW CATHODE MATERIAL FOR BATTERIES OF HIGH ENERGY DENSITY. *Mater. Res. Bull.* **15,** 783–789 (1980).

53. Schipper, F., Erickson, E. M., Erk, C., Shin, J.-Y., Chesneau, F. F. & Aurbach, D. Review—Recent Advances and Remaining Challenges for Lithium Ion Battery Cathodes I. Nickel-Rich, LiNixCoyMnzO2. *J. Electrochem. Soc.* **164,** A6220–A6228 (2017).

54. Broussely, M., Perton, F., Biensan, P., Bodet, J. M., Labat, J., Lecerf, A., Delmas, C., Rougier, A. & Pérès, J. P. LixNiO2, a promising cathode for rechargeable lithium batteries. *J. Power Sources* **54,** 109–114 (1995).

55. Blomgren, G. E. The Development and Future of Lithium Ion Batteries. *J. Electrochem. Soc.* **164,** A5019–A5025 (2017).

56. Types of Lithium-ion Batteries – Battery University. at <https://batteryuniversity.com/learn/article/types_of_lithium_ion>

57. Yoon, W.-S., Chung, K. Y., McBreen, J., Fischer, D. A. & Yang, X.-Q. Electronic structural changes of the electrochemically Li-ion deintercalated

LiNi0.8Co0.15Al0.05O2 cathode material investigated by X-ray absorption spectroscopy. *J. Power Sources* **174,** 1015–1020 (2007).

58. Sallis, S., Pereira, N., Mukherjee, P., Quackenbush, N. F., Faenza, N., Schlueter, C., Lee, T.-L., Yang, W. L., Cosandey, F., Amatucci, G. G. & Piper, L. F. J. Surface degradation of Li1–xNi0.80Co0.15Al0.05O2 cathodes: Correlating charge transfer impedance with surface phase transformations. *Appl. Phys. Lett.* **108,** 263902 (2016).

59. Hwang, S., Chang, W., Kim, S. M., Su, D., Kim, D. H., Lee, J. Y., Chung, K. Y. & Stach, E. A. Investigation of Changes in the Surface Structure of LixNi0.8Co0.15Al0.05O2 Cathode Materials Induced by the Initial Charge. *Chem. Mater.* **26,** 1084–1092 (2014).

60. Takanashi, S. & Abe, Y. Improvement of the electrochemical performance of an NCA positive-electrode material of lithium ion battery by forming an Al-rich surface layer. *Ceram. Int.* **43,** 9246–9252 (2017).

61. Hou, P., Zhang, H., Deng, X., Xu, X. & Zhang, L. Stabilizing the Electrode/Electrolyte Interface of LiNi0.8Co0.15Al0.05O2 through Tailoring Aluminum Distribution in Microspheres as Long-Life, High-Rate, and Safe Cathode for Lithium-Ion Batteries. *ACS Appl. Mater. Interfaces* **9,** 29643–29653 (2017).

62. Kasavajjula, U., Wang, C. & Appleby, A. J. Nano- and bulk-silicon-based insertion anodes for lithium-ion secondary cells. *J. Power Sources* **163,** 1003–1039 (2007).

63. Zuo, X., Zhu, J., Müller-Buschbaum, P. & Cheng, Y.-J. Silicon based lithium-ion battery anodes: A chronicle perspective review. *Nano Energy* **31,** 113–143 (2017).

64. Wu, M., Xiao, X., Vukmirovic, N., Xun, S., Das, P. K., Song, X., Olalde-Velasco, P., Wang, D., Weber, A. Z., Wang, L.-W., Battaglia, V. S., Yang, W. & Liu, G. Toward an Ideal Polymer Binder Design for High-Capacity Battery Anodes. *J. Am. Chem. Soc.* **135,** 12048–12056 (2013).

65. Wang, C., Wu, H., Chen, Z., McDowell, M. T., Cui, Y. & Bao, Z. Self-healing chemistry enables the stable operation of silicon microparticle anodes for high-energy lithium-ion batteries. *Nat. Chem.* **5,** 1042–1048 (2013).

66. Choi, S., Kwon, T., Coskun, A. & Choi, J. W. Highly elastic binders integrating polyrotaxanes for silicon microparticle anodes in lithium ion batteries. *Science* **357,** 279–283 (2017).

67. Karkar, Z., Guyomard, D., Roué, L. & Lestriez, B. A comparative study of polyacrylic acid (PAA) and carboxymethyl cellulose (CMC) binders for Si-based electrodes. *Electrochimica Acta* **258,** 453–466 (2017).

68. Magasinski, A., Zdyrko, B., Kovalenko, I., Hertzberg, B., Burtovyy, R., Huebner, C. F., Fuller, T. F., Luzinov, I. & Yushin, G. Toward Efficient Binders for Li-Ion Battery Si-Based Anodes: Polyacrylic Acid. *ACS Appl. Mater. Interfaces* **2,** 3004–3010 (2010).

69. Song, J., Chen, S., Zhou, M., Xu, T., Lv, D., L. Gordin, M., Long, T., Melnyk, M. & Wang, D. Micro-sized silicon–carbon composites composed of carbon-coated sub-10 nm Si primary particles as high-performance anode materials for lithium-ion batteries. *J. Mater. Chem. A* **2,** 1257–1262 (2014).

70. Yi, R., Dai, F., Gordin, M. L., Chen, S. & Wang, D. Micro-sized Si-C Composite with Interconnected Nanoscale Building Blocks as High-Performance Anodes for Practical Application in Lithium-Ion Batteries. *Adv. Energy Mater.* **3,** 295–300 (2013).

71. Huang, X., Sui, X., Yang, H., Ren, R., Wu, Y., Guo, X. & Chen, J. HF-free synthesis of Si/C yolk/shell anodes for lithium-ion batteries. *J. Mater. Chem. A* **6,** 2593–2599 (2018).

72. Liu, N., Lu, Z., Zhao, J., McDowell, M. T., Lee, H.-W., Zhao, W. & Cui, Y. A pomegranate-inspired nanoscale design for large-volume-change lithium battery anodes. *Nat. Nanotechnol.* **9,** 187–192 (2014).

73. Piper, D. M., Yersak, T. A., Son, S.-B., Kim, S. C., Kang, C. S., Oh, K. H., Ban, C., Dillon, A. C. & Lee, S.-H. Conformal Coatings of Cyclized-PAN for Mechanically Resilient Si nano-Composite Anodes. *Adv. Energy Mater.* **3,** 697–702 (2013).

74. Ge, M., Fang, X., Rong, J. & Zhou, C. Review of porous silicon preparation and its application for lithium-ion battery anodes. *Nanotechnology* **24,** 422001 (2013).

75. Wu, Q., Shi, B., Bareño, J., Liu, Y., Maroni, V. A., Zhai, D., Dees, D. W. & Lu, W. Investigations of Si Thin Films as Anode of Lithium-Ion Batteries. *ACS Appl. Mater. Interfaces* **10,** 3487–3494 (2018).

76. Wu, H. & Cui, Y. Designing nanostructured Si anodes for high energy lithium ion batteries. *Nano Today* **7,** 414–429 (2012).

77. Gu, M., Li, Y., Li, X., Hu, S., Zhang, X., Xu, W., Thevuthasan, S., Baer, D. R., Zhang, J.-G., Liu, J. & Wang, C. In Situ TEM Study of Lithiation Behavior of

Silicon Nanoparticles Attached to and Embedded in a Carbon Matrix. *ACS Nano* **6,** 8439–8447 (2012).

78. McDowell, M. T., Lee, S. W., Harris, J. T., Korgel, B. A., Wang, C., Nix, W. D. & Cui, Y. In Situ TEM of Two-Phase Lithiation of Amorphous Silicon Nanospheres. *Nano Lett.* **13,** 758–764 (2013).

79. Shen, C., Ge, M., Luo, L., Fang, X., Liu, Y., Zhang, A., Rong, J., Wang, C. & Zhou, C. *In Situ* and *Ex Situ* TEM Study of Lithiation Behaviours of Porous Silicon Nanostructures. *Sci. Rep.* **6,** 31334 (2016).

80. Liu, X. H., Zheng, H., Zhong, L., Huang, S., Karki, K., Zhang, L. Q., Liu, Y., Kushima, A., Liang, W. T., Wang, J. W., Cho, J.-H., Epstein, E., Dayeh, S. A., Picraux, S. T., Zhu, T., Li, J., Sullivan, J. P., Cumings, J., Wang, C., Mao, S. X., Ye, Z. Z., Zhang, S. & Huang, J. Y. Anisotropic Swelling and Fracture of Silicon Nanowires during Lithiation. *Nano Lett.* **11,** 3312–3318 (2011).

81. McDowell, M. T., Lee, S. W., Nix, W. D. & Cui, Y. 25th Anniversary Article: Understanding the Lithiation of Silicon and Other Alloying Anodes for Lithium-Ion Batteries. *Adv. Mater.* **25,** 4966–4985 (2013).

82. Moore, G. E. Cramming More Components Onto Integrated Circuits. *Proc. IEEE* **86,** 82–85 (1998).

83. Hisamoto, D., Kedzierski, and J., Takeuchi, H., Asano, K., Kuo, C., Anderson, E. & and, and J. B. FinFET-a self-aligned double-gate MOSFET scalable to 20 nm. *IEEE Trans. Electron Devices* **47,** 2320–2325 (2000).

84. Inoue, K., Yano, F., Nishida, A., Takamizawa, H., Tsunomura, T., Nagai, Y. & Hasegawa, M. Dopant distributions in n-MOSFET structure observed by atom probe tomography. *Ultramicroscopy* **109,** 1479–1484 (2009).

85. Takamizawa, H., Shimizu, Y., Nozawa, Y., Toyama, T., Morita, H., Yabuuchi, Y., Ogura, M. & Nagai, Y. Dopant characterization in self-regulatory plasma doped fin field-effect transistors by atom probe tomography. *Appl. Phys. Lett.* **100,** 093502 (2012).

86. Larson, D. J., Alvis, R. L., Lawrence, D. F., Prosa, T. J., Ulfig, R. M., Reinhard, D. A., Clifton, P. H., Gerstl, S. S. A., Bunton, J. H., Lenz, D. R., Kelly, T. F. & Stiller, K. Analysis of Bulk Dielectrics with Atom Probe Tomography. *Microsc. Microanal.* **14,** 1254–1255 (2008).

87. Parikh, P., Senowitz, C., Lyons, D., Martin, I., Prosa, T. J., DiBattista, M., Devaraj, A. & Meng, Y. S. Three-Dimensional Nanoscale Mapping of State-of-

the-Art Field-Effect Transistors (FinFETs). *Microsc. Microanal.* **23,** 916–925 (2017).

88. Gault, B., Moody, M. P., Cairney, J. M. & Ringer, S. P. *Atom Probe Microscopy*. (Springer Science & Business Media, 2012).

89. Gribb, A. A. & Kelly, T. F. Atom Probe Analysis. *Adv. Mater. Process.* **162,** 31–34 (2004).

90. Kelly, T. F., Larson, D. J., Thompson, K., Alvis, R. L., Bunton, J. H., Olson, J. D. & Gorman, B. P. Atom Probe Tomography of Electronic Materials. *Annu. Rev. Mater. Res.* **37,** 681–727 (2007).

91. IMR Group - Kelly Nygren. at <http://robertson.matse.illinois.edu/Kelly.html>

92. Larson, D. J., Prosa, T. J., Ulfig, R. M., Geiser, B. P. & Kelly, T. F. *Local Electrode Atom Probe Tomography*. (Springer New York, 2013). doi:10.1007/978-1-4614-8721-0

93. Miller, M. K. *Atom-probe tomography: the local electrode atom probe*. (Springer, 2014).

94. Felfer, P., McCarroll, I., Macauley, C. & Cairney, J. M. A simple approach to atom probe sample preparation by using shadow masks. *Ultramicroscopy* **160,** 163–167 (2016).

95. Takahashi, J., Kawakami, K., Kobayashi, Y. & Tarui, T. The first direct observation of hydrogen trapping sites in TiC precipitation-hardening steel through atom probe tomography. *Scr. Mater.* **63,** 261–264 (2010).

96. Valley, J. W., Cavosie, A. J., Ushikubo, T., Reinhard, D. A., Lawrence, D. F., Larson, D. J., Clifton, P. H., Kelly, T. F., Wilde, S. A., Moser, D. E. & Spicuzza, M. J. Hadean age for a post-magma-ocean zircon confirmed by atom-probe tomography. *Nat. Geosci.* **7,** 219–223 (2014).

97. Kambham, A. K., Zschaetzsch, G., Sasaki, Y., Togo, M., Horiguchi, N., Mody, J., Florakis, A., Gajula, D. R., Kumar, A., Gilbert, M. & Vandervorst, W. Atom Probe Tomography for 3D-dopant analysis in FinFET devices. in *2012 Symp. VLSI Technol. VLSIT* 77–78 (2012). doi:10.1109/VLSIT.2012.6242469

98. Gordon, L. M., Tran, L. & Joester, D. Atom Probe Tomography of Apatites and Bone-Type Mineralized Tissues. *ACS Nano* **6,** 10667–10675 (2012).

99. Gordon, L. M. & Joester, D. Nanoscale chemical tomography of buried organic–inorganic interfaces in the chiton tooth. *Nature* **469,** 194–197 (2011).

100. Stoffers, A., Cojocaru-Mirédin, O., Seifert, W., Zaefferer, S., Riepe, S. & Raabe, D. Grain boundary segregation in multicrystalline silicon: correlative characterization by EBSD, EBIC, and atom probe tomography. *Prog. Photovolt. Res. Appl.* **23,** 1742–1753 (2015).

101. Gorman, B. P., Norman, A. G. & Yan, Y. Atom Probe Analysis of III–V and Si-Based Semiconductor Photovoltaic Structures. *Microsc. Microanal.* **13,** 493–502 (2007).

102. Hernández-Saz, J., Herrera, M., Delgado, F. J., Duguay, S., Philippe, T., Gonzalez, M., Abell, J., Walters, R. J. & Molina, S. I. Atom-scale compositional distribution in InAlAsSb-based triple junction solar cells by atom probe tomography. *Nanotechnology* **27,** 305402 (2016).

103. Choi, P.-P., Cojocaru-Mirédin, O., Abou-Ras, D., Caballero, R., Raabe, D., Smentkowski, V. S., Park, C. G., Gu, G. H., Mazumder, B., Wong, M. H., Hu, Y.-L., Melo, T. P. & Speck, J. S. Atom Probe Tomography of Compound Semiconductors for Photovoltaic and Light-Emitting Device Applications. *Microsc. Today* **20,** 18–24 (2012).

104. Cojocaru-Mirédin, O., Choi, P., Wuerz, R. & Raabe, D. Atomic-scale distribution of impurities in CuInSe2-based thin-film solar cells. *Ultramicroscopy* **111,** 552–556 (2011).

105. Cojocaru-Mirédin, O., Choi, P., Abou-Ras, D., Schmidt, S. S., Caballero, R. & Raabe, D. Characterization of Grain Boundaries in Cu(In,Ga)Se\bf 2Films Using Atom-Probe Tomography. *IEEE J. Photovolt.* **1,** 207–212 (2011).

106. Keller, J., Schlesiger, R., Riedel, I., Parisi, J., Schmitz, G., Avellan, A. & Dalibor, T. Grain boundary investigations on sulfurized Cu(In,Ga)(S,Se)2 solar cells using atom probe tomography. *Sol. Energy Mater. Sol. Cells* **117,** 592–598 (2013).

107. Diercks, D. R., Musselman, M., Morgenstern, A., Wilson, T., Kumar, M., Smith, K., Kawase, M., Gorman, B. P., Eberhart, M. & Packard, C. E. Evidence for Anisotropic Mechanical Behavior and Nanoscale Chemical Heterogeneity in Cycled LiCoO2. *J. Electrochem. Soc.* **161,** F3039–F3045 (2014).

108. Maier, J., Pfeiffer, B., Volkert, C. A. & Nowak, C. Three-Dimensional Microstructural Characterization of Lithium Manganese Oxide with Atom Probe Tomography. *Energy Technol.* **4,** 1565–1574 (2016).

109. Vissers, D. R., Isheim, D., Zhan, C., Chen, Z., Lu, J. & Amine, K. Understanding atomic scale phenomena within the surface layer of a long-term cycled 5V spinel electrode. *Nano Energy* **19,** 297–306 (2016).

110. Devaraj, A., Gu, M., Colby, R., Yan, P., Wang, C. M., Zheng, J. M., Xiao, J., Genc, A., Zhang, J. G., Belharouak, I., Wang, D., Amine, K. & Thevuthasan, S. Visualizing nanoscale 3D compositional fluctuation of lithium in advanced lithium-ion battery cathodes. *Nat. Commun.* **6,** 8014 (2015).

111. Mohanty, D., Mazumder, B., Devaraj, A., Sefat, A. S., Huq, A., David, L. A., Payzant, E. A., Li, J., Wood, D. L. & Daniel, C. Resolving the degradation pathways in high-voltage oxides for high-energy-density lithium-ion batteries; Alternation in chemistry, composition and crystal structures. *Nano Energy* **36,** 76–84 (2017).

112. Santhanagopalan, D., Schreiber, D. K., Perea, D. E., Martens, R. L., Janssen, Y., Khalifah, P. & Meng, Y. S. Effects of laser energy and wavelength on the analysis of LiFePO4 using laser assisted atom probe tomography. *Ultramicroscopy* **148,** 57–66 (2015).

113. Sepehri-Amin, H., Ohkubo, T., Kodzuka, M., Yamamura, H., Saito, T., Iba, H. & Hono, K. Evidence for nano-Si clusters in amorphous SiO anode materials for rechargeable Li-ion batteries. *Scr. Mater.* **69,** 92–95 (2013).

114. Devaraj, A., Colby, R., Hess, W. P., Perea, D. E. & Thevuthasan, S. Role of Photoexcitation and Field Ionization in the Measurement of Accurate Oxide Stoichiometry by Laser-Assisted Atom Probe Tomography. *J. Phys. Chem. Lett.* **4,** 993–998 (2013).

115. Mano, M. M. *Digital Logic and Computer Design*. (Prentice Hall PTR, 1979).

116. Bardeen, J. & Brattain, W. H. The Transistor, A Semi-Conductor Triode. *Phys. Rev.* **74,** 230–231 (1948).

117. Deal, B. E. & Early, J. M. *75th AnniVersary Review Series The Evolution of Silicon Semiconductor Technology: 19S2-1977*.

118. Evolution of the MOS transistor-from conception to VLSI. *Proc. IEEE* **76,** 1280–1326 (1988).

119. Weste, N. H. E. & Eshraghian, K. Principles of CMOS VLSI design: A systems perspective. *NASA STIRecon Tech. Rep. A* **85,** (1985).

120. Bohr, M. The evolution of scaling from the homogeneous era to the heterogeneous era. in *2011 Int. Electron Devices Meet.* 1.1.1-1.1.6 (2011). doi:10.1109/IEDM.2011.6131469

121. Thompson, S. E. & Parthasarathy, S. Moore's law: the future of Si microelectronics. *Mater. Today* **9,** 20–25 (2006).

122. Bruce, M. R., Bruce, V. J., Eppes, D. H., Wilcox, J., Cole, E. I., Tangyunyong, P., Hawkins, C. F. & Ring, R. Soft defect localization (SDL) in integrated circuits using laser scanning microscopy. in *16th Annu. Meet. IEEE Lasers Electro-Opt. Soc. 2003 LEOS 2003* **2,** 662–663 vol.2 (2003).

123. Phang, J. C. H., Chan, D. S. H., Palaniappan, M., Chin, J. M., Davis, B., Bruce, M., Wilcox, J., Gilfeather, G., Chua, C. M., Koh, L. S., Ng, H. Y. & Tan, S. H. A review of laser induced techniques for microelectronic failure analysis. in *Proc. 11th Int. Symp. Phys. Fail. Anal. Integr. Circuits IPFA 2004 IEEE Cat No04TH8743* 255–261 (2004). doi:10.1109/IPFA.2004.1345617

124. Nikawa, K., Inoue, S., Morimoto, K. & Sone, S. Failure analysis case studies using the IR-OBIRCH (infrared optical beam induced resistance change) method. in *Proc. Eighth Asian Test Symp. ATS99* 394–399 (1999). doi:10.1109/ATS.1999.810781

125. Zhang, L., Ohuchi, K., Adachi, K., Ishimaru, K., Takayanagi, M. & Nishiyama, A. High-resolution characterization of ultrashallow junctions by measuring in vacuum with scanning spreading resistance microscopy. *Appl. Phys. Lett.* **90,** 192103 (2007).

126. Hayase, Y., Hara, K., Ogata, S., Zhang, L., Akutsu, H., Kurihara, M., Norimatsu, K. & Nagamine, S. Applications of site-specific scanning spreading resistance microscopy (SSRM) to failure analysis of production lines. in *2012 12th Int. Workshop Junction Technol.* 146–149 (2012). doi:10.1109/IWJT.2012.6212830

127. Pei, G., Kedzierski, J., Oldiges, P., Ieong, M. & Kan, E. C.-. FinFET design considerations based on 3-D simulation and analytical modeling. *IEEE Trans. Electron Devices* **49,** 1411–1419 (2002).

128. Baravelli, E., Jurczak, M., Speciale, N., Meyer, K. D. & Dixit, A. Impact of LER and Random Dopant Fluctuations on FinFET Matching Performance. *IEEE Trans. Nanotechnol.* **7,** 291–298 (2008).

129. Bernstein, K., Frank, D. J., Gattiker, A. E., Haensch, W., Ji, B. L., Nassif, S. R., Nowak, E. J., Pearson, D. J. & Rohrer, N. J. High-performance CMOS

variability in the 65-nm regime and beyond. *IBM J. Res. Dev.* **50,** 433–449 (2006).

130. Wang, X., Brown, A. R. & Asenov, and A. Statistical variability and reliability in nanoscale FinFETs. in *2011 Int. Electron Devices Meet.* 5.4.1-5.4.4 (2011). doi:10.1109/IEDM.2011.6131494

131. Batson, P. E., Dellby, N. & Krivanek, O. L. Sub-ångstrom resolution using aberration corrected electron optics. *Nature* **418,** 617 (2002).

132. Lefebvre, W., Vurpillot, F. & Sauvage, X. *Atom Probe Tomography: Put Theory Into Practice*. (Academic Press, 2016).

133. Miller, M. K. *Atom Probe Tomography: Analysis at the Atomic Level*. (Springer Science & Business Media, 2012).

134. Thompson, K., Flaitz, P. L., Ronsheim, P., Larson, D. J. & Kelly, T. F. Imaging of Arsenic Cottrell Atmospheres Around Silicon Defects by Three-Dimensional Atom Probe Tomography. *Science* **317,** 1370–1374 (2007).

135. Ulfig, R., Thompson, K., Alvis, R., Larson, D. J. & Ronsheim, P. Three Dimensional Compositional Characterization of Dielectric Films with LEAP Tomography. *Microsc. Microanal.* **13,** 828–829 (2007).

136. Han, B., Takamizawa, H., Shimizu, Y., Inoue, K., Nagai, Y., Yano, F., Kunimune, Y., Inoue, M. & Nishida, A. Phosphorus and boron diffusion paths in polycrystalline silicon gate of a trench-type three-dimensional metal-oxide-semiconductor field effect transistor investigated by atom probe tomography. *Appl. Phys. Lett.* **107,** 023506 (2015).

137. Larson, D. J., Lawrence, D., Lefebvre, W., Olson, D., Prosa, T. J., Reinhard, D. A., Ulfig, R. M., Clifton, P. H., Bunton, J. H., Lenz, D., Olson, J. D., Renaud, L., Martin, I. & Kelly, T. F. Toward atom probe tomography of microelectronic devices. *J. Phys. Conf. Ser.* **326,** 012030 (2011).

138. Kambham, A. K., Kumar, A., Florakis, A. & Vandervorst, W. Three-dimensional doping and diffusion in nano scaled devices as studied by atom probe tomography. *Nanotechnology* **24,** 275705 (2013).

139. Kambham, A. K., Kumar, A., Gilbert, M. & Vandervorst, W. 3D site specific sample preparation and analysis of 3D devices (FinFETs) by atom probe tomography. *Ultramicroscopy* **132,** 65–69 (2013).

140. Kambham, A. K., Mody, J., Gilbert, M., Koelling, S. & Vandervorst, W. Atom-probe for FinFET dopant characterization. *Ultramicroscopy* **111,** 535–539 (2011).

141. Panciera, F., Hoummada, K., Gregoire, M., Juhel, M., Lorut, F., Bicais, N. & Mangelinck, D. Atom probe tomography of SRAM transistors: Specimen preparation methods and analysis. *Microelectron. Eng.* **107,** 167–172 (2013).

142. Hatzistergos, M. S., Hopstaken, M., Kim, E., Vanamurthy, L. & Shaffer, J. F. Characterization of 3D Dopant Distribution in State of the Art FinFET Structures. *Microsc. Microanal.* **19,** 960–961 (2013).

143. Larson, D. J., Foord, D. T., Petford-Long, A. K., Liew, H., Blamire, M. G., Cerezo, A. & Smith, G. D. W. Field-ion specimen preparation using focused ion-beam milling. *Ultramicroscopy* **79,** 287–293 (1999).

144. Thompson, K., Lawrence, D., Larson, D. J., Olson, J. D., Kelly, T. F. & Gorman, B. In situ site-specific specimen preparation for atom probe tomography. *Ultramicroscopy* **107,** 131–139 (2007).

145. Lawrence, D., Alvis, R. & Olson, D. Specimen Preparation for Cross-Section Atom Probe Analysis. *Microsc. Microanal.* **14,** 1004–1005 (2008).

146. Koelling, S., Innocenti, N., Hellings, G., Gilbert, M., Kambham, A. K., De Meyer, K. & Vandervorst, W. Characteristics of cross-sectional atom probe analysis on semiconductor structures. *Ultramicroscopy* **111,** 540–545 (2011).

147. Lin, Y.-S., Puthenkovilakam, R. & Chang, J. P. Dielectric property and thermal stability of HfO2 on silicon. *Appl. Phys. Lett.* **81,** 2041–2043 (2002).

148. Gilbert, M., Vandervorst, W., Koelling, S. & Kambham, A. K. Atom probe analysis of a 3D finFET with high-k metal gate. *Ultramicroscopy* **111,** 530–534 (2011).

149. Devaraj, A., Colby, R., Vurpillot, F. & Thevuthasan, S. Understanding Atom Probe Tomography of Oxide-Supported Metal Nanoparticles by Correlation with Atomic-Resolution Electron Microscopy and Field Evaporation Simulation. *J. Phys. Chem. Lett.* **5,** 1361–1367 (2014).

150. Grenier, A., Duguay, S., Barnes, J. P., Serra, R., Haberfehlner, G., Cooper, D., Bertin, F., Barraud, S., Audoit, G., Arnoldi, L., Cadel, E., Chabli, A. & Vurpillot, F. 3D analysis of advanced nano-devices using electron and atom probe tomography. *Ultramicroscopy* **136,** 185–192 (2014).

151. Madaan, N., Bao, J., Nandasiri, M., Xu, Z., Thevuthasan, S. & Devaraj, A. Impact of dynamic specimen shape evolution on the atom probe tomography results of doped epitaxial oxide multilayers: Comparison of experiment and simulation. *Appl. Phys. Lett.* **107,** 091601 (2015).

152. Vurpillot, F., Gruber, M., Da Costa, G., Martin, I., Renaud, L. & Bostel, A. Pragmatic reconstruction methods in atom probe tomography. *Ultramicroscopy* **111,** 1286–1294 (2011).

153. Bokor, and J. Sensitivity of double-gate and FinFETDevices to process variations. *IEEE Trans. Electron Devices* **50,** 2255–2261 (2003).

154. The Battery Will Kill Fossil Fuels—It's Only a Matter of Time. (2018). at <https://www.bloomberg.com/news/articles/2018-03-08/the-battery-will-kill-fossil-fuels-it-s-only-a-matter-of-time>

155. Liu, H., Wolf, M., Karki, K., Yu, Y.-S., Stach, E. A., Cabana, J., Chapman, K. W. & Chupas, P. J. Intergranular Cracking as a Major Cause of Long-Term Capacity Fading of Layered Cathodes. *Nano Lett.* **17,** 3452–3457 (2017).

156. Sallis, S., Pereira, N., Mukherjee, P., Quackenbush, N. F., Faenza, N., Schlueter, C., Lee, T.-L., Yang, W. L., Cosandey, F., Amatucci, G. G. & Piper, L. F. J. Surface degradation of Li1–xNi0.80Co0.15Al0.05O2 cathodes: Correlating charge transfer impedance with surface phase transformations. *Appl. Phys. Lett.* **108,** 263902 (2016).

157. Zhang, H., Karki, K., Huang, Y., Whittingham, M. S., Stach, E. A. & Zhou, G. Atomic Insight into the Layered/Spinel Phase Transformation in Charged $LiNi_{0.80}Co_{0.15}Al_{0.05}O_2$ Cathode Particles. *J. Phys. Chem. C* **121,** 1421–1430 (2017).

158. Mohanty, D., Dahlberg, K., King, D. M., David, L. A., Sefat, A. S., Wood, D. L., Daniel, C., Dhar, S., Mahajan, V., Lee, M. & Albano, F. Modification of Ni-Rich FCG NMC and NCA Cathodes by Atomic Layer Deposition: Preventing Surface Phase Transitions for High-Voltage Lithium-Ion Batteries. *Sci. Rep.* **6,** 26532 (2016).

159. Kim, U.-H., Kim, J.-H., Hwang, J.-Y., Ryu, H.-H., Yoon, C. S. & Sun, Y.-K. Compositionally and structurally redesigned high-energy Ni-rich layered cathode for next-generation lithium batteries. *Mater. Today* **23,** 26–36 (2019).

160. Qiu, Q.-Q., Shadike, Z., Wang, Q.-C., Yue, X.-Y., Li, X.-L., Yuan, S.-S., Fang, F., Wu, X.-J., Hunt, A., Waluyo, I., Bak, S.-M., Yang, X.-Q. & Zhou, Y.-N. Improving the Electrochemical Performance and Structural Stability of the

LiNi0.8Co0.15Al0.05O2 Cathode Material at High-Voltage Charging through Ti Substitution. *ACS Appl. Mater. Interfaces* (2019). doi:10.1021/acsami.9b05100

161. Schmitz, G., Abouzari, R., Berkemeier, F., Gallasch, T., Greiwe, G., Stockhoff, T. & Wunde, F. Nanoanalysis and Ion Conductivity of Thin Film Battery Materials. *Z. Für Phys. Chem.* **224,** 1795–1829 (2010).

162. Pfeiffer, B., Maier, J., Arlt, J. & Nowak, C. In Situ Atom Probe Deintercalation of Lithium-Manganese-Oxide. *Microsc. Microanal.* **23,** 314–320 (2017).

163. Huang, X., Pu, H., Chang, J., Cui, S., Hallac, P. B., Jiang, J., Hurley, P. T. & Chen, J. Improved Cyclic Performance of Si Anodes for Lithium-Ion Batteries by Forming Intermetallic Interphases between Si Nanoparticles and Metal Microparticles. *ACS Appl. Mater. Interfaces* **5,** 11965–11970 (2013).

164. Liu, X. H., Fan, F., Yang, H., Zhang, S., Huang, J. Y. & Zhu, T. Self-Limiting Lithiation in Silicon Nanowires. *ACS Nano* **7,** 1495–1503 (2013).

165. Seidlhofer, B.-K., Jerliu, B., Trapp, M., Hüger, E., Risse, S., Cubitt, R., Schmidt, H., Steitz, R. & Ballauff, M. Lithiation of Crystalline Silicon As Analyzed by Operando Neutron Reflectivity. *ACS Nano* **10,** 7458–7466 (2016).

166. Radvanyi, E., Vito, E. D., Porcher, W., Danet, J., Desbois, P., Colin, J.-F. & Larbi, S. J. S. Study of lithiation mechanisms in silicon electrodes by Auger Electron Spectroscopy. *J. Mater. Chem. A* **1,** 4956–4965 (2013).

167. Liu, X. H., Wang, J. W., Huang, S., Fan, F., Huang, X., Liu, Y., Krylyuk, S., Yoo, J., Dayeh, S. A., Davydov, A. V., Mao, S. X., Picraux, S. T., Zhang, S., Li, J., Zhu, T. & Huang, J. Y. *In situ* atomic-scale imaging of electrochemical lithiation in silicon. *Nat. Nanotechnol.* **7,** 749–756 (2012).

168. Wang, X., Li, Y. & Meng, Y. S. Cryogenic Electron Microscopy for Characterizing and Diagnosing Batteries. *Joule* **2,** 2225–2234 (2018).

169. Koo, B., Kim, H., Cho, Y., Lee, K. T., Choi, N.-S. & Cho, J. A Highly Cross-Linked Polymeric Binder for High-Performance Silicon Negative Electrodes in Lithium Ion Batteries. *Angew. Chem. Int. Ed.* **51,** 8762–8767 (2012).

170. Liu, M., Johnston, M. B. & Snaith, H. J. Efficient planar heterojunction perovskite solar cells by vapour deposition. *Nature* **501,** 395–398 (2013).

171. Burschka, J., Pellet, N., Moon, S.-J., Humphry-Baker, R., Gao, P., Nazeeruddin, M. K. & Grätzel, M. Sequential deposition as a route to high-performance perovskite-sensitized solar cells. *Nature* **499,** 316–319 (2013).

172. Yang, W. S., Noh, J. H., Jeon, N. J., Kim, Y. C., Ryu, S., Seo, J. & Seok, S. I. High-performance photovoltaic perovskite layers fabricated through intramolecular exchange. *Science* **348,** 1234–1237 (2015).

173. Kaltenbrunner, M., Adam, G., Głowacki, E. D., Drack, M., Schwödiauer, R., Leonat, L., Apaydin, D. H., Groiss, H., Scharber, M. C., White, M. S., Sariciftci, N. S. & Bauer, S. Flexible high power-per-weight perovskite solar cells with chromium oxide–metal contacts for improved stability in air. *Nat. Mater.* **14,** 1032–1039 (2015).

174. Yin, X., Chen, P., Que, M., Xing, Y., Que, W., Niu, C. & Shao, J. Highly Efficient Flexible Perovskite Solar Cells Using Solution-Derived NiOx Hole Contacts. *ACS Nano* **10,** 3630–3636 (2016).

175. Li, R., Xiang, X., Tong, X., Zou, J. & Li, Q. Wearable Double-Twisted Fibrous Perovskite Solar Cell. *Adv. Mater.* **27,** 3831–3835 (2015).

176. Ball, J. M., Lee, M. M., Hey, A. & Snaith, H. J. Low-temperature processed meso-superstructured to thin-film perovskite solar cells. *Energy Environ. Sci.* **6,** 1739–1743 (2013).

177. Fu, F., Feurer, T., Jäger, T., Avancini, E., Bissig, B., Yoon, S., Buecheler, S. & Tiwari, A. N. Low-temperature-processed efficient semi-transparent planar perovskite solar cells for bifacial and tandem applications. *Nat. Commun.* **6,** 8932 (2015).

178. Edri, E., Kirmayer, S., Henning, A., Mukhopadhyay, S., Gartsman, K., Rosenwaks, Y., Hodes, G. & Cahen, D. Why Lead Methylammonium Tri-Iodide Perovskite-Based Solar Cells Require a Mesoporous Electron Transporting Scaffold (but Not Necessarily a Hole Conductor). *Nano Lett.* **14,** 1000–1004 (2014).

179. Nguyen, W. H., Bailie, C. D., Unger, E. L. & McGehee, M. D. Enhancing the Hole-Conductivity of Spiro-OMeTAD without Oxygen or Lithium Salts by Using Spiro(TFSI)2 in Perovskite and Dye-Sensitized Solar Cells. *J. Am. Chem. Soc.* **136,** 10996–11001 (2014).

180. Xiao, Z., Yuan, Y., Shao, Y., Wang, Q., Dong, Q., Bi, C., Sharma, P., Gruverman, A. & Huang, J. Giant switchable photovoltaic effect in organometal trihalide perovskite devices. *Nat. Mater.* **14,** 193–198 (2015).

181. Xu, X., Chen, Q., Hong, Z., Zhou, H., Liu, Z., Chang, W.-H., Sun, P., Chen, H., Marco, N. D., Wang, M. & Yang, Y. Working Mechanism for Flexible Perovskite Solar Cells with Simplified Architecture. *Nano Lett.* **15,** 6514–6520 (2015).

182. Kim, H.-S., Lee, J.-W., Yantara, N., Boix, P. P., Kulkarni, S. A., Mhaisalkar, S., Grätzel, M. & Park, N.-G. High Efficiency Solid-State Sensitized Solar Cell-Based on Submicrometer Rutile TiO2 Nanorod and CH3NH3PbI3 Perovskite Sensitizer. *Nano Lett.* **13,** 2412–2417 (2013).

183. Choi, H., Mai, C.-K., Kim, H.-B., Jeong, J., Song, S., Bazan, G. C., Kim, J. Y. & Heeger, A. J. Conjugated polyelectrolyte hole transport layer for inverted-type perovskite solar cells. *Nat. Commun.* **6,** 7348 (2015).

184. Liu, Y., Chen, Q., Duan, H.-S., Zhou, H., Yang, Y. (Michael), Chen, H., Luo, S., Song, T.-B., Dou, L., Hong, Z. & Yang, Y. A dopant-free organic hole transport material for efficient planar heterojunction perovskite solar cells. *J. Mater. Chem. A* **3,** 11940–11947 (2015).

185. You, J., Meng, L., Song, T.-B., Guo, T.-F., Yang, Y. (Michael), Chang, W.-H., Hong, Z., Chen, H., Zhou, H., Chen, Q., Liu, Y., De Marco, N. & Yang, Y. Improved air stability of perovskite solar cells via solution-processed metal oxide transport layers. *Nat. Nanotechnol.* **11,** 75–81 (2016).

186. Krüger, J., Plass, R., Cevey, L., Piccirelli, M., Grätzel, M. & Bach, U. High efficiency solid-state photovoltaic device due to inhibition of interface charge recombination. *Appl. Phys. Lett.* **79,** 2085–2087 (2001).

187. Yuan, W., Zhao, H., Hu, H., Wang, S. & Baker, G. L. Synthesis and Characterization of the Hole-Conducting Silica/Polymer Nanocomposites and Application in Solid-State Dye-Sensitized Solar Cell. *ACS Appl. Mater. Interfaces* **5,** 4155–4161 (2013).

188. Dualeh, A., Moehl, T., Tétreault, N., Teuscher, J., Gao, P., Nazeeruddin, M. K. & Grätzel, M. Impedance Spectroscopic Analysis of Lead Iodide Perovskite-Sensitized Solid-State Solar Cells. *ACS Nano* **8,** 362–373 (2014).

189. Boschloo, G., Häggman, L. & Hagfeldt, A. Quantification of the Effect of 4-tert-Butylpyridine Addition to I-/I3- Redox Electrolytes in Dye-Sensitized Nanostructured TiO2 Solar Cells. *J. Phys. Chem. B* **110,** 13144–13150 (2006).

190. Haque, S. A., Palomares, E., Cho, B. M., Green, A. N. M., Hirata, N., Klug, D. R. & Durrant, J. R. Charge Separation versus Recombination in Dye-Sensitized Nanocrystalline Solar Cells: the Minimization of Kinetic Redundancy. *J. Am. Chem. Soc.* **127,** 3456–3462 (2005).

191. Park, N.-G. Organometal Perovskite Light Absorbers Toward a 20% Efficiency Low-Cost Solid-State Mesoscopic Solar Cell. *J. Phys. Chem. Lett.* **4,** 2423–2429 (2013).

192. Li, W., Dong, H., Wang, L., Li, N., Guo, X., Li, J. & Qiu, Y. Montmorillonite as bifunctional buffer layer material for hybrid perovskite solar cells with protection from corrosion and retarding recombination. *J. Mater. Chem. A* **2,** 13587–13592 (2014).

193. Cappel, U. B., Daeneke, T. & Bach, U. Oxygen-Induced Doping of Spiro-MeOTAD in Solid-State Dye-Sensitized Solar Cells and Its Impact on Device Performance. *Nano Lett.* **12,** 4925–4931 (2012).

194. Abate, A., Leijtens, T., Pathak, S., Teuscher, J., Avolio, R., Errico, M. E., Kirkpatrik, J., Ball, J. M., Docampo, P., McPherson, I. & Snaith, H. J. Lithium salts as “redox active” p-type dopants for organic semiconductors and their impact in solid-state dye-sensitized solar cells. *Phys. Chem. Chem. Phys.* **15,** 2572–2579 (2013).

195. Wang, S., Yuan, W. & Meng, Y. S. Spectrum-Dependent Spiro-OMeTAD Oxidization Mechanism in Perovskite Solar Cells. *ACS Appl. Mater. Interfaces* **7,** 24791–24798 (2015).

196. Divitini, G., Cacovich, S., Matteocci, F., Cinà, L., Di Carlo, A. & Ducati, C. *In situ* observation of heat-induced degradation of perovskite solar cells. *Nat. Energy* **1,** 15012 (2016).

197. Bergmann, V. W., Weber, S. A. L., Javier Ramos, F., Nazeeruddin, M. K., Grätzel, M., Li, D., Domanski, A. L., Lieberwirth, I., Ahmad, S. & Berger, R. Real-space observation of unbalanced charge distribution inside a perovskite-sensitized solar cell. *Nat. Commun.* **5,** 5001 (2014).

198. Nanova, D., Kast, A. K., Pfannmöller, M., Müller, C., Veith, L., Wacker, I., Agari, M., Hermes, W., Erk, P., Kowalsky, W., Schröder, R. R. & Lovrinčić, R. Unraveling the Nanoscale Morphologies of Mesoporous Perovskite Solar Cells and Their Correlation to Device Performance. *Nano Lett.* **14,** 2735–2740 (2014).

199. Zhou, Y., Vasiliev, A. L., Wu, W., Yang, M., Pang, S., Zhu, K. & Padture, N. P. Crystal Morphologies of Organolead Trihalide in Mesoscopic/Planar Perovskite Solar Cells. *J. Phys. Chem. Lett.* **6,** 2292–2297 (2015).

200. Docampo, P., Hey, A., Guldin, S., Gunning, R., Steiner, U. & Snaith, H. J. Pore Filling of Spiro-OMeTAD in Solid-State Dye-Sensitized Solar Cells Determined Via Optical Reflectometry. *Adv. Funct. Mater.* **22,** 5010–5019 (2012).

201. Snaith, H. J., Humphry-Baker, R., Chen, P., Cesar, I., Zakeeruddin, S. M. & Grätzel, M. Charge collection and pore filling in solid-state dye-sensitized solar cells. *Nanotechnology* **19,** 424003 (2008).

202. Kim, S., Jeong Park, M., Balsara, N. P., Liu, G. & Minor, A. M. Minimization of focused ion beam damage in nanostructured polymer thin films. *Ultramicroscopy* **111,** 191–199 (2011).